The ISEELS Spectra of Some Cyclic Organic Molecules

THE INNER SHELL ELECTRON ENERGY LOSS SPECTRA OF SOME CYCLIC ORGANIC MOLECULES

By

DAVID C. NEWBURY, B.Sc.

A Thesis

Submitted to the School of Graduate Studies

in Partial Fulfilment of the Requirements

for the Degree

Master of Science

McMaster University

March, 1986

MASTER OF SCIENCE (1986)   McMASTER UNIVERSITY
Hamilton, Ontario

TITLE: Inner Shell Electron Energy Loss Spectroscopy of Some Cyclic Organic Molecules

AUTHOR: David C. Newbury, B.Sc. (University of Waterloo)

SUPERVISOR: Dr. Adam P. Hitchcock, Ph.D. (UBC)

NUMBER OF PAGES: xii, 164

ABSTRACT

Inner shell electron energy loss spectroscopy has been used to obtain the core excitation spectra of some cyclic molecules. Recorded under the conditions of small momentum transfer (typically 2.5 keV impact energy and small angle scattering, <5°), the spectra are equivalent to those produced by soft x-ray photoabsorption. The molecules investigated are aromatic (benzene, pyridine, furan and pyrrole), unsaturated (cyclopentene, cyclohexene and cyclo-octatetraene) and saturated (cyclopentane, cyclohexane, tetrahydrofuran, pyrrolidine and piperdine) species. The heterocyclic species contain a single heteroatom which is either nitrogen (pyridine, pyrrole, pyrrolidine and piperdine) or oxygen (furan and tetrahydrofuran). In all cases the spectra are dominated by shape resonance features. The carbon K-shell and heteroatom K-shell spectra are quite similar indicating the transitions are to a similar set of unoccupied orbitals.

In certain cases, condensed phase x-ray 'photoabsorption' spectra (recorded by partial electron yield) were available for the purposes of comparision. Such comparisions are very useful in unambiguously identifing Rydberg, π^* and σ^* states. As a result the carbon K-shell excitation spectrum of benzene has been reassigned. A previously unidentified class of(1s $\rightarrow \pi^*(CH_2)$) transitions has been identified and characterized in the spectra of the saturated molecules.

All of the spectra studied show continuum resonances which could be assigned to σ^* shape resonances. The saturated cyclic systems show a second continuum resonance which is attributed to the overlap of in-ring atomic orbitals. This feature is strongest in the five membered ring systems with a heteroatom. The relationship between the shape resonance position and bond length is extended to these molecules. In the cases where there is extensive delocalization the simple relationship begins to breakdown.

ACKNOWLEDGEMENT

The author would like to express his deep appreciation to a number of individuals who were instrumental in allowing this thesis to be completed. Foremost of these is my supervisor, Dr. Adam P. Hitchcock who provided excellent guidance through the world of electron spectroscopy. All the condensed phase NEXAFS data is courtesy of Dr. J. Stöhr, Dr. F. Sette and Mr. A.L. Johnson. The author also appreciates their help in interpreting the NEXAFS data. The construction of the differentially pumped spectrometer was done with the help of the excellent machining skills of Mr. M. Roberts. Much appreciation goes to Miss C.L. Poland who aided the production of the thesis and allowed ideas to be presented to her first.

Finally to my parents, Mr. and Mrs. Ronald Newbury and the rest of my family, who have supported me throughout my academic career. They never gave up on me, even when I was ready to. This thesis is dedicated to them.

TABLE OF CONTENTS

Descriptive note....ii
Abstract....iii
Acknowledgements....v
Table of Contents....vi
List of Figures....ix
List of Tables....xi

CHAPTER 1: Introduction....1

1.1 General Introduction....1
1.2 Aspects of Inner Shell Electron Energy Loss Spectroscopy....3
1.2.1 Vitual Photon Model....5
1.2.2 Further Theory....7
1.3 Comparision of ISEELS and Photoabsorption....10
1.4 Interpretation of ISEELS Spectra....14
1.4.1 Bound Resonances....15
1.4.2 Continuum Resonances....18
1.5 Shape Resonances....19
1.6 Shape Resonances for Bond Length Determination....22

CHAPTER 2: Experimental....28

2.1 Introdution....28
2.2 The Electron Source....28
2.3 The Spectrometer....29
2.3.1 The Lens System....31
2.3.2 The Analyzer....32
2.3.3 The Double Deflection System....35
2.4 Sample Handling....36
2.5 Energy Calibration....38
2.6 Spectral Aquisition....38

CHAPTER 3: Integration of Gas Phase and Condensed Phase Core Excitation Studies....41

3.1 Introduction....41
3.2 Near Edge X-ray Absorption Fine Structure....43
3.2.1 Comparison of Spectra....45
3.2.2 Effects of Surface Molecule Interactions....49

CHAPTER 4: The K-Shell Excitation Spectra of Benzene and Pyridine...51

4.1 Introduction....51
4.2 Benzene....52
4.2.1 Benzene Electron Energy Loss Spectra....52
4.2.2 Continuum Resonances in Benzene....53
4.2.3 Comparison to Solid and Monolayer NEXAFS Spectra...56

4.3 Pyridine..63
4.3.1 Pyridine Carbon K-Shell ISEELS Spectra.............63
4.3.2 Comparison to Solid and Monolayer NEXAFS Spectra...68
4.3.3 Pyridine Nitrogen K-Shell ISEELS Spectra...........69
4.3.4 Comparison to Condensed Phase NEXAFS Spectra.......72
4.4 Broadening of π^* Features.................................74
4.5 Conclusions...76

CHAPTER 5: Carbon K-Shell Spectra of Some Non-Aromatic Cyclic Hydrocarbons..77

5.1 Introduction..77
5.2 Results and Discussion................................78
5.2.1 Saturated Cyclic Hydrocarbons......................78
5.2.2 Comparison to Condensed Phase NEXAFS Spectra.......82
5.2.3 Unsaturated Hydrocarbons...........................88
5.2.4 Comparison to Condensed Phase Spectra..............91
5.3 Continuum Resonances in Cyclic Hydrocarbons...........98
5.4 Conclusions...99

CHAPTER 6: Inner Shell Electron Energy Loss Spectroscopy of Some Heterocyclic Molecules...............................100

6.1 Introduction..100
6.2 Estimation of Ionization Potential....................100
6.3 Furan...102
6.3.1 Furan Carbon K-Shell ISEELS Spectrum...............102
6.3.2 Furan Oxygen K-Shell ISEELS Spectrum...............106
6.4 Pyrrole...107
6.4.1 Pyrrole Carbon K-Shell ISEELS Spectrum.............107
6.4.2 Pyrrole Nitrogen K-Shell ISEELS Spectrum...........110
6.5 Tetrahydrofuran.......................................112
6.5.1 Tetrahydrofuran Carbon K-Shell ISEELS Spectrum.....112
6.5.2 Tetrahydrofuran Oxygen K-Shell ISEELS Spectrum.....116
6.6 Pyrrolidine...117
6.6.1 Pyrrolidine Carbon K-Shell ISEELS Spectrum.........117
6.6.2 Pyrrolidine Nitrogen K-Shell ISEELS Spectrum.......120
6.7 Piperdine...121
6.7.1 Piperdine Carbon K-Shell ISEELS Spectrum...........121
6.7.2 Piperdine Nitrogen K-Shell ISEELS Spectrum.........123
6.8 Continuum Resonances in the Heterocyclics.............125
6.9 Conclusions...126

CHAPTER 7: Interpretation of Continuum Features....................128

7.1 Introduction..128
7.1.1 The Shape Resonances Picture.......................128
7.1.2 Delocalized Sigma States...........................129
7.1.3 Multielectron Excitation...........................130
7.2 Cyclic Hydrocarbons...................................131
7.2.1 Geometry of Molecules..............................133

    - 7.2.2 Explanation of Continuum Features in Cyclic Hydrocarbons.....134
  - 7.3 Heterocyclic Molecules.....137
    - 7.3.1 Geometry of Molecules.....137
    - 7.3.2 Explanation of Continuum Features in Furan and Pyrrole.....137
    - 7.3.3 Explanation of Continuum Features in Saturated Heterocyclics.....140
  - 7.4 Influence of the Ring Size.....142
  - 7.5 State of the Shape Resonance Relationship.....142
  - 7.6 Conclusions.....155

CHAPTER 8: Concluding Remarks.....157

REFERENCES.....160

LIST OF FIGURES

Figure 1.1 Vitual Photon Model....................................6

Figure 1.2 Potential Well in a Molecule..........................16

Figure 1.3 K-Shell Electron Energy Loss Spectra of N_2............20

Figure 1.4 Shape Resonance Positions versus Bond Length..........24

Figure 2.1 Schematic of the ISEELS Spectrometer..................30

Figure 2.2 Comparison of Spectra from Old and New Analyzers......34

Figure 2.3 Schematic of the ISEELS Electronics...................39

Figure 3.1 Coordinates in Angle Resolved Photoemission...........47

Figure 4.1 Carbon K-Shell ISEELS and NEXAFS Spectra of Benzene With Backgrounds..54

Figure 4.2 Carbon K-Shell ISEELS and NEXAFS Spectra of Benzene Background Subtracted...................................59

Figure 4.3 Comparison of Carbon K-Shell ISEELS Spectra with an MSX$_\alpha$ Calculation.......................................61

Figure 4.4 Carbon K-Shell ISEELS and NEXAFS Spectra of Pyridine..64

Figure 4.5 Carbon and Nitrogen ISEELS Spectra of Pyridine at Improved Resolution.......................................66

Figure 4.6 Nitrogen K-Shell ISEELS and NEXAFS Spectra of Pyridine..70

Figure 5.1 Carbon K-Shell ISEELS Spectra of C_5H_{10} and C_6H_{12}......79

Figure 5.2 Carbon K-Shell ISEELS and NEXAFS Spectra of C_6D_{12}.....83

Figure 5.3 Carbon K-Shell ISEELS Spectra of C_5H_8, C_6H_{10}, and C_8H_8..89

Figure 5.4 Carbon K-Shell ISEELS and NEXAFS Spectra of C_5H_8 92

Figure 5.5 Carbon K-Shell ISEELS and NEXAFS Spectra of C_8H_8......95

Figure 6.1 Carbon and Oxygen K-Shell ISEELS Spectra of Furan.....104

Figure 6.2 Carbon and Nitrogen K-Shell ISEELS Spectra of Pyrrole.109

Figure 6.3 Carbon and Oxygen K-Shell ISEELS Spectra of Tetrahydrofuran.....113

Figure 6.4 Carbon and Nitrogen K-Shell ISEELS Spectra of Pyrrolidine.....118

Figure 6.5 Carbon and Nitrogen K-Shell ISEELS Spectra of Piperdine.....122

Figure 7.1 Shapes and Bond Lengths of Cyclic Hydrocarbons and Heterocyclic Molecules.....132

Figure 7.2 Carbon K-Shell ISEELS Spectra of Five Membered Saturated Ring Systems.....143

Figure 7.3 Carbon K-Shell ISEELS Spectra of Six Membered Saturated Ring Systems.....144

Figure 7.4 Shape Resonance Position versus Bond Length for Z=12..146

Figure 7.5 Shape Resonance Position versus Bond Length for Z=13..150

Figure 7.6 Shape Resonance Position versus Bond Length for Z=14..152

LIST OF TABLES

Table 2.1 Suppliers and purity of Molecules Analyzed............37

Table 4.1 Absolute Energies and Assignments of Carbon K-Shell Gaseous and Condensed Phase Benzene...........57

Table 4.2 Absolute Energies and Assignments of Carbon K-Shell Gaseous and Condensed Phase Pyridine..........65

Table 4.3 Absolute Energies and Assignments of Nitrogen K-Shell Gaseous and Condensed Phase Pyridine..........73

Table 4.4 Widths of $1s \dashrightarrow \pi^*$ Features in Gaseous and Condensed Phases of Benzene and Pyridine..............75

Table 5.1 Absolute Energies and Assignments of Carbon K-Shell Spectra of Gaseous C_5H_{10} and C_6H_{12}............81

Table 5.2 Absolute Energies and Assignments of Carbon K-Shell Spectra of Condensed Phase C_6D_{12}..............86

Table 5.3 Absolute Energies and Assignments of Carbon K-Shell Spectra of C_5H_8 and C_6H_{12}......................90

Table 5.4 Absolute Energies and Assignments of Carbon K-Shell Spectra of Condensed Phase C_5H_8..............93

Table 5.5 Absolute Energies and Assignments of Carbon K-Shell Spectra of Gaseous and Condensed Phase C_8H_8...96

Table 6.1 Absolute Energies and Assignments of Carbon and Oxygen K-Shell Spectra of Gaseous Furan...........105

Table 6.2 Absolute Energies and Assignments of Carbon and Nitrogen K-Shell Spectra of Gaseous Pyrrole.......111

Table 6.3 Absolute Energies and Assignments of Carbon and Oxygen K-Shell Spectra of Gaseous Tetrahydrofuran.115

Table 6.4 Absolute Energies and Assignments of Carbon and Nitrogen K-Shell Spectra of Gaseous Pyrrolidine...119

Table 6.5 Absolute Energies and Assignments of Carbon and Nitrogen K-Shell Spectra of Gaseous Piperdine.....124

Table 7.1 Shape Resonance Position and Bond Lengths for Z=12....147

Table 7.2 Shape Resonance Position and Bond Lengths for Z=13....151

Table 7.3 Shape Resonance Position and Bond Lengths for Z=14....153

CHAPTER 1

INTRODUCTION

1.1 General Introduction

Electron energy loss spectroscopy(EELS) has emerged, over the last two decades, as a powerful technique for exploring the electronic and vibrational structure of atoms and molecules. Although the energy losses that are associated with inelastic scattering of electrons were first observed by Franck and Hertz in the early part of this century[FH14], progress as a useable technique was initially very slow. In the 1960's dramatic improvements in vacuum techniques and electron optics technology allowed EELS to develop to the point it has reached today[BB81]. While the various ways that EELS have been applied are interesting, this work is concerned primarily with inner shell electron energy loss spectroscopy(ISEELS) and its application to studies of the excitation of the inner shell electrons of gas phase species. Some of the data presented will be compared with solid and monolayer spectra recorded by the Near Edge X-ray Absorption Fine Structure(NEXAFS) technique[SSJ85]. Such comparisons have been shown to be quite useful in assigning spectral features of molecules. The energy loss technique provides information equivalent to that from photoabsorption when it is carried out in the limit of small momentum transfer. A recent bibliography summarizes much of the available data in inner-shell excitation that are currently available[H82 and unpublished updates].

In electron energy loss spectroscopy, often referred to as electron impact spectroscopy, a beam of electrons is accelerated by a potential difference, towards the target species from the electron source. The electrons interact with the target in a field free region and can be elastically or inelastically scattered. Those that undergo inelastic collisions lose energy in exciting the target. This process can be shown as;

$$T + e(E_o) \rightarrow T^*(E_n) + e(E_1, \theta); \qquad 1.1.1$$

where T is the target, $e(E_o)$ is the incident electron with energy E_o, T^* (E_n) is the excited target having excitation energy E_n and $e(E_1, \theta)$ is the inelastic electron, scattered through an angle θ with energy E_1. Conservation of energy gives;

$$E_o = E_n + E_1 + E_t \qquad 1.1.2$$

Here E_t is the translational energy given to the target. The very large difference between the masses of the electron and the target makes this term very small and it is neglected. This allows EELS to give a direct measurement of the excitation energy(E_n) by;

$$E_n = E_o - E_1 \qquad 1.1.3$$

Therefore, EELS is an alternative method to photoabsorption for measuring the energy of transitions between the ground and excited states of targets.

1.2 Aspects of Inner Shell Electron Energy Loss Spectroscopy

Of the energy loss techniques being used, a large portion deal with transitions from electrons in valence levels. Inner shell excitations are easily identified from valence excitation by their differences in energies. Valence shell excitation and ionization can be defined as those processes occurring at energy losses of less than approximately 50eV. This corresponds to equivalent photon energies from the infrared to ultraviolet and vacuum ultraviolet regions. Inner-shell energy losses, on the other hand, are always above 50eV and typically of the order of hundreds of electron volts. This is the region of photon energies of soft X-rays. In all of the work done for this thesis, the energy losses were less that 600 electron volts. In addition to the differences in energies, inner-shell excitation spectra are often much easier to interpret than the valence shell spectrum of the same molecule. This can be easily understood, since the inner-shell electrons are localized on the atomic cores and are very atomic-like in character. The effect of this is to have fewer initial states from which transitions can occur. This leads to spectra which are much less complex than those produced by excitation of valence electrons.

In this thesis, ISEELS is used to reproduce the same spectral features that would be expected from photoabsorption. This allows use of optical electric dipole selection rules to predict or interpret the spectra. Optical or electric-dipole allowed transitions dominate EELS when the E_o/E_n ratio is high and the scattering angle, θ, is small(see Section 1.2.2). Electron energy loss also has the advantage of being able to excite non-dipole and spin exchange transitions. Non-dipole transitions are possible if the scattering angle is large, while spin exchange transitions will occur if the ratio of $E_o/E_n \simeq 1$(i.e. close to the threshold for excitation E_n). While such excitations are of interest, they were not important factors in this thesis and will not be given any further consideration.

A brief aside to explain some terms is required before continuing.

The terms core and inner-shell will be used to describe the non-bonding electrons being excited. They will be interchanged freely as will the quantum chemical (1s,2s,2p etc.) and the X-ray absorption notations(K, L_1 and L_{23} etc.).

1.2.1 Virtual Photon Model

To explain how an electron beam can give equivalent results to a photon beam a semiempirical approach known as the virtual photon model can be used[C71]. Under conditions of fast electron impact and small angle scattering, the impact parameter, b, (see Figure 1.1 a) is larger than the dimensions of the target. The electric field, associated with the electron, is sharply pulsed in time and is uniform with respect to the target. As the velocity of the electrons is increased, the electric field becomes more sharply pulsed until it approaches a delta function (Figure 1.1b). If a fourier transform is performed, the result will have equal coefficients for the transform function, regardless of the frequency. Thus this is similar to the electric field that is associated with a beam of white light.

In reality, the electron's velocity never reaches a level where there is a delta function. There will remain both perpendicular and parallel components to the electric field. However, if these components are separated, the electric field perpendicular to the electron's direction of travel is more intense than that associated with the electric field parallel to the direction of travel. Furthermore, it is more sharply pulsed(Figure 1.1c and d) and thus over a range of frequencies the coefficients of

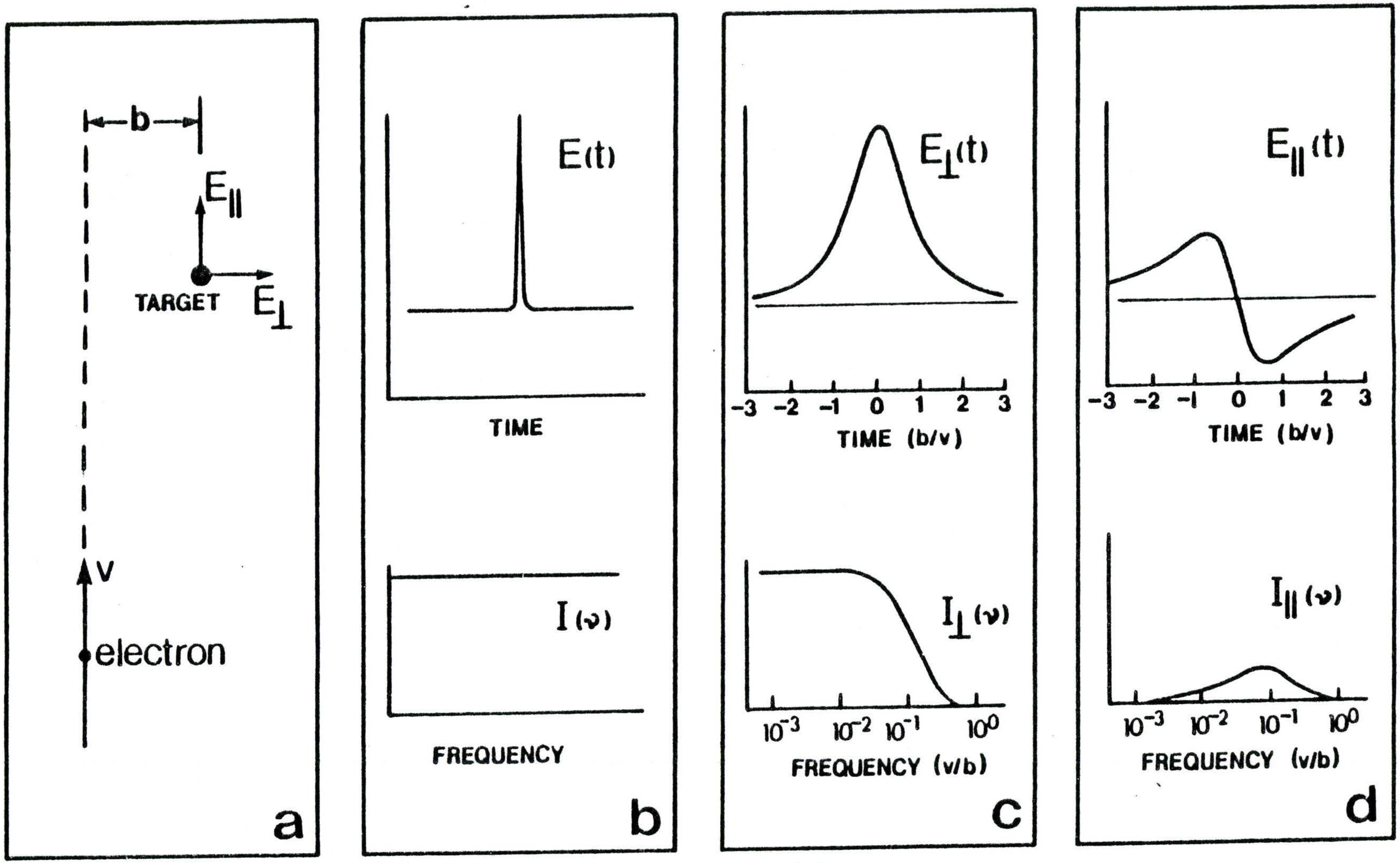

Figure 1.1 Electric field, E(t), and corresponding frequency spectrum, I(ν), associated with a distant collision of a fast electron with a molecular target. Collision parameters; v , electron velocity and b, impact parameter, c and d, realistic picture

the fourier transform frequency-domain function are equal. If the experimental conditions are chosen such that this situation exists then the analogy to white light is maintained. This will result in spectra which exhibit similar transitions from either electrons or photons. Empirically, it is found that the conditions necessary to maintain this similarity occur when the incident beam energy is greater than approximately 5 x E_n and angle of scatter(θ)is less than five degrees. A more complete treatment of this topic may be found in [W74].

1.2.2 Further Theory

While the virtual photon model provides an understanding of how an electron can behave as a photon for purposes of excitation, to calculate parameters and to fully understand the phenomena a full quantum mechanical treatment must be performed. Such a treatment has been done admirably elsewhere[W74,H78]. A brief review of the theory will be given in the following section.

The theory of small momentum transfer in electron-atom or electron-molecule interactions was first described in the 1930's by Bethe[B30]. This work has been detailed by Inokuti[I71] and the basic principles found in many standard physical chemistry texts[L78,A71]. The basis of Bethe's scattering theory is the first Born approximation and as a result it is often termed the Bethe-Born theory. The first Born approximation assumes that the interaction between the electron and the target is weak. The electron, pictured as a plane wave, is thus not significantly distorted by the interaction.

Among the most important results of the Bethe theory is the relationship between the electron impact collision cross sections and generalized or optical oscillator strengths. The differential cross section(DCS), $d\sigma(E,\theta)/d\Omega$, is the number of incident electrons scattered through an angle θ into a solid angle $d\Omega$ after exciting the target, divided by the total number of electrons per unit area per second[S84]. While this term is useful, one usually uses the generalized oscillator strength(GOS) from atomic physics which was introduced by Bethe[B30]. The expression for the GOS has the form;

$$f_n(K) = (E_n/2\ K^{-2})|\varepsilon_{On}(K)| \qquad 1.2.1$$

where K is the momentum transfer variable and $\varepsilon_{On}(K)$ a matrix element describing the transition from the state $|\psi_O\rangle$ to the state $|\psi_n\rangle$ with the form;

$$\varepsilon_{On}(K) = \langle\psi_n|\exp(i\vec{K}\cdot\vec{r}_s)|\psi_O\rangle \qquad 1.2.2$$

The magnitude of the vector $\vec{K}$ is defined by the expression;

$$|\vec{K}|=|\vec{k}_0 - \vec{k}_1|= [k_0{}^2 + k_1{}^2 - 2k_0k_1\cos\theta]^{1/2} \qquad 1.2.3$$

The GOS ($f_n(K)$), is a generalization of the optical oscillator strength f_n which has the form;

$$f_n = (E_n/2)\varepsilon_{1_{on}}{}^2 \qquad 1.2.4$$

where $\varepsilon_{1_{on}}$ is the matrix element for the electric dipole transition from the ground state(o) the the excited state(n). The quantity f_n is proportional to the photoabsorption cross section. If the exponential in the matrix element(1.2.2) is expanded in a power series then;

$$\exp(i\vec{K}\cdot\vec{r}) = 1 + i(\vec{K}\cdot\vec{r}) + (i\vec{K}\cdot\vec{r})^2/2 + \quad (i\vec{K}\cdot\vec{r})^n/n! \qquad 1.2.5$$

and if ψ_o and ψ_n are orthogonal then;

$$\epsilon_{on}(K) = \varepsilon_1(iK) + \varepsilon_2(iK)^2 + \varepsilon_3(iK)^3 + \ldots \qquad 1.2.6$$

and

$$f_n(K) = (E_n/2)[\varepsilon_1{}^2 + (\varepsilon_2{}^2 - 2\varepsilon_1\varepsilon_3)K^2 + \ldots O(K^4)] \; 1.2.7$$

thus;

$$\lim_{k\to 0} f_n(K) = f_n(\text{optical}) \qquad 1.2.8$$

Equation 1.2.7 provides the connection between photoabsorption and fast electron impact. The limit $K\to 0$ is approached when $\theta \simeq 0^o$ and the impact velocity is high. If the incident energy is much greater than the transition energy and θ is small, then the electron energy loss DCS is related to the optical oscillator strength by [I71];

$$d\sigma_n/d\Omega = cE_oE_n^{-3}f_n(\text{optical}) \qquad 1.2.9$$

where c is a numerical constant. The optical cross section and the optical oscillator strength are directly proportional and thus the electron energy loss and photoabsorption spectra are related simply through the E_n^{-3} factor. The E_n^{-3} factor has implications on the useful range in electron energy loss experiments since the intensities decrease rapidly as E_n increases.

1.3 Comparison of ISEELS and Photoabsorption

Having established, semi-empirically, a relationship between energy loss measurements and photoabsorption, and having shown that such a relationship has to be examined by quantum theory, it is pertinent to now discuss the relative merits of the two techniques. Indeed, one may question the usefulness of a technique employing electrons when an optical technique is available. Since the use of photoabsorption is well documented in the UV and IR energy regions and the theory involved in excitation well known, it would appear that staying with such a well established technique would be advantageous. The difficulty in extending photoabsorption to the inner shell region is based on the radiation required and as a result ISEELS in the dipole regime was able to develop as a viable technique with several advantages over its photoabsortion counterpart.

To excite an atom or molecule by photoabsorption the energy of the photon must be exactly equal to the energy of transition, E_n - i.e. photoabsorption is a resonant process. To excite core electrons of second and third row elements, the photon energy must be in the soft X-ray region of the spectrum. There are two main sources of soft X-ray radiation currently available. These are: bremstrahlung and electron synchrotron radiation. Bremstrahlung, which results when an electron is slowed in the coulombic fields of an atom, can provide only low intensity radiation and has not been extensively used. Electron synchrotron sources have only been developed in the last decade. Although they are rapidly becoming more available and useful, inner shell excitation studies by photoabsortion still suffer from the inherent difficulties in using soft X-ray photons.

The inelastic electron scattering cross-section of atoms or molecules is on the order of 10^5 greater than the (soft X-ray) photoabsorption cross-section. As a result, path lengths for inner shell electron energy loss work can be much smaller(e.g. 1 cm at approximately 10^{-4} torr versus 10 cm at 1-100 torr). To achieve similar intensities of signals, photoabsorption requires very long pathlengths or much higher pressures, both which may be impractical. Monochromating soft X-ray photons is difficult. Mechanical gratings are usually used. These must be carefully chosen as soft X-rays are readily absorbed on many surfaces and not well reflected. To maximize reflection, it is often necessary to use grazing incidence which requires extremely high mechanical precision and perfectly smooth surfaces. Potentially even more significant is the fact that these gratings may become contaminated with carbon deposits even if ultra high vacuum($<10^{-9}$ torr) is used. Since a large portion of the interesting molecules are organic, careful incident photon flux normalization must be performed in carbon K-shell photoabsorption to eliminate any artificial features introduced by contamination of the surfaces of optical compoments. In electron synchrotron radiation, the most intense portion of the beam is in the hard X-ray region and care must be taken to avoid order overlapping, which will superimpose this radiation with the desired radiation. Finally, the availability of synchrotron sources is not great, and their cost enormous. All of these difficulties make EELS an attractive alternative to photoabsorption for studying inner-shell excitation.

Electron energy loss is not a resonant process and thus it is not necessary for the incident electron to have exactly the energy of the desired transition. The incoming electron need only have energy equal to or greater than that of the desired transition. After the collision the inelastically scattered electrons are focussed, energy selected and detected. If the energy selection is done using retardation and a constant analyser voltage, it is possible to maintain constant resolution over the entire spectral range. Since the energy of the incident electrons is determined only by the potential difference between the electron source and the collision region, it is possible, with minor modifications, to use EELS to measure from the infrared to hard X-ray region of the spectrum. An important advantage of ISEELS over photoabsorption is its ability to achieve higher resolutions than photoabsorption at large excitation energies. Although this feature was not exploited in this thesis, resolutions of less than 100 meV have been demonstrated by energy selection of the incident beam[TKB76,KTR77,KRT77,H78]. Resolutions of 75 meV in the nitrogen K spectrum of N_2 [KRT77] correspond to a wavelength of 0.006Å(at 31Å). This resolution is better than any published optical experiments. EELS has a further advantage of being able to excite non-dipole and spin exchange transitionsas noted earlier.

This is not to say that ISEELS techniques are free from difficulties and limitations. The most serious limitation is in the E_n^{-3} factor(equation 1.2.8). This sets a practical upper limit to

ISEELS work. Commercial ISEELS spectrometers are not available, so the researcher must be familiar with the appropriate instrumental technologies(high vacuum, mechanical, electronics). Care must be taken to avoid high voltage breakdowns and voltage drifts which can destroy a potentially useful spectrum. The reduced penetration of electrons, compared to X-rays, has resulted in their application to condensed phases not being as wide spread as photons. This reduced penetration does have advantages for surface analysis and the development of condensed phase ISEELS techniques has begun[BB81].

In general then, one finds that optical techniques tend to be superior at transition energies of less than 200 eV. Between 200-1,000 eV, the region for excitation of second and third row core electrons, electron techniques are more favourable and above 1,000 eV, optical techniques again are preferred.

1.4 Interpretation of ISEELS Spectra

In the interpretation of ISEELS spectra, it is usually sufficient to describe the excitations in terms of a one electron, frozen orbital framework. Since all the spectra found in this thesis were recorded under small momentum transfer conditions, optical dipole selection rules apply and no discussion will be given to dipole forbidden transitions. The excitations observed in ISEELS result from core electrons being promoted to unoccupied or partially occupied orbitals. It is possible to have transitions to states which are below and above the ionization potential(IP) of the electron being excited. States below the IP are considered to be bound states, while those above are quasibound continuum states, or, as they are often referred to, resonances. In addition, the continuum sometimes exhibits weak features due to two electron processes such as double excitation(simultaneous promotion of a core and a valence electron), shake-up(excitation plus ionization) and shake-off(double ionization)[S84].

1.4.1 Bound Resonances

The ionization potential(I.P.), which defines whether a particular state is bound or not, is described in the gas phase as the binding energy of the electron relative to the vacuum level, E_v. In solid and chemisorbed studies the IP is measured relative to the Fermi energy of the solid or metal. Of the features in gas phase spectra that occur below the IP of the core electron, there are two types: promotion to partially or fully unoccupied molecular levels and promotion to non-bonding Rydberg orbitals(see Figure 1.2).

Rydberg orbitals are atomic-like orbitals with large radial extent and thus are diffuse. Since they are so large, they are effectively an electron in orbit around a positively charged ion

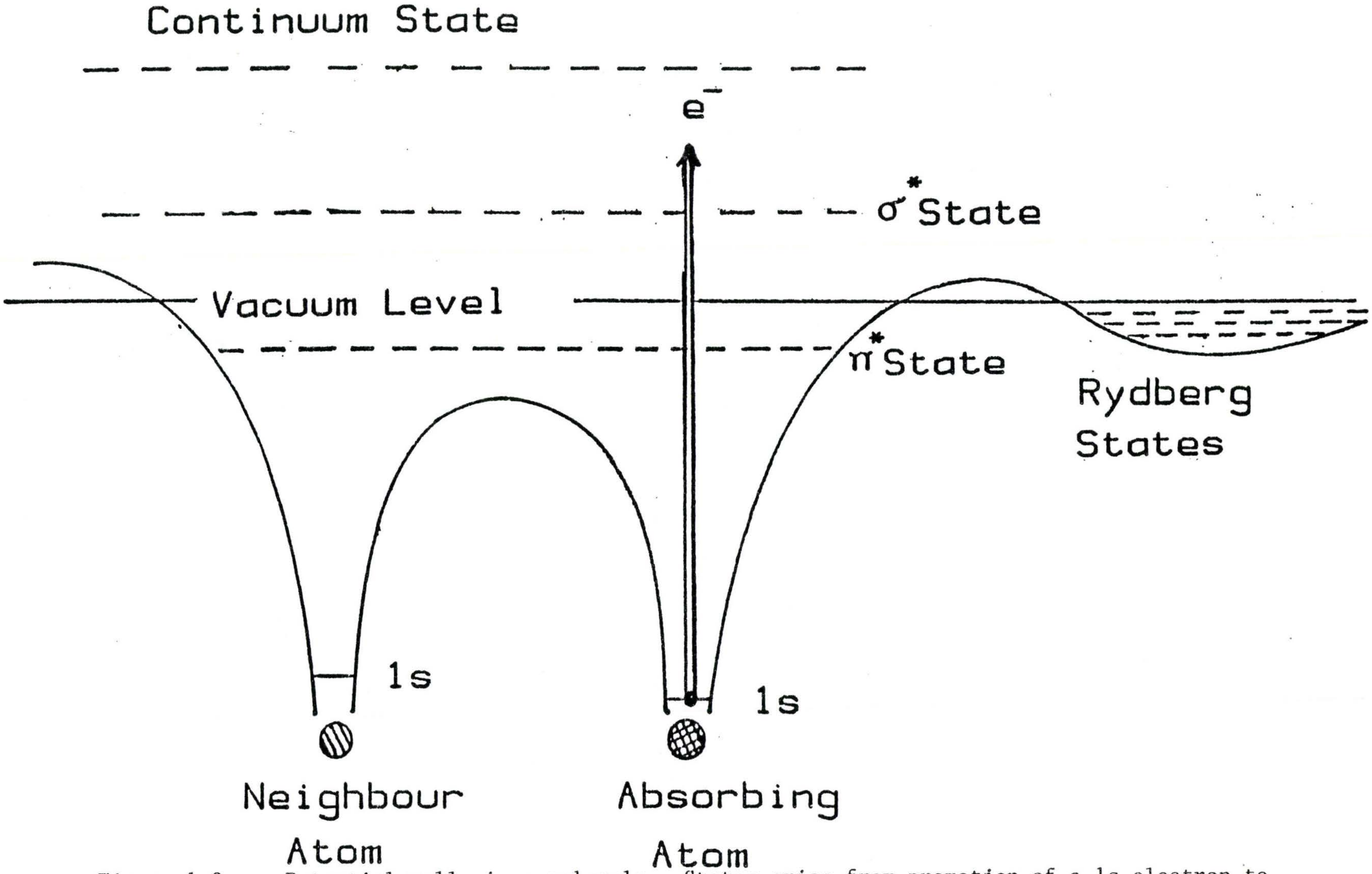

Figure 1.2 Potential wells in a molecule. States arise from promotion of a 1s electron to bound π^* states, quasibound σ^* states (inner well) or Rydberg (outer well) states.

core. Rydberg excited states are well known in the spectra of atoms and can, in general, be fitted to the formula;

$$E_{Ryd} = IP - T = IP - R/(n^*)^2 = IP - R/(n - \delta_\ell)^2; \qquad 1.4.1$$

where E_{Ryd} is the energy of the Rydberg orbital, T is the term value and IP the ionization potential[R75]. The term value, T, can be expressed in terms of R, the Rydberg constant, divided by n^{*2}, the effective quantum number. The value of n^* may be defined in terms of the difference between n, the principle quantum number, and δ_ℓ the quantum defect, which is characteristic of the angular momentum quantum number. The quantum defect is related to how much a particular Rydberg orbital penetrates the atomic(or molecular) core. The value of δ_ℓ varies considerably in some cases, but empirical values, determined by Robin[R75], place typical values for a second row element at 1, 0.6 and 0.1 for s, p and d type orbitals respectively. Transitions to Rydberg states result in a regular series of features which converge at the ionization threshold of the excited electron.

In the spectra of molecules, transitions to Rydberg levels are usually weak. Instead, enhanced intensities both above and below the IP occur. These shape resonances were first described by Dehmer and Dill [DD76] and will be discussed in Section 1.5. When such resonances are bound, they indicate transitions to partially filled or antibonding molecular orbitals. Such resonance states are bound because of coulombic interaction of the excited electron with the core hole which pulls the state below E_v, the vacuum energy level. The majority of bound resonances found in this thesis are to antibonding π^* molecular orbitals. Such 'discrete' shape resonances can be very intense due to potential barriers(see Section 1.5). Molecular orbitals are described as "inner well" transitions, while Rydberg transitions are "outer well"(see Figure 1.2).

1.4.2 Continuum Resonances

Beyond the ionization limit of a molecule, many features are still identifiable. In some cases such features can be the most intense in the spectrum. These features are often described as quasibound with the electron excited to a level above the IP, but trapped around the molecule by a barrier. Barriers due to centrifugal and potential effects have been described [DD76,NF68,D72]. The barrier results in enhanced intensities for transitions to antibonding molecular orbitals, which are generally of σ symmetry in the molecules studied. Other features observed in the continuum include multiple electron processes. The shake-up and shake-off processes are the thresholds of the satellite lines observed in XPS[SNJ69]. Generally, spectral features occur within 20 eV of the IP and thus are often termed near edge features.

1.5 Shape Resonances

In core excitation the electron being excited is atomic-like and as a result the dominant transitions might be expected to be similar to those in atomic spectra, namely the Rydberg 1s → np series. As data on molecules became available, this was shown not to be the case, and areas of enhanced intensities were found both above and below the IP. Furthermore, it was often difficult to even detect the presence of any Rydberg features whatsoever. In molecules with electronegative ligands, the strong features were interpreted as arising from the presence of a charge barrier which resulted in the electron being trapped in quasibound states[NF68,D72]. However, many molecules which show these enhanced intensities do not have electronegative ligands. To describe the features in the spectra of these molecules, Dehmer and Dill, using multiple scattering X_α calculations described by Slater[SJ71], first accurately described the features in terms of shape resonances. They result from high angular momentum final states associated with centrifugal barriers by which an electron may become trapped, resulting in greater intensity at the expense of the Rydberg intensity.

The multiple scattering approach[DD76] partitions the

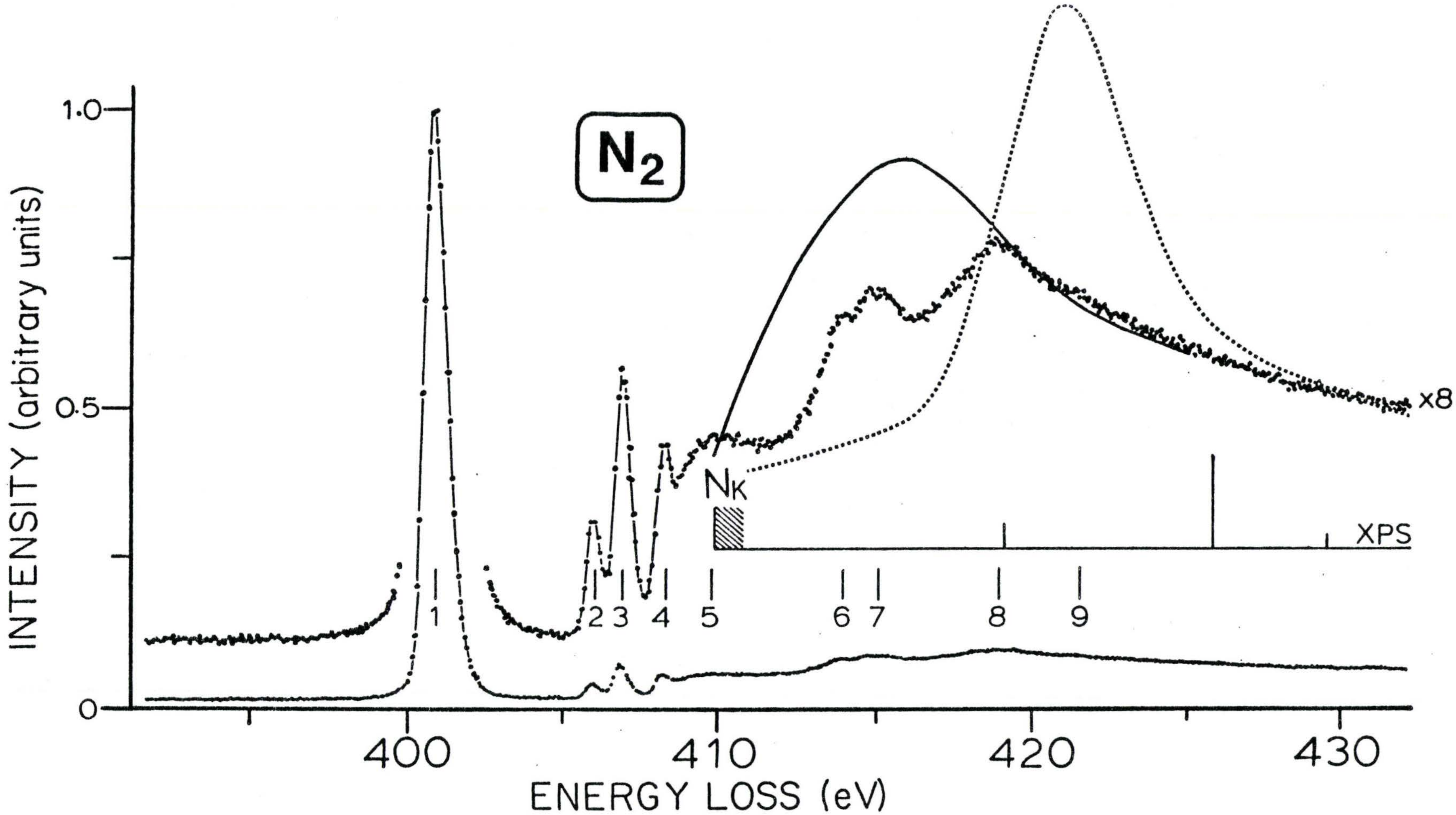

Figure 1.3 K-Shell Electron Energy Loss Spectrum of N_2 [HB80]. The solid line is the continuum shape calculated by MO techniques[RL77] while the dashed line is that calculated by MS-X_α[DD76]

molecules's field into spherical components centred upon the atoms and also one surrounding the molecule. A central potential is determined for each sphere and a partial wave solution is generated. This allowed calculation of the photoabsorption cross sections for K shell excitaion of randomly oriented molecules. This was done on N_2 for the dipole allowed channels for K-shell ionization. The results accurately reproduced the ISEELS spectrum of Wight et al[WBV73] thus assigning the dominant feature at 401.1 eV to an ℓ =2(d-wave) shape resonance(or a transition to the π^*_g orbital) and the continuum transition at 419 eV to an ℓ=3(f-wave) shape resonance(or a transition to the σ^*_u level)[DD76].

The shape resonance explanation provides a simple physical picture of the core excitation process. The photoelectron, produced by K-shell excitation, is initially considered to be an outgoing p-wave(ℓ=1) centred on the core excited atom. As this photoelectron escapes, it is scattered by the anisotropic molecular field into all allowed channels, which are made up of various angular momentum components. The partial wave expansion of the π^*_g channel in N_2 indicates that at 401 eV there is a very large d wave(ℓ=2) component. This creates the large intensity of the first peak in the spectrum (Figure 1.3).

In the case of the σ_u channel, the partial wave expansion indicates significant f-wave(ℓ=3) character. The f-wave penetrates the centrifugal barrier into the molecular core. This results in the f-wave having significant overlap with the core orbitals and the molecular field can support a quasibound state over a narrow range of energies. Further examination shows that while the molecular field can support a f-wave penetration of this type along the bond axis, it cannot do so perpendicular to the molecular axis. This result has important implications in core excitation studies of oriented molecules[SJ82 - see Chapter 3].

Although the molecular orbital picture was originally used to discuss the features seen in core excitation spectra, we now see that the multiple scattering model provides a complimentary theory that can describe, semi-quantitatively, the observed phenomena in core excitation. It is often possible to identify shape resonances if knowledge of the MO picture of the molecule in question is known, since all shape resonances identified to date can be associated with unoccupied MO's in a one-electron treatment.

1.6 Shape Resonances for Bond Length Determination

As illustrated by Dehmer and Dill[DD76], the spectral position of the σ shape resonance is sensitive to and may be quantitatively related to the bond length. This may not be too surprising if one thinks of the orientation of the bonds in simple terms. Sigma bonds are considered to arise by combining two atomic orbitals along the molecular axis. By contrast, the atomic orbitals for π type bonds are located perpendicular to the intramolecular bond and would tend to be less sensitive to bond length. The σ shape resonance is most easily pictured as a resonance scattering of the photoelectron between the excited atom and its neighbour(s). All this suggests that σ shape resonances would be sensitive to bond length.

Sette et al[SSH84] have examined a number of K shell spectra of low Z molecules and their shape resonance position. By measuring the shape resonance position E_σ, relative to the 1s binding energy, they defined a quantity δ. This quantity is the difference between the energy of the σ shape resonance and the I.P.. The determination of this value had an uncertainty of approximately ± 2 eV, associated mainly with the location of the peak of the broad resonance. The molecules were further separated into classes based on a parameter Z which was defined as the sum of the atomic numbers from the absorbing atom and the scattering atom from which the resonance results.

This treatment yielded a simple correlation between δ and R for each Z. The value of δ was found to decrease monotonically as R increased. A least squares linear fit of the available data was preformed according to;

$$\delta = m - nR \qquad 1.6.1$$

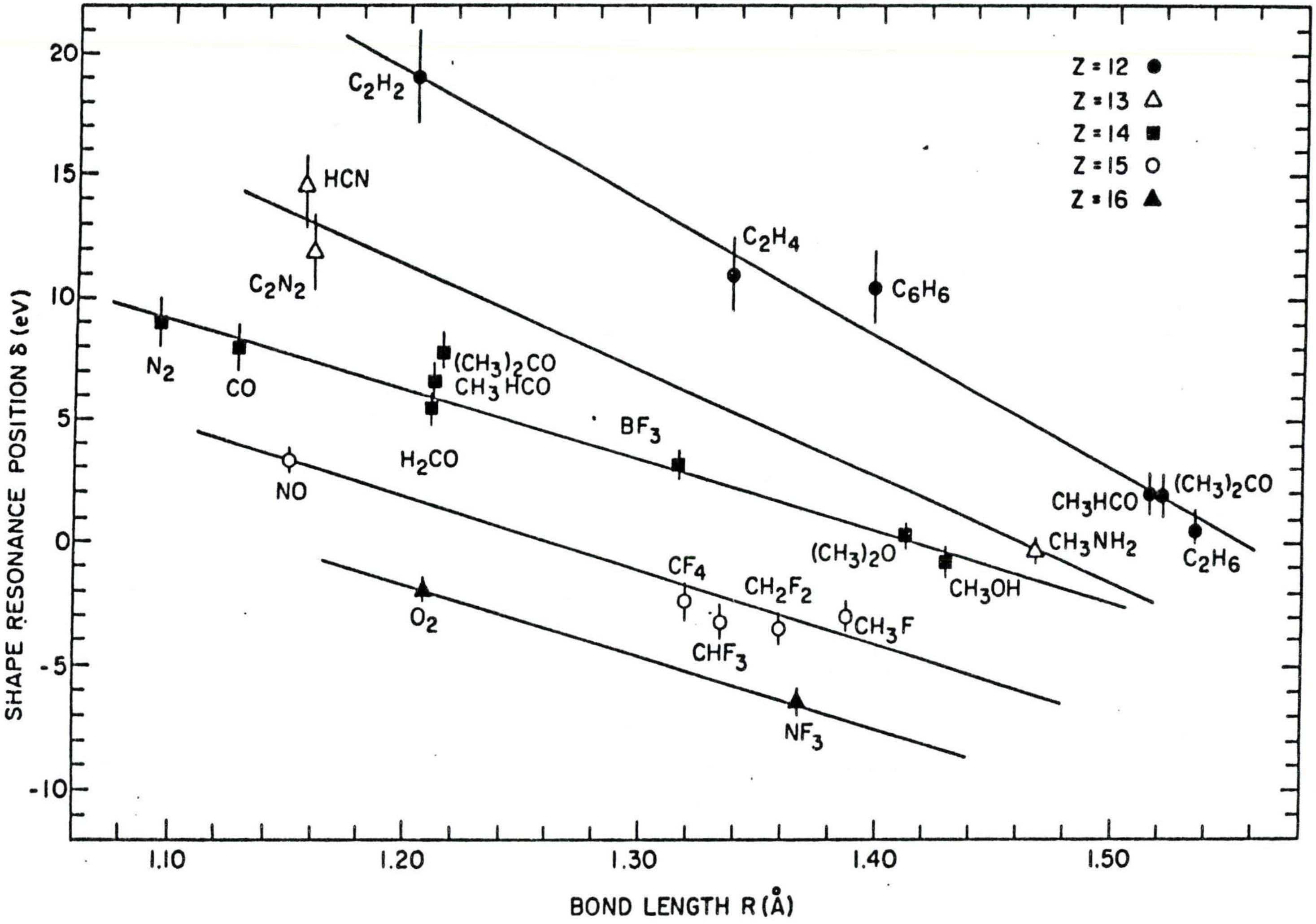

Figure 1.4 Plot of shape resonance position δ as a function of Z[SSH84]. The straight lines represent a least squares fit to the data points.

The fitted lines are superimposed on the experimental points in Figure 1.4[SSH84]. Although in some cases there is little data to give accurate correlation, good fitting with the experimental data is seen. The slopes in all cases were remarkably similar showing only small changes with the intercept decreasing as Z increases. This empirical formula has been used to predict the values of the bond lengths of perfluoro-2-butene(CF_3-CF=CF-CF_3) and gave excellent agreement with predicted results[SSH84].

Using a full multiple scattering theory, Natoli[N83] has shown that for isostructural molecules a simple relationship between δ and R exists;

$$(\delta - V_0) R^2 = C_0 \qquad 1.6.2$$

where C_0 depends on the atomic phase shifts of the atoms involved in the scattering process and V_0 is the mean intramolecular potential relative to the vacuum level. This formula is limited in its usefulness due to lack of knowledge of C_0 and the inner potential V_0. Although C_0 is energy dependent through the energy dependence of the atomic phase shifts the σ shape resonance energies fall in a region where the atomic phase shifts are smoothly varying[BDG83]. Equation 1.6.2 suggests that variations in the shapes and the intercepts of the least squares fit lines in Figure 1.4 result from changes in V_0

and/or C_o. The fact that δ varies linearly with Z indicates that V_o varies linearly with Z. It has been shown[SSH84] that V_o is proportional to Z and that C_o is nearly constant between Z=12 and Z=18. This result is derived from the empirical results and while the assumptions seem reasonable more theoretical work is required to further investigate this phenomenon. The work presented in this thesis has considerably increased the available data and, in most cases, the simple empirical relationship holds. Previously, certain molecules such as CO_2, COS, N_2O and NO_2 have been found to deviate from this relationship[SSH84]. In general, molecules with extensive delocalization do not follow the simple correlation and the predicted bond lengths are shorter than the actual bond lengths. In this work, aromatic molecules are found to exhibit similar, although less severe, deviations from the proposed correlation. An alternative interpretation of the relationship between bond lengths and continuum resonances in aromatics is presented in this thesis.

Even so, a good agreement for the relationship between shape resonance position and bond length may be made. In fact, Stöhr et al have used the empirical relationship to determine bond lengths of molecules chemisorbed to metal surfaces, with reasonable accuracy[SGE83,SSJ84]. Yet to be accomplished is a more precise theoretical treatment of this phenomena. If this can be done, it may allow either the extension of this relationship in any phase or a better understanding of the situations in which the empirically derived relationship can be applied.

CHAPTER 2

EXPERIMENTAL

2.1 Introduction

This chapter is concerned with the spectrometer and the experimental conditions used in obtaining the spectral data presented later. The spectrometer was originally constructed by T. Steel[S82]. To improve the performance of the instrument, differential pumping was added to the gun region during the course of this work. New hemispherical analyzers were obtained near the end of the experimental work and, as a result, resolution and count rates were dramatically improved. A schematic of the spectrometer is shown in Figure 2.1. A gas inlet system was also constructed to allow easy handling of both liquid and gaseous samples and calibration standards.

2.2 The Electron Source

The electron source used in the data collection was a Philips 300 television tube electron gun. Although designed to operate at much higher potentials, the gun gave reliable, stable operation at the spectrometer's operating potential(2.5 keV). The gun consists of a filament, indirectly heated cathode(C), grid(G), focus(F) and anode(A)(see Figure 2.1). The indirectly heated cathode was BaSrO. The focusing element is an Einzel lens. Although these guns did give stable operation, they were often subject to chemical attack from the sample gases. To reduce this, a differentially pumped gun region was constructed. This was accomplished by pumping the main chamber with one diffusion pump and the gun region with another. The two areas were separated by a Delrin block. Thus the only path for the gas to enter the gun region was through the electron beam path. While this was sucessful in keeping the pressure in the gun region more stable, the more reactive gases still affected the gun's lifetime. In some cases, this problem could be overcome by increasing the power to the filament. This would tend to indicate that the problem was more one of a change in the work function of the surface rather than extensive reaction of the oxide.

2.3 The Spectrometer

A brief description of how the spectrometer operates is presented here. Electrons produced in the gun region are accelerated by a potential difference towards the interaction region. This was typically the energy loss plus 2.5 keV. Deflectors D1, D2 and D3 allow for corrections in the beam path while the lens elements V1-V4

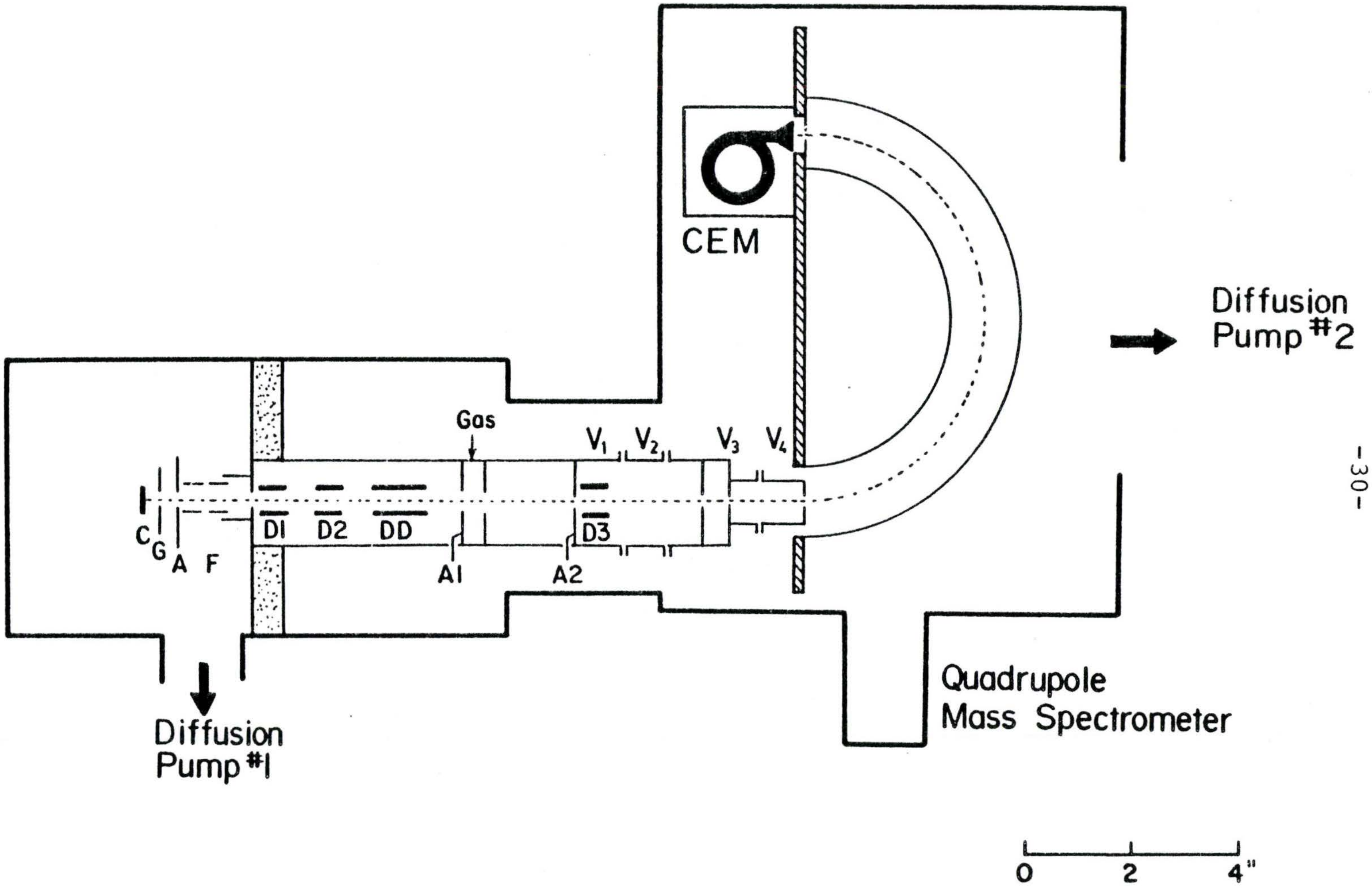

Figure 2.1 Schematic of the ISEELS Spectrometer.

retard the electrons so they are analysed at constant energy. The energy loss of interest is added on top of the accelerating potential by adding a negative potential equal to the energy loss plus the analyzer pass energy to the cathode potential.

Initially, the spectrometer is tuned on the main beam of electrons(E_{loss}= 0 eV; $\theta = 0$). By use of D1 and D2, the beam is passed through the centre of the collision chamber. This is done by maximizing then minimizing the current on the aperture plates A1 and A2, which are connected to ammeters(see Figure 2.3). The current to the cone of the detector, a channeltron continuous dynode multiplier, is then maximized by adjusting D3 and lenses V2 and V3. The cone of the channeltron operates as a Faraday cup in this situation. A set of Helmholtz coils reduces the magnetic field along the electron trajectory.

2.3.1 The Lens System

The lenses used in the spectrometer are designed to focus the electron beam and decelerate the electrons to a constant energy. The lens system consists of a three cylinder zoom lens and a two cylinder lens. Two sets of lenses are employed to keep the deceleration ratio in any one lens from becoming too large. A large deceleration ratio can lead to beam divergence and image formation in the lens field[S82].

The zoom lens provides a variable deceleration ratio of 6:1 to 3:1 for energy losses of 0-1,250 eV on a 2,500 eV incident electron beam. Although it is possible to theoretically determine the voltage ratios at various energy losses, the optimum lens voltages were not the same as theory, probably due to the interplay between the deflection plates, magnetic fields and lens. This is due to the electron beam travelling off the axis of the lens system and is unavoidable, due to difficulty in precisely aligning the electron gun axis with that of the lens stack.

2.3.2 The Analyzer

The analyzer used is a hemispherical electrostatic analyzer. The principles and theoretical considerations of various analyzers are well documented and are presented in a number of review articles[H73,S67,WGS74]. A hemispherical electrostatic analyzer was selected since it is suited to experiments which call for coupling to strongly decelerating lenses of axial symmetry, as in this setup.

The electrons, with the appropriate energy, are deflected by the $1/r^2$ electric field produced by the potential difference, V, between the two hemispheres. This is related to the pass energy, V_0, by:

$$V = V_o[(R2/R1) - (R1/R2)] \qquad 2.3.1$$

where R1 and R2 are the radii of the inner and outer spheres respectively. The theoretical resolution of the analyzer is approximated by:

$$E(\mathrm{FWHM}) = 0.01\ V_{an} \qquad 2.3.2$$

Initially, this resolution was not obtainable and resolutions of 1.0 eV full width at half maximum(FWHM) were the norm. It was suspected that the reason for the decreased resolution was stray magnetic fields and variations in the spectral voltages. It was noticed that the hemispheres used in the original construction of the spectrometer were not completely hemispherical. Initially this was not expected to cause the observed reduction in resolution. However, new hemispheres were constructed to test this near the end of this thesis. When the new analyzer was placed in the machine, an improvement in the resolution from 1.0 to 0.6 eV on the C_K signal of CO was achieved. As well, count rates improved by a factor of 100(see Figure 2.2). Although this change was made too late to repeat all of the spectra obtained, the spectra of the heterocyclic molecules presented in Chapter 6, as well as pyridine, were obtained under these much improved conditions.

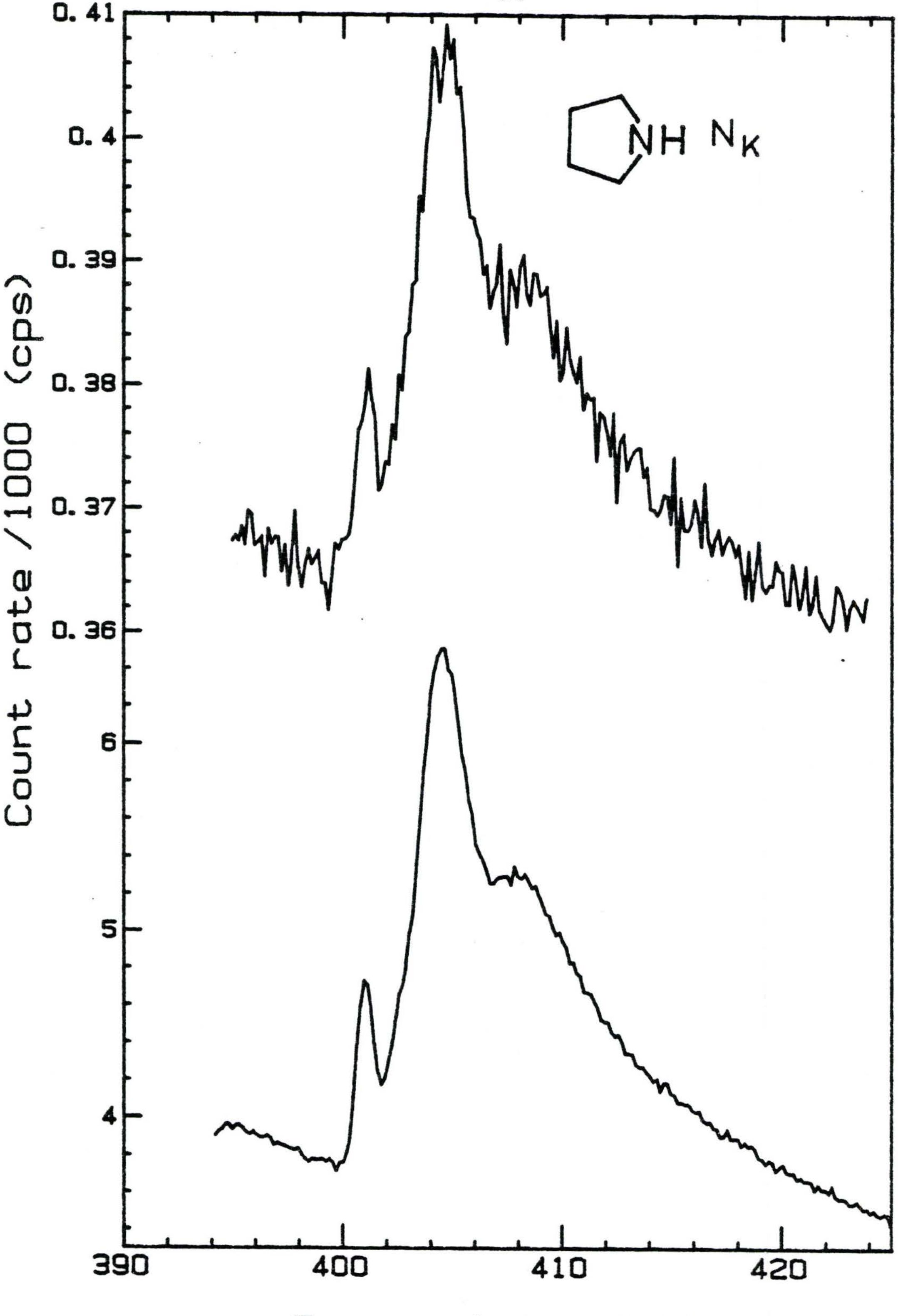

Figure 2.2 A comparison of spectra obtained by the old spectrometer(top) and the new spectrometer(bottom). The difference in resolution is approximately 0.5eV FWHM.

2.3.3 The Double Deflection System

In measuring a K-shell excitation spectrum of a molecule with this spectrometer, it is not possible to obtain useful data at zero scattering angle. This is due to a large background of electrons resulting from the scattering of the main beam and secondary electrons that are emitted when the main beam collides with the outer hemisphere of the analyzer. In order for a spectrum to be collected, the main beam is passed through a "double deflection" system. This system consists of a set of deflection plates, labelled DD in Figure 2.1, which are twice as long as D2 and located at the halfway point between D2 and the collision region. The plates operate perpendicular to the dispersive plane of the analyzer. The voltage for these plates is generated by a single voltage source. The beam is first deflected through an angle by D2 and then deflected back in the opposite direction by DD. Regardless of the deflection angle chosen, this system causes the main beam to pass through the centre of the collision region, where the gas concentration is the highest and in the viewing cone of the analyzer. The main beam is intercepted by A2 and only electrons inelastically scattered by an angle of 1-3° will be detected. This also allows the beam current to be monitored throughout the experiment.

2.4 Sample Handling

A gas inlet system, constructed during the course of this thesis, allowed liquid and gaseous samples to be introduced to the collision region of the spectrometer. The gas inlet system, which consisted of two separate lines, one for reference gases and one for samples, was pumped by a single rotary pump. The pump was equipped with a liquid N_2 trap to allow removal of condensables and chemically active species which might degrade the rotary pump oil. The gas pressure in the lines could be monitored by a Bourdon vacuum gauge, and the rate of introduction to the collision region varied by a Granville Phillips Series 203(reference line) or a Nupro Series MGD(sample line) leak valves. After the leak valves, the lines are rejoined to allow low pressure mixing of the reference and the samples. Appropriate valving allowed each line to be independently pumped. It was often necessary to pump for 1-2 hours when dealing with liquid samples to remove condensed vapour from the walls of the gas inlet line.

The samples and standards used were commercially available and of stated high purity(see Table 2.1). Highly volatile components of the liquid samples were removed by several freeze, pump, thaw cycles.

Table 2.1

Supplier and Purity of Molecules Analyzed

Molecule	Purity(%)	Supplier	Molecule	Purity(%)	Supplier
CO	99.99	Matheson	C_2H_2	99.5	Can. Liq.
N_2	99.99	Matheson	C_2H_4	99.0	Can. Liq.
Benzene	99.0	BDH	Cyclopentane	98.0	Aldrich
Pyridine	99.5	Canlab	Cyclopentene	99.0	Aldrich
Cyclohexane	99.0	BDH	Cyclooctatetraene	98.0	Aldrich
Furan	99.0	Aldrich	Pyrrole	98	Aldrich
THF	99.5	BDH	Pyrrolidine	98	BDH
piperdine	98	BDH	CO_2	99.99	Can. Liq.

2.5 Energy Calibration

All energy scales were determined by calibrating the energy scale of the spectrum of the unknown to a feature of known energy from a reference molecule. This is necessary because the spectrometer energy scale is slightly dependent on the gas being studied, due to changes in surface electrostatic potentials caused by gas adsorption. In the case of C_K spectra, the 1s → π* peak of CO was generally used. This peak is known accurately to be at 287.40 eV[SB84]. In cases where this peak overlapped with features in the sample spectrum, the 1s → π* features in C_2H_2(285.9 eV) or C_2H_4(284.68 eV) were used[HB77]. To calibrate N_2 spectra, the 1s → π* peak of N_2(401.10 eV) was used and for O_K spectra, the 1s → π* peak of CO(533.5 eV) was used[SB84]. The sample and the reference were introduced at various concentration ratios to check for apparent peak shifts caused by spectral overlap. The energy difference between the sample and the calibrant was determined and the sample's energy scale established with this value.

2.6 Spectral Acquisition

Spectra were typically collected in the following manner: the sample, or reference and sample, were introduced into the collision region. After tuning on the main beam, the energy loss and

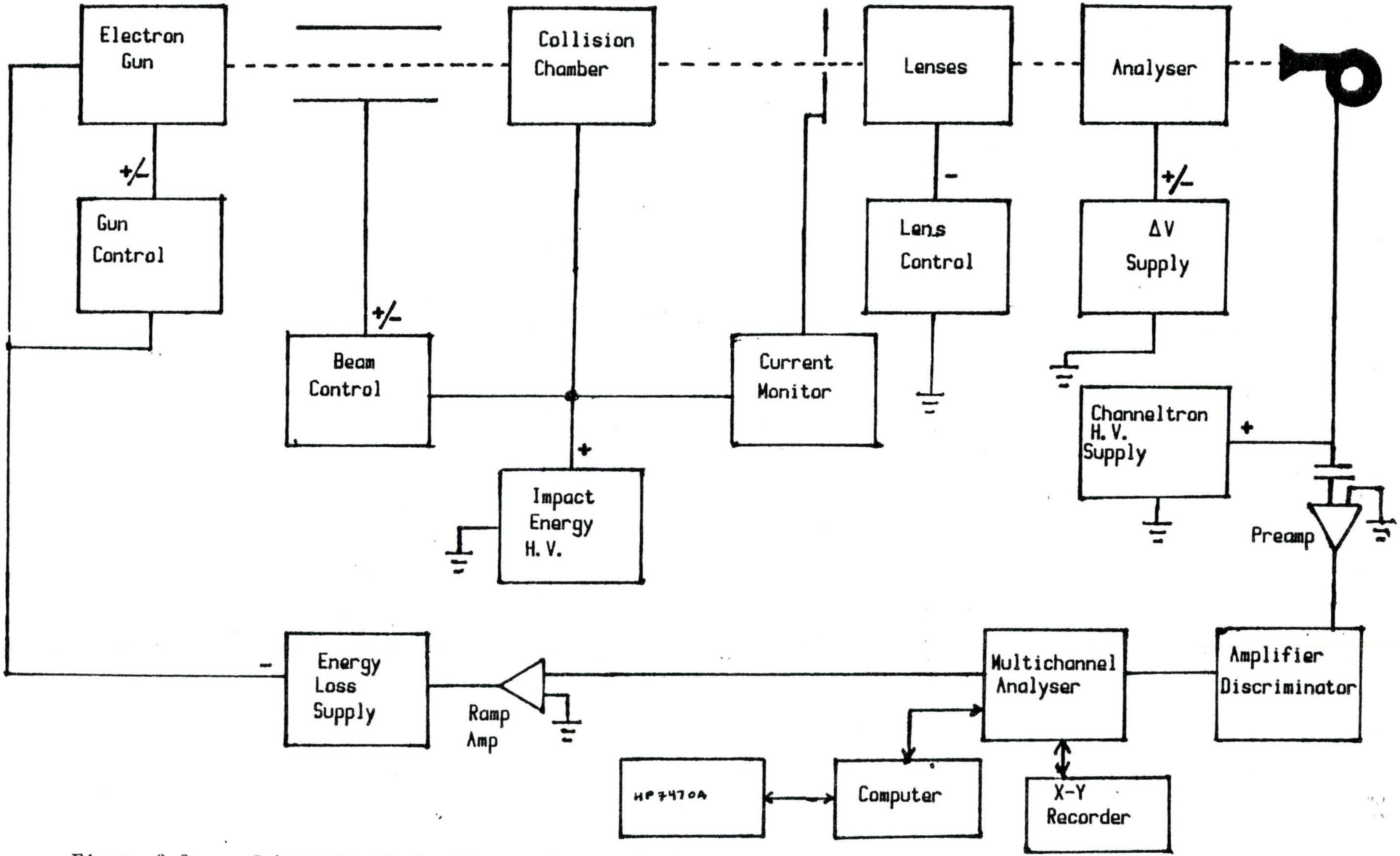

Figure 2.3 Schematic of the Electronics used with the ISEELS Spectrometer.

spectral width were set and the beam deflected by the double deflection system. The channeltron's high voltage was then applied and the detector set up in pulse counting mode. The start and stop voltages were determined with a 4.5 digit Keithley 175 Autoranging or Fluke 8060A Multimeter. The detector produced pulses from the inelastically scattered electrons and these were processed using standard counting techniques. The spectra were collected on a Nicolet 1170 signal averager which also supplies a 0 to 10 volt ramp, appropriately amplified to allow for continual scanning. The acquisition time varied depending on the resolution, number of data points, count rate and energy region studied. With the construction of new hemispheres, the acquisition times decreased dramatically.

Once collected the spectra could be transfered to a PDP-11 microcomputer. Spectra of calibration runs were plotted on an XY recorder for energy scale determination. The spectra stored in the computer could then be calibrated, truncated and background subtracted as required. The plots presented in this thesis were prepared on a HP7470A plotter. An overall schematic of the spectrometer electronics and data system is shown in Figure 2.3.

CHAPTER 3

INTEGRATION OF GAS PHASE AND CONDENSED PHASE CORE EXCITATION STUDIES

3.1 Introduction

In section 1.3, the advantages of ISEELS over photoabsorption studies were discussed. However, regardless of this, many studies of inner shell excitation in low Z containing molecules are being done by photoabsorption. This proves to be advantageous for it provides a check on the accuracy and a measure of the degree of dipole domination of both the photoabsorption and ISEELS spectra when they are performed on the same molecule. However, relatively few gas phase photoabsorption experiments have been done especially at the carbon K-edge. Recently, a considerable number of photoabsorption studies have been done on inner shell excitation in solids and chemisorbed layers where they are often referred to as XANES or NEXAFS. XANES refers to X-ray Absorption Near Edge Structure and NEXAFS refers to Near Edge X-ray Absorption Fine Structure. They both deal with features observed within approximately 20-30 eV of the photoabsorption edge. This is in contrast to EXAFS, Extended X-ray Absorption Fine Structure, which are features found beyond the absorption edges, up to several hundred volts[S77].

In an ISEELS spectrum of a molecule, the resulting transitions that are observed are due to intramolecular transitions in randomly oriented molecules. Any additional features that are observed in the condensed phase spectra would be interpreted as resulting from intermolecular transitions. Solid phase NEXAFS spectra will quench Rydberg features, thus identifying them in the gas phase. More interesting is the ability of chemisorbed NEXAFS spectra to predict, if the chemisorbed geometry is known, features that can be attributed to final states of σ or π symmetry. Thus the combination of gas phase, solid phase and chemisorbed spectra of the same molecule can allow for unambiguous assignments of all peaks in the spectra.

Why should we show any concern about solids and particularily chemisorption when the main emphasis of this thesis is ISEELS? The reasoning is simple; ISEELS as a technique does provide useful information, but there are limited practical applications of the spectroscopy of randomly oriented, isolated gas phase molecules. Perhaps the area of physics and physical chemistry that has grown the most over the past decade is in the field collectively known as surface science. Such growth is not surprising, since many important chemical and physical processes cannot be known unless what is occurring on the surface is understood at the atomic level. Furthermore, as the surface to area ratio continues to decrease in semiconductors, a more accurate description of surfaces and how they interact with various environments is desirable. In this, ISEELS allows development of a good understanding of core excitation molecular spectroscopy by determining the spectra of molecules of known geometry and calculable electronic structure. It has helped open the way for inner shell electron energy loss techniques to be extended to solids and surfaces, providing another independent source of information. Therefore, to accurately characterize the core spectroscopy of a molecule, it has been found useful to combine the ISEELS and NEXAFS data.

3.2 Near Edge X-ray Absorption Fine Structure

Although NEXAFS employs photons as its source of excitation, it is not precisely a photoabsorption technique. The normal method of detection is one that measures the electron yield from various excitations[S83]. This may be accomplished by measuring the Elastic Auger Yield(EAY), Partial Auger Yield(PAY), Total Electron Yield (TEY) or the Secondary Electron Yield(SEY). In the first two cases, the intensity of a particular Auger transition is measured as a function of photon energy. In EAY, the Auger electrons which have not suffered any energy loss are monitored, while PAY only detects those with energy greater than a cut off energy E_p. The former allows the best signal to background ratio, but the poorest signal. The latter gives an improved signal, but at the cost of a lower signal to background ratio. The PAY detection scheme is well suited to low Z atoms. In TEY, all emitted electrons including Auger electrons, photoelectrons and inelastically scattered electrons are detected. The TEY measurements are simple and provide higher counts but lower signal to background compared to the EAY technique. The SEY detection technique measures a portion of the low energy inelastic electrons and the spectra are similar, in practice, to the TEY method, although TEY has higher count rates. In these methods, the intensity of the electron current, from the electron multiplier, is monitored as a function of photon energy. Generally, the spectra produced are similar to photoabsorption studies, if all the K shell hole states have the same decay probabilities. In principle, above the K shell IP the electron yield will at least double, since both directly ionized and Auger electrons are produced. In photoelectron yield studies from condensed phases, the higher energy Auger electrons produce several secondary electrons and thus dominate the electron yield.

The experimental details involved in NEXAFS measurements have been extensively discussed by Stöhr[S83] and will not be detailed here. It is not the goal of this section to explain the technique, but to show why it is useful in combination with ISEELS. It is most important to note that this laboratory has collaborated closely with the EXXON research facility in New Jersey. All the condensed phase data shown in this thesis is not work done by the author, but is the work of Stöhr and coworkers.

3.2.1 Comparison of Spectra

Perhaps the most immediately obvious point when comparing the spectra of a molecule in the gas phase to a molecule in the solid or even in chemisorbed states, without geometry changes, is the remarkable similarity between the spectra. This indicates that, for the most part, the spectra of all three are dominated by intramolecular transitions. Any additional feature in condensed phase spectra would indicate intermolecular transitions, while changes between the spectra will immediately point out distortions in the molecular geometry. Thus the same picture used to describe features in the gas phase can be used to describe features in solid and chemisorbed molecules in situations where the molecules are undistorted in the condensed phase. The domination of shape resonance features exist in the NEXAFS spectra of solids and monolayer just as it does in the spectra of gas phase molecules[SBJ81]. The spectra are not, however, identical. The gas phase molecule has Rydberg orbitals which collapse into the band structure of the solid when the molecule condenses. Thus, any transitions which are assigned to a Rydberg state in the gas phase spectrum generally do not appear in the condensed phase spectrum of the molecule. This behaviour was originally shown by changes in EELS as the pressure of gases was increased[R75]. The same effect has been shown in comparison of the ISEELS and NEXAFS spectra of benzene, pyridine and cyclohexane([HSH85,NHS85] Chapters 4 and 5).

While the ability of a comparison of gas and condensed phase spectra to identify Rydberg features is useful, it is not the most significant aspect of the phase dependence of the core spectra. More significant is the effect that orientation has on inner shell transitions of molecular orbitals. The NEXAFS spectra of condensed molecules show a strong polarization dependence. This is particularily true for molecules chemisorbed at monolayer or submonolayer coverage, which are usually highly oriented on the metal surface. By varying the angle of incidence of the photon beam with respect to the surface, it is possible to get controlled intensity enhancement of π and σ shape resonances, useful both for spectral assignment and determination of the molecular orientation on a surface.

The theoretical aspects of the polarization dependence of the orbitals have been outlined by Stöhr and Jaeger[SJ82]. By using the same equation which governs the peak intensities of angle resolved photoemission and retaining the symmetry of the molecular orbitals, using the angular definitions in Figure 3.1 the cross section for a diatomic molecule along the direction $\vec{k}$ is;

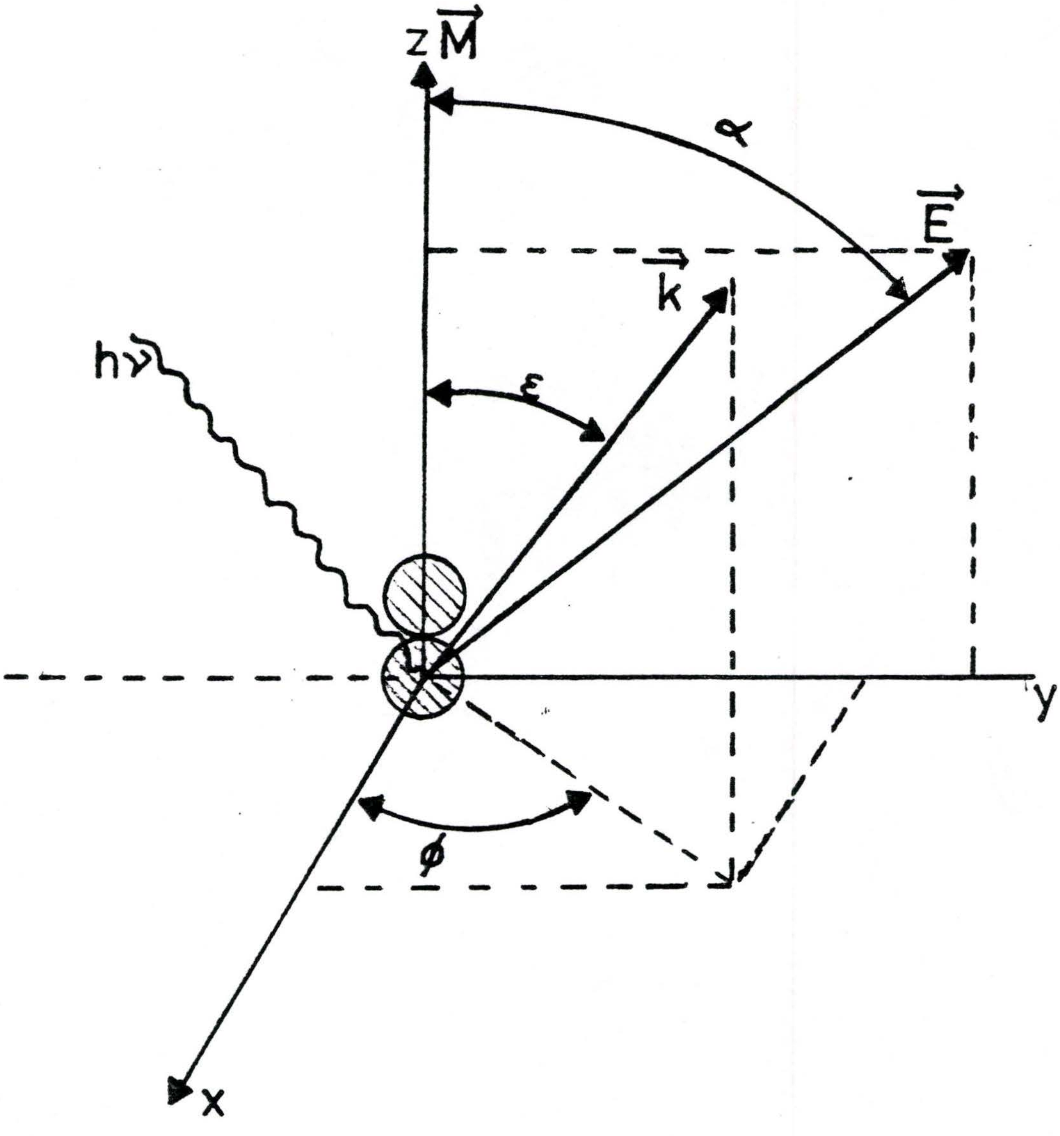

Figure 3.1 Definition of the coordinates which determine the polarization dependent angle resolved photoemission spectra from oriented molecules. $\vec{M}$ is the symmetry axis of the molecule, $\vec{E}$ the x-ray electric field vector and $\vec{k}$ the photoelectron emission direction[SJ82].

$$d^2\sigma/dk\,d\vec{M} = I(\varepsilon,\phi,\alpha) = A(\varepsilon)\cos^2\alpha + [B(\varepsilon) + C(\varepsilon)\cos 2\phi]\sin^2\alpha + D(\varepsilon)\sin\phi\sin\alpha\cos\alpha \qquad 3.1.1$$

where α is the angle between the molecular $\vec{M}$ and the electric field vector E. The direction of the photoemission is determined by the polar co-ordinates ε and ϕ. In X-ray absorption experiments, the absorption coefficient for an inner-shell excitation is determined by integration of Equation 3.1.1 over all k. This yields;

$$\mu(\alpha) = d\sigma/d\vec{M} = X\cos^2\alpha + Y\sin^2\alpha \qquad 3.1.2$$

where the coefficients X and Y are;

$$X = \sigma/4\pi(1 + \beta_m) \qquad 3.1.3$$

$$Y = \sigma/4\pi(1 - \beta_m) \qquad 3.1.4$$

Thus equation 3.1.1 can be rewritten as;

$$\mu(\alpha) = \mu_o/4\pi[1 + 1/2\ \beta_m(3\cos^2\alpha - 1)] \qquad 3.1.5$$

where μ_o is the integrated photabsorption cross section and $\beta_m = \beta_m$ (hν) is an asymmetry parameter. The value of β_m can be determined by expressing it in terms of the electric dipole amplitudes. As a result, $\beta_m=2$ and -1 for pure σ and π final states respectively. For 1s $\rightarrow \sigma$ transitions, equation 3.1.5 becomes;

$$\mu_{\sigma\sigma}(\alpha) = 3\mu_o/4\pi \cos^2\alpha \qquad 3.1.6$$

and for 1s $\rightarrow \pi$ transitions, equation 3.1.5 is;

$$\mu_{\sigma\pi}(\alpha) = 3\mu_o/4\pi \sin^2\alpha \qquad 3.1.7$$

Equations 3.1.6 and 3.1.7 show the intensity distributions for different orientations of the $\vec{E}$ vectors with respect to $\vec{M}$. When electrons are excited along the electric field vector direction for $\vec{E} \,//\, \vec{M}$ ($\alpha=0$), the final wave function must have σ symmetry($\mu_{\sigma\pi}=0$) and for $\vec{E} \perp M(\alpha=90\ )$ the final state must have π symmetry($\mu_{\sigma\sigma}=0$). According to this then σ and π final state orbitals must have opposite polarization dependence.

3.2.2 Effects of Surface Molecule Interactions

The end result of the previous discussion is that by using polarized x-rays (such as are produced by synchrotron radiation) and varying the angle of incidence, the σ and π shape resonances will be enhanced or reduced depending on the orientation of the molecule with respect to the surface. Thus, by experimentally observing changes in intensity of σ or π shape resonances, the surface orientation can be inferred. Such studies are simpler for molecules containing π resonances because of their sharpness and intensity. Studies of this sort have been carried out and are in agreement with other surface techniques capable of determining orientation[JMS83, KSG84]. Upon, chemisorption it has been found that there may be significant broadening of π shape resonances, if present. This is thought to be a result of mixing of the π^* orbitals of the chemisorbed molecule with the metallic states. This broadening was first explained by Jugnet et al for CO on Ni(III)[JHA84]. The $2\pi^*$ orbitals of the CO hybridizes with the Ni 4s, 4p states which causes the broadening. This broadening effect of the molecule/surface bonding is observed in benzene and pyridine[Chapter 4], for example.

CHAPTER 4

THE K-SHELL EXCITATION SPECTRA OF BENZENE AND PYRIDINE

4.1 Introduction

Inner shell excitation spectroscopy has proven to be a powerful technique for obtaining information on electronic structure and geometry of molecules, both in the gas phase[H82,SSH84] and adsorbed on surfaces[S84]. Most of the studies carried out prior to this thesis have dealt with relatively simple molecules where the assignments of the observed resonances is generally straight forward. The assignments of inner shell excitation spectra of more complex, aromatic molecules, such as benzene, do not appear to be as simple. In the past there have been conflicting assignments of the observed resonances[HB77,BST81,L85] and correlation to the empirical relationship between bond length and K shell resonance position developed by Sette et al[SSH84] was poor. In this chapter, the K shell excitation spectrum of benzene is reexamined in an attempt to clear up this uncertainty. The reassignment of the benzene spectrum is based on a comparison between gas phase ISEELS, solid and monolayer NEXAFS spectra and the results of an Xα multiple scattering(MS) calculation[HSH85]. The different spectral techniques, when used in combination, allow for the unambiguous identification of Rydberg and valence orbitals. Knowledge of the chemisorbed geometry can also provide information on which features are π^* or σ^* states. By applying the same treatment to the pyridine spectra, the assignment of all features is also accomplished.

The reassignment of the benzene spectra and subsequent assignment of the pyridine C_K and N_K shell spectra have allowed for aromatic molecules to be more accurately represented in the empirical relationship of Sette's[SSH84]. Analysis of the position of the K shell resonances of both molecules upon chemisorption indicates that, in contrast to simple hydrocarbons[SSJ84], there is no measurable change in the molecular geometry.

4.2 Benzene

4.2.1 Benzene Electron Energy Loss Spectrum

The gas phase K shell electron energy loss spectrum of benzene is shown at the top of Figure 4.1. This spectrum was recorded with the McMaster ISEELS spectrometer at a resolution of 1.0 eV. While previous studies were done at slightly better resolution all major resonances are resolved at the instrumental resolution available. Four major resonances 1, 3, 4 and 5 are resolved with a weaker feature(2) also present. The first feature is a 1s → π^*

transition. This is in agreement with all other studies[HB77,JMS83]. The remaining three features have uncertain assignments. Feature 3 is a bound transition and as a result was assigned to a Rydberg state by Hitchcock and Brion[HB77]. The two remaining features are continuum states. Feature 4 was assigned to a double excitation feature, while feature 5 was not assigned in [HB77].

Benzene is known to have two empty π^* orbitals which are of e_{2u} and b_{2g} symmetry[JS73]. Transitions to both states are dipole allowed and thus two resonances should be observed if they are separated enough in energy. Although Hitchcock and Brion[HB77] acknowledged the existence of these two states, they did not assign any feature to the second state. In a SCF-MO calculation Butscher et al[BST81] has assigned peaks 1 and 4 to the e_{2u} and b_{2g} states respectively. Lindholm, using semiempirical HAM/3 calculations has assigned peaks 1 and 3 to the two π^* states[L85]. This assignment is also suggested by the calculations of Giordan[GMT85].

4.2.2 Continuum Resonances in Benzene

In all previous studies[HBS84,SSH84,SGE83 and SSJ84] a given σ^* shape resonance was associated with one of the bonds, or types of bonds, in a molecule, and the energy of that shape resonance(relative to the I.P.) was correlated with the bond length. For aliphatic

Figure 4.1

4.1.1 The carbon K Shell ISEELS spectrum of gaseous benzene by energy loss of 2.8 KeV electrons at 1.0 eV FWHM resolution.

4.1.2 The carbon K Shell NEXAFS spectrum of solid(multilayer) benzene at 100K recorded at normal incidence.

4.1.3 The carbon K Shell NEXAFS spectrum of a monolayer of benzene at 200K recorded at normal incidence.

4.1.4 The carbon K Shell NEXAFS spectrum of a monolayer of benzene at 200K recorded at glancing incidence.

The dashed lines represent the estimated backgrounds.

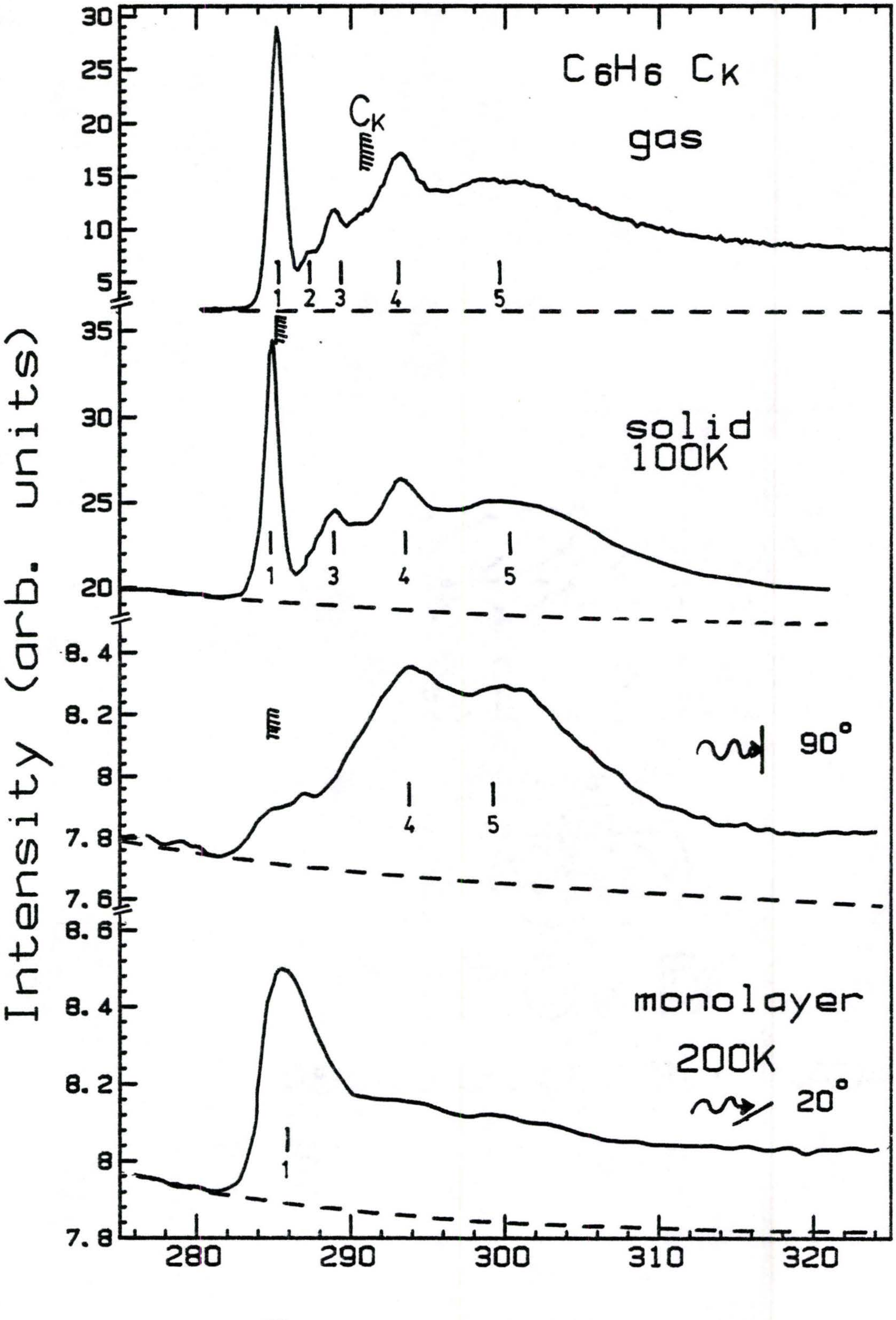
C6H6 CK
gas
CK
1
2
3
4
5
solid
100K
1
3
4
5
90°
4
5
monolayer
200K
20°
1
30
25
20
15
10
5
35
30
25
20
8.4
8.2
8
7.8
7.6
8.6
8.4
8.2
8
7.8
280
290
300
310
320
Intensity (arb. units)
Energy (eV)

hydrocarbons there is a σ shape resonance corresponding to each type of carbon-carbon bond in the molecule. This is the basis of the linear relationship between the σ shape resonance position, relative to the I.P., and the length of the corresponding bond[SSH84,SB84]. If this approach is extended to benzene, only one σ shape resonance should be expected for the one unique C-C bond length in benzene. However, benzene has two experimental and three calculated σ shape resonances. The difference between the aliphatic and aromatic cases can be understood by building up the correct delocalized σ^* states from a set of localized σ^* states[JS73], each of these being localized on one of the bonds in the molecule. In the case of the aliphatic molecules there is only a weak interaction between the localized σ^* states[JS73] and so the delocalized σ^* states corresponding to a given type of bond all lie at about the same energy, producing only one shape resonance. However, in benzene there is a strong interaction between the localized σ^* states, producing a set of delocalized σ^* states that are widely separated in energy. Previously only peak 5 was used in the correlation of bond length with shape resonance position. The present gas/solid/surface comparison indicates that peak 4 is not, as previously assigned[HB77], a double excitation feature, but is a σ shape resonance. The intensity weighted average energy of peaks 4 and 5, relative to the I.P., is 8.8 ± 0.5 eV. This is in good agreement with the predicted value[SSH84] of 8.5 ± 0.5 eV for a bond length of 1.40 Å with a single associated shape resonance(Z=12 correlation line).

4.2.3 Comparison to Solid and Monolayer NEXAFS Spectra

In order to resolve this controversy, the NEXAFS spectra for solid and chemisorbed benzene were obtained from Stöhr[S85]. The geometry of chemisorbed benzene has been determined to be parallel to the metal surface[JMS83,LID78,NM79,BR79]. The polarization dependence of the π^* and σ^* orbitals, as described by Stöhr and Jager[SJ82], should allow for identification of these orbitals in benzene and resolve the uncertainty in spectral assignments. The spectra of solid benzene is shown below that of gas phase benzene in Figure 4.1. The lower two curves of Figure 4.1 depict the spectra of benzene chemisorbed on a Pt(III) surface and recorded at perpendicular and grazing X-ray incidence respectively. In this figure an estimated background is shown as a dashed line for all four spectra. The background subtracted spectra are shown in Figure 4.2. Such a procedure is often necessary if relative intensities are to be accurately represented. The energies and assignments of all observed features in the benzene spectra are listed in Table 4.1.

In the benzene spectra the K shell ionization potential(I.P.) in each phase is indicated by the hatched line and labelled C_K. These values are taken from X-ray photoelectron measurements in the

Table 4.1

Absolute Energies (eV) and Assignments of Features in the Carbon K Shell Spectra of Benzene in the Gas, Solid and Monolayer States.

			Monolayer on Pt(III)		
Feature	Gas ± 0.1 eV	Solid ± 0.5 eV	90° ± 0.5 eV	20° ± 0.5 eV	Assignment[b]
1	285.2[a]	285.0	-	286.0	π^* (e_{2u})
2	287.2	-	-	-	3p
3	288.9	288.9	-	-	π^* (b_{2g})
4	293.5	293.3	293.7	-	σ^* (e_{1u})
5	300.2	300.1	299.9	-	σ^* ($e_{2g} + a_{2g}$)
I.P.	290.3[c]	284.9[d]	284.4[e]	284.4[e]	

[a] ISEELS spectrum recorded with 1.0 eV FWHM. Feature 1 was determined to be 2.2(1) eV lower in energy that the C 1s → π^* transition in CO (287.40 eV)[SB84].

[b] Only the final orbital is listed.

[c] From gas phase XPS, relative to vacuum level[DS74].

[d] From solid state XPS, relative to Fermi level[CK71].

[e] R. J. Koestner (private communication), relative to Fermi level[K85].

gas phase[DS74], solid state[CK71] and chemisorbed states[K85]. In the gas phase spectrum, the I.P. corresponds to the 1s binding energy(BE) relative to the vacuum level(E_v) while for the solid and chemisorbed cases it corresponds to the 1s BE relative to the Fermi level(E_F). For the gas phase spectrum resonances 1 and 3 fall below the I.P. and are therefore bound state transitions. For the neutral molecule the antibonding states into which the 1s electron is excited fall above E_v, but in inner shell excitation they are pulled below E_v by the Coulomb interaction with the 1s core hole. For solid benzene, which is an insulator, the Fermi level falls in the band gap and the resonance energies for the transitions can be either smaller or larger than the 1s BE's. For a chemisorbed molecular monolayer on a metal surface the lowest possible 1s excitation energy is determined by the 1s BE relative to E_F since by definition all states below E_F are filled. Therefore the $1s \rightarrow \pi^*$ transition energy must be slightly larger than the 1s BE. This is in agreement with all previously studied cases.

The NEXAFS spectrum of solid benzene shows the same major resonances as the gas phase spectrum. This indicates that all resonances are highly localized on the benzene molecule. Feature 2 is greatly reduced in intensity in the spectrum of solid benzene. This is indicative of a Rydberg orbital, which collapses upon condensation[R75], and supports the previous assignments of this feature. The term value of 3.1 eV indicates that feature 2 in the

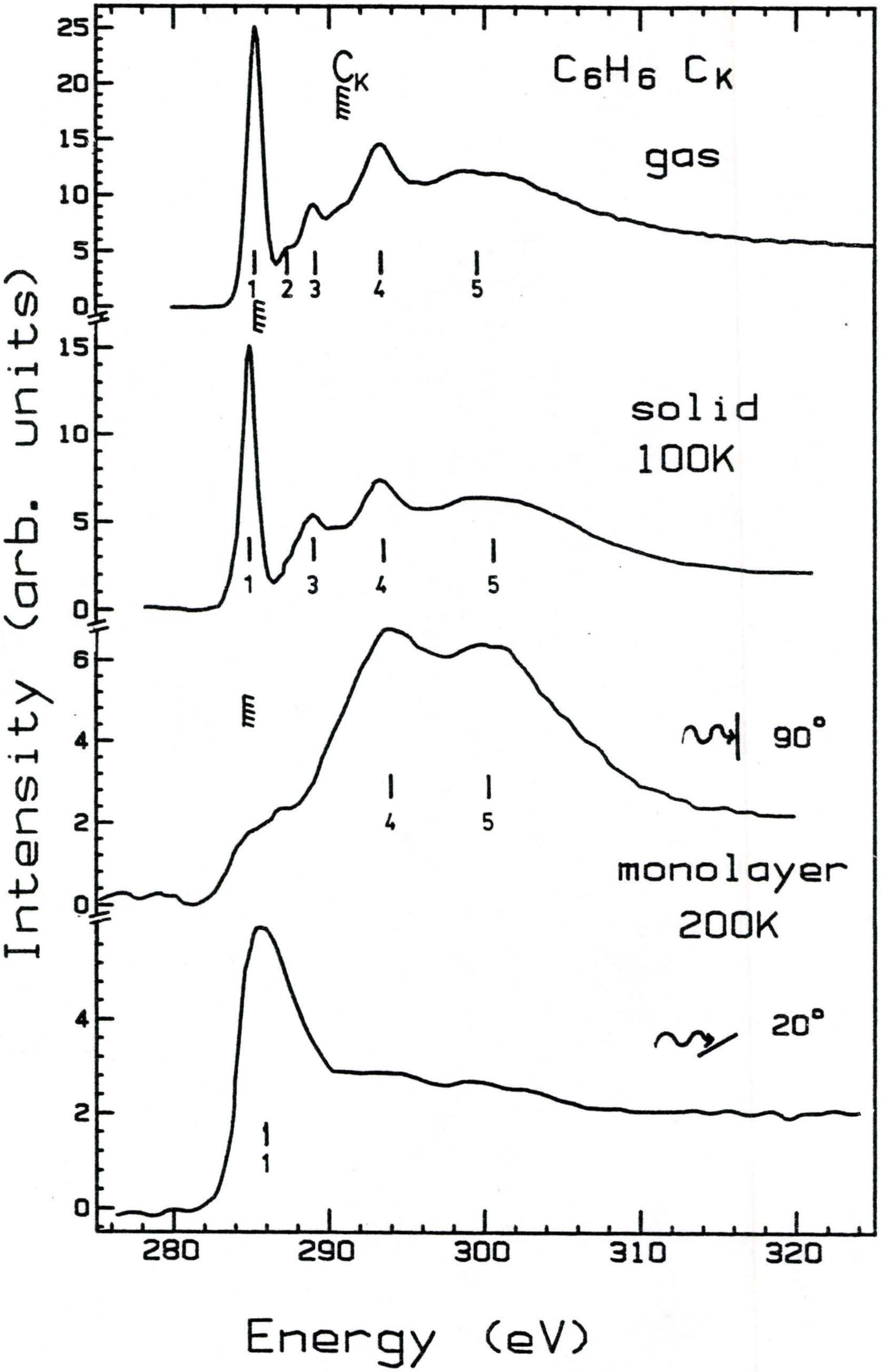

Figure 4.2 The carbon K Shell Spectra of gas phase, solid and monolayer benzene with a background subtracted.

gas phase spectrum can be assigned to transitions to a 3p Rydberg orbital[R75]. Feature 3, on the other hand, is not quenched in the spectrum of the solid. This is strongly supportive of a transition to a valence type antibonding orbital and not to the Rydberg orbital as previously assigned[HB77].

The symmetry of the final orbital in the transition corresponding to feature 3 can then be determined by the polarization dependence in the chemisorbed phase. The NEXAFS spectra of chemisorbed benzene has been recorded at perpendicular and glancing X-ray incidence[HSH85]. Features 1 and 3 have opposite polarization dependence from features 4 and 5 indicating that they are of opposite symmetry. Linearily polarized X-rays can induce transition to pure σ^* or π^* states in chemisorbed species depending on the molecular orientation and angle of X-ray incidence[SJ82]. The benzene is chemisorbed parallel to the surface and thus the polarization dependence indicates that features 1 and 3 are of π symmetry while features 4 and 5 are of σ symmetry. In the grazing incidence spectrum of chemisorbed benzene feature 3 is not resolved due to broadening of the π^* features. This increased width can be shown by comparing the chemisorbed benezene to that of pyridine(see Table 4.4) Pyridine which chemisorbs perpendicular to the surface does not show the same degree of broadening as benzene does. The polarization dependence of the high energy wing of the broadened first peak indicates that peak 3 should be assigned to the higher energy b_{2g} (π^*) state.

Figure 4.3

A comparison of the carbon K Shell ISEELS spectrum of gaseous benzene with the spectrum generated by an $X\alpha$ multiple scattering calculation[HSH85]. The calculated resonances are indicated on this spectrum.

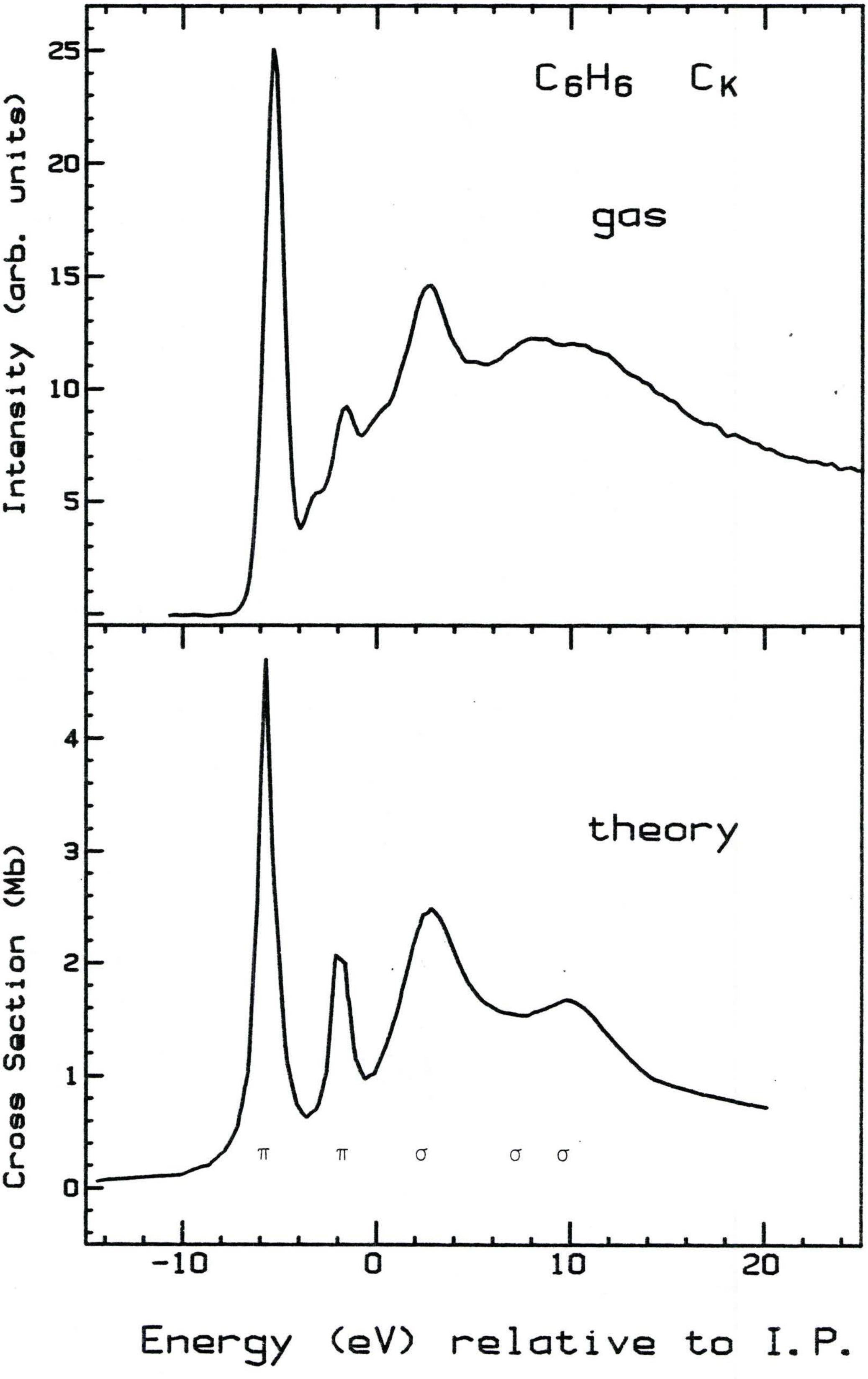
C_6H_6 C_K
gas
Intensity (arb. units)
25
20
15
10
5
theory
Cross Section (Mb)
4
3
2
1
0
π
π
σ
σ
σ
-10
0
10
20
Energy (eV) relative to I.P.

In the spectrum of chemisorbed benzene at perpendicular X-ray incidence neither features 1 or 3 are significantly intense. Features 4 and 5 are the major resonances in this spectrum. This indicates that they are both of σ symmetry. To try to obtain a better understanding of the benzene carbon 1s spectrum a Xα multiple scattering calculation was performed by Horsley(Exxon)[HSH85]. The results of this calculation, shown in Figure 4.3, matches the gas phase spectrum of benzene quite well, although there are three σ^* states in the calculated spectrum. The first two calculated resonances are π^* resonances due to transitions from the 1s to e_{2u} and b_{2g} levels respectively. The remaining three resonances are the e_{1u}, e_{2g} and a_{2g} σ^* states. The matching of the first two calculated resonances to peaks 1 and 3 in the gas phase is additional evidence that these peaks are the two π^* states. The fourth feature corresponds to the e_{1u} state, based on SCF-MO calculations[HSH85] and the fifth feature corresponds to transitions to the two closely spaced e_{2g} and a_{2g} σ^* states.

4.3 Pyridine

4.3.1 Pyridine Carbon K-Shell ISEELS Spectrum

The carbon K shell electron energy loss spectrum of pyridine is shown at the top of Figure 4.4. The spectrum is once again dominated by four resonances and is quite similar in appearance to that of benzene. This is not entirely unexpected, as the isoelectronic nature and similar geometry of pyridine should lead to a similar electronic structure to that of benzene. A major effect of placing the nitrogen in the benzene ring is to reduce the symmetry of the system from D_{6h} to C_{2v}. This has the effect of splitting the degenerate e_{2u} π^* state into two π^* states, b_1 and a_2. Thus the C_K spectrum should show three π^* states if there is sufficient resolution.

The first feature seen in the C_K spectrum of pyridine, which was the degenerate e_{2u} level in benzene, does not appear to be split. Electron transmission spectroscopy of pyridine by Nenner and Schulz[NS74] indicates that the separation between the a_2 and b_1 levels is 0.6 eV which is less than the instrumental resolution of 1.0 eV initially available. Theoretical MO calculations have indicated that the splitting is much less than the 0.6 eV shown by Nenner and Schulz[JS76]. Improved resolutions of 0.7 - 0.6 eV which became available later(see Chapter 2) still showed no splitting or

Figure 4.4

4.4.1 The carbon K Shell ISEELS spectrum of gaseous pyridine by energy loss of 2.8 KeV electrons at 1.0 eV FWHM resolution.

4.4.2 The carbon K Shell NEXAFS spectrum of solid(multilayer) pyridine at 100K recorded at normal incidence.

4.4.3 The carbon K Shell NEXAFS spectrum of a monolayer of pyridine at 300K recorded at normal incidence.

4.4.4 The carbon K Shell NEXAFS spectrum of a monolayer of pyridine at 300K recorded at glancing incidence.

A background has been subtracted from all the spectra.

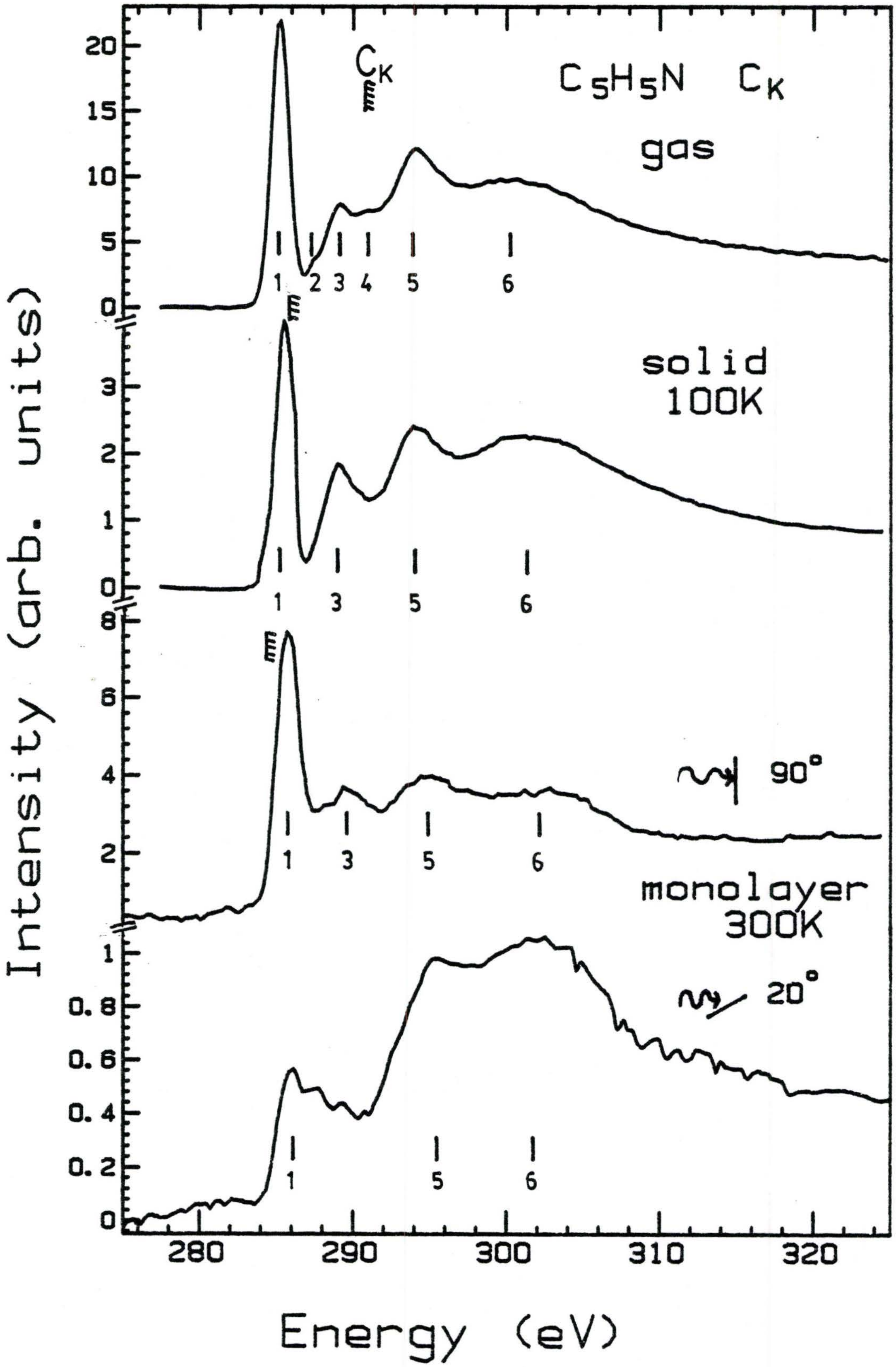
C5H5N Ck
Ck
gas
solid
100K
monolayer
300K
90°
20°
1
2
3
4
5
6
0
5
10
15
20
1
2
3
8
6
4
0.2
0.4
0.6
0.8
280
290
300
310
320
Intensity (arb. units)
Energy (eV)

Table 4.2

Absolute Energies (eV) and Assignments of Features in the Carbon K Shell Spectra of Pyridine in the Gas, Solid and Monolayer States.

Feature	Gas	Solid	Monolayer on Pt(III)		Assignment
			90°	20°	
	± 0.1 eV	± 0.5 eV	± 0.5 eV	± 0.5 eV	
1	285.3[a]	285.5	285.8	285.9	π^*
2	287.4	-	-	-	3p Rydberg
3	289.2	289.1	289.6	-	π^*
4	290.8	-	-	-	continuum onset
5	294.2	294.1	294.7	295.3	σ^*
6	300.1	301.0	302.0	301.7	σ^*
I.P.	290.6[b]	285.9[c]	284.4[d]	284.4	

[a] This feature was found to occur at 2.1(1) eV lower in energy than the C 1s → π^* transition in CO (287.40 eV)[SB84].

[b] Obtained from the solid state average carbon 1s I.P. (285.9 eV) [CCK72] and the differences in gas[BCJ80] and solid state[CCK72] nitrogen 1s I.P.'s for pyridine (4.7 eV).

[c] Average of the 3 carbon 1s environments[CCK72].

[d] Value for benzene on Pt(111).

Figure 4.5

4.5.1 The carbon K Shell ISEELS spectrum of gaseous pyridine by energy loss of 2.8 KeV electrons at 0.6 eV FWHM resolution.

4.5.2 The nitrogen K Shell ISEELS spectrum of gaseous pyridine by energy loss of 2.9 KeV electrons at 0.6 eV FWHM resolution.

A background has been subtracted from both spectra.

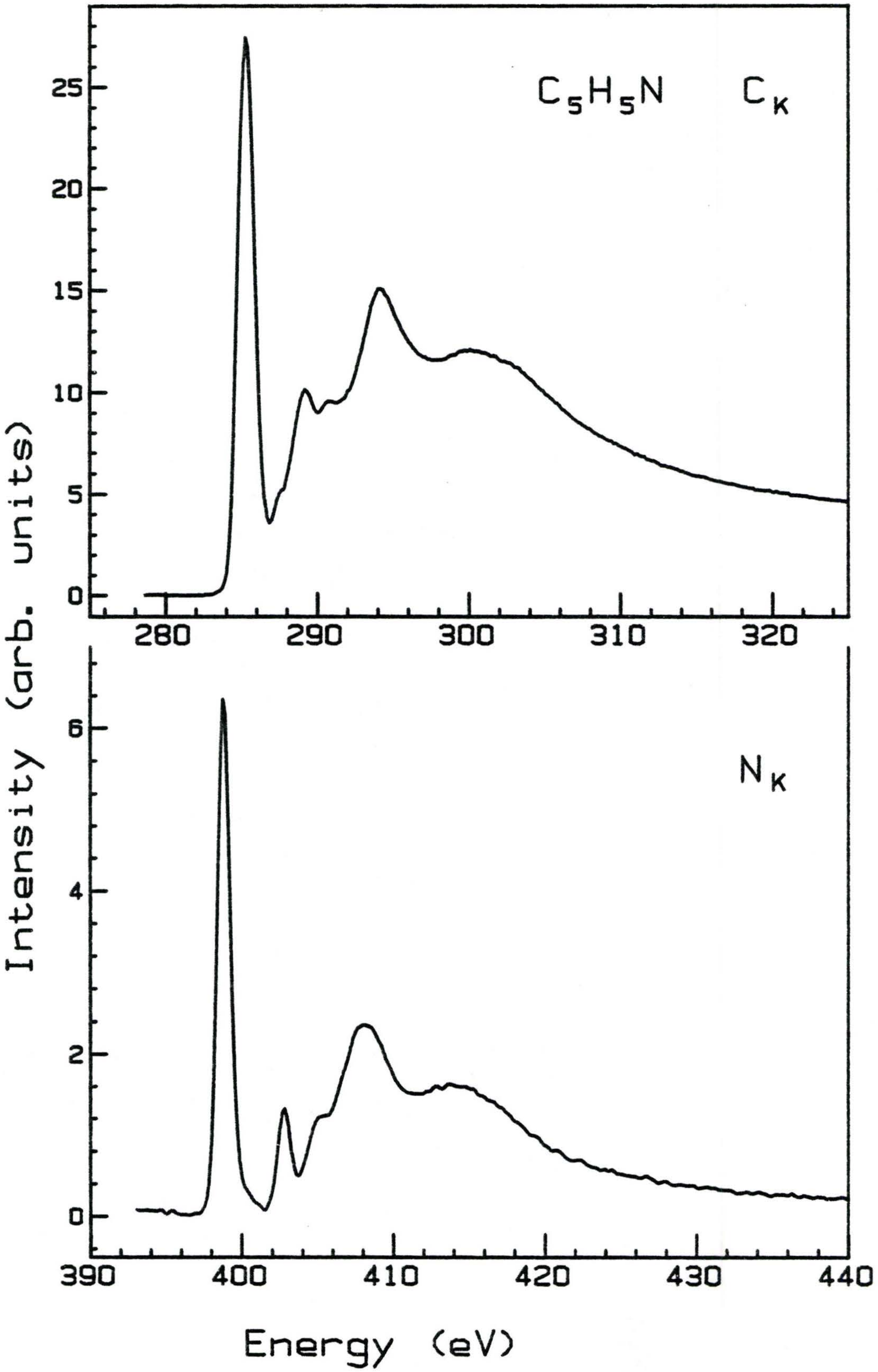
C_5H_5N C_K
N_K
Intensity (arb. units)
Energy (eV)
0
5
10
15
20
25
280
290
300
310
320
0
2
4
6
390
400
410
420
430
440

asymmetry(see Figure 4.5). The improvement in resolution decreased the peak width only 0.2 eV in the C_K shell spectrum, indicating that the peak width is molecule rather than instrument determimed. The combination of 2 electronic and vibrational broadening, which has accounted for the asymmetry in the e_{2u} level in benzene[HB77], may also explain why this feature appears as a single, symmetric peak. The second and fourth features in pyridine appear to be Rydberg due to their low intensities. The second feature is assigned to the 3p Rydberg state based on its term value of 3.2 eV. The fourth feature is assigned to the onset of the continuum. Peak 3 appears to be analogous to the second π^* feature in benzene. In C_{2v} symmetry this orbital, which has b_{2g} symmetry in benzene, now has b_1 symmetry. The two remaining resonances are assigned to transitions to σ^* levels as described in benzene. It might be expected that, in the simple approach used for aliphatic molecules[SSH84], the different C-C bond lengths and the C-N bond will give different σ shape resonance positions. The two C-C bonds are only 0.002Å different(1.394 and 1.392Å [LB76]) and could not be distinguished. The C-N is 0.05Å shorter than the C-C bonds(1.338 Å [LB76]) and this separation should be noticable. Using the correlation lines developed in [SSH84], the C-C bond length corresponds to a σ shape resonance position of 8.9(5) eV while the C-N bond length corresponds to a σ shape resonance position of 3.9(5) eV above the edge. The effects of the aromaticity as observed in benzene(Section 4.2.2) is expected to dominate and thus resonance due to single bond lengths as separate features are not seen but rather are combined in delocalized σ^* states which produce two continuum features experimentally. The intensity weighted average of the two σ shape resonance positions in the carbon K shell spectrum of pyridine have a value of 8.7(5) eV. Thus the predicted value is in excellent agreement with experiment using this modified approach of Sette el al[SSH84].

4.3.2 Comparison to Solid and Chemisorbed NEXAFS Spectra

The solid, normal and glancing incidence chemisorbed carbon K shell NEXAFS spectra of pyridine are shown below the gas phase spectrum in Figure 4.4. As with benzene, all the spectra have had a background subtracted from them. The I.Ps, again indicated by a hatched line and labelled C_K, were determined in the same manner as were the benzene I.P.s. The values of the I.P.s and energies of the observed transitions are listed in Table 4.2.

As with benzene, the spectrum of solid pyridine once again shows the same major resonances as the gas phase spectrum indicating all the observed transitions are intramolecular. The polarization dependence of peaks 1 and 3 are opposite from peaks 5 and 6 indicating that they are of opposite symmetry. The 1s → π^* peaks in pyridine have opposite polarization dependence to that of benzene. This has been used to determine that pyridine is oriented perpendicular to the surface[JMS84,JMS85]. Peaks 2 and 4 from the gas phase spectra are quenched in the condensed phase spectra confirming their assignment to Rydberg orbitals. The polarization dependence of peaks 1 and 3 confirm their assignment to the π^* levels. Again no splitting of peak 1 can be seen even with improved instrument resolution. The polarization dependence of peaks 5 and 6 confirm their assignment to σ shape resonances.

4.3.3 Pyridine Nitrogen K-Shell ISEELS Spectrum

The nitrogen K shell electron energy loss spectrum of gaseous pyridine is shown in Figure 4.6. This spectrum resembles that of the carbon K shell spectrum indicating that the transitions occur to the same set of unoccupied molecular orbitals. Symmetry considerations indicate that only two $1s \rightarrow \pi^*$ transitions are dipole allowed and the first peak should by narrower than the first peak in the carbon K shell spectrum. The first $1s \rightarrow \pi^*$ peak should only be to the $3b_1$ level, due to dipole selection rules. The width here, 1.4 eV at best available resolution(see Table 4.4), indicates that vibrational excitation accompanies the core excitation. A difference in the widths of analogous features in different core edge spectra of the same molecule has also been observed in CO[HB80]. In this high resolution study it was not possible to see any vibrational structure in the O_{1s} spectrum. This was attributed to either dissociation of

Figure 4.6

4.6.1 The nitrogen K Shell ISEELS spectrum of gaseous pyridine by energy loss of 2.9 KeV electrons at 1.0 eV FWHM resolution.

4.6.2 The nitrogen K Shell NEXAFS spectrum of solid(multilayer) pyridine at 100K recorded at normal incidence.

4.6.3 The nitrogen K Shell NEXAFS spectrum of a monolayer of pyridine at 300K recorded at normal incidence.

A background has been subtracted from each spectrum.

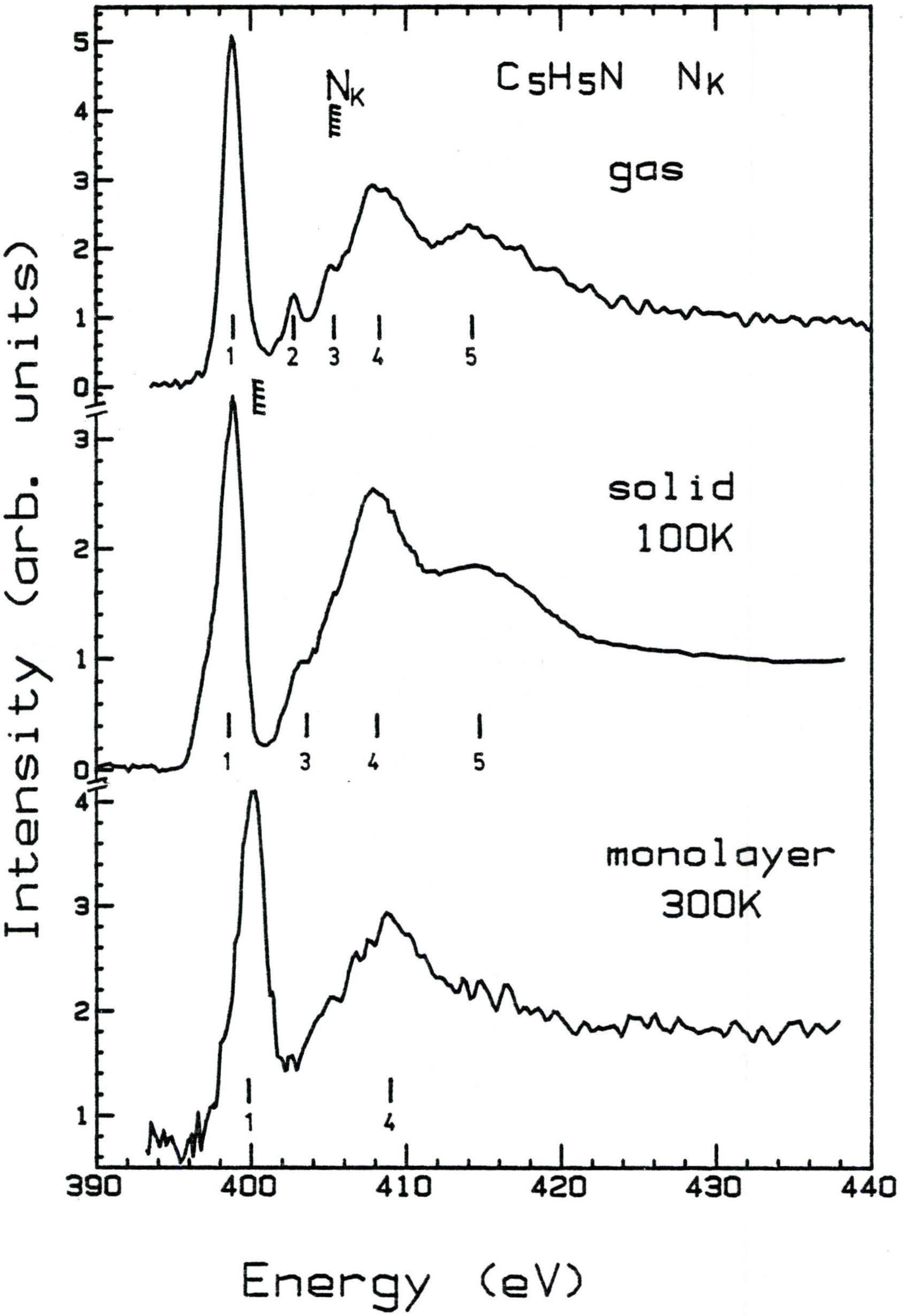
C5H5N NK
NK
gas
solid
100K
monolayer
300K
1
2
3
4
5
Intensity (arb. units)
Energy (eV)
390
400
410
420
430
440
0
1
2
3
4
5

the (O_{1s}^{-1}, π^*) excited state or a rapid Auger decay giving rise to a larger line width[HB77]. Such reasoning may also explain the different widths in the first feature of the nitrogen K shell spectrum.

Feature 2 is assigned to the second 1s → π^* transition. This transition is to a level of $4b_1$ symmetry since the $3b_1$ is placed at lower energy[NS75,C67,JS76] and the $2a_2$ is dipole forbidden. The small feature 3 is a result of the onset of the continuum. Peak 4 and 5 are assigned to σ shape resonances. In the nitrogen K shell spectrum, only one σ shape resonance should be seen, corresponding to the one C-N bond. This should have a value of 5.2(5) eV according to Sette[SSH84]. However, the delocalization of the σ^* states in aromatic molecules accounts for the splitting of the σ^* levels. The intensity weighted average of the two experimental position gives a value of 6.0(5) eV and thus the predicted value of 5.2(5) eV is in good agreement. It is interesting to note that the intensity of the first σ shape resonance is larger that that of the second σ shape resonance in pyridine. This may be an indication of a departure from the pure aromatic picture seen in benzene. More discussion of this is given in Chapter 7.

4.3.4 Comparison to Condensed Phase NEXAFS Spectra

The NEXAFS spectra of solid and monolayer pyridine, recorded at normal incidence, obtained by Stöhr[HSH85] and are shown below the gas phase spectrum in Figure 4.6. The grazing incidence spectrum of chemisorbed pyridine were not recorded by Stöhr and co-workers. Comparison of the gas and solid spectra indicates that all of the solid state features are intramolecular. The same four major resonances are again present although feature 2 is broadened and overlaps with peak 4. The relative intensities have changed from the gas phase to the condensed phase. This may be due to partial orientation in the solid state. The energies of all observed features in Figure 4.6 are listed in Table 4.3. The low energy shoulder on the first peak of the solid and monolayer spectra is thought to be an instrumental artifact from a nonguassian monochromator response function[S85]. The presence of some σ shape resonance intensity in the normal incidence C_K and N_K NEXAFS spectrum of pyridine indicates that the ring is not 90°. to the surface but is tilted away from the surface normal. This has been interpreted as cleavage of the alpha C-H bond which converts the pyridine to the alpha pyridyl state at temperatures above 240K[JMS85].

Table 4.3

Absolute Energies (eV) and Assignments of Features in the Nitrogen K Shell Spectra of Pyridine in the Gas, Solid and Monolayer States

			Monolayer on Pt(III)	
Feature	Gas ± 0.1 eV	Solid ± 0.5 eV	90° ± 0.5 eV	Assignment
1	398.8[a]	398.8[b]	400.1[c]	π^*
2	402.7	403.3	-	π^*
3	405.1	-	-	Continuum onset
4	408.0	408.0	408.2	σ^*
5	414.3	414.3	-	σ^*
I.P.	404.9[d]	400.2[e]		

a. This feature was found to occur at $2.3^{(1)}$ eV lower energy than the $N_{1s} \to \pi^*$ feature in N_2(401.1 eV)[SB84].

b. The original spectrum was shifted 1.4 eV to lower energy in order to align the first π^* peak with that of the gas phase spectrum.

c. The recorded spectrum was shifted 1.4 eV to lower energy. The shift of 1.3 eV between solid and monolayer $N_{1s} \to \pi^*$ is considered real.

d. From gas phase XPS[BCJ80].

e. From solid state XPS[CCK72].

4.4 Broadening of π Features

A comparison of the gas or solid spectra of benzene to the chemisorbed spectrum shows considerable broadening of the 1s → π^* features. This broadening can also be seen in both the C_K and N_K spectra of pyridine although the broadening is not as pronounced(see Table 4.4). This broadening is interpreted as the effect of the interaction of the molecular π system and the metal surface. The hybridization of molecular π^* orbitals with metal orbitals of predominantly d character leads to a broadening of the π^* resonances. The broadening is much greater in benzene since it lies parallel to the surface while the plane of the pyridine ring is perpendicular to the surface. The origin of the broadening is thought to be an energy broadening of the hybridized π^* states relative to the pure molecular π^* state(initial state effect) and/or a reduced lifetime in the 1s → π^* final state created in the excitation process. Such a reduction in the excited states lifetime would result from the overlap of metal and molecular states as a consequence of delocalization. A similar broadening effect has been observed in the carbon and oxygen 1s → π^* transitions of monolayer CO on Ni(III)[JHA84]. The shift of +1.3 eV in the position of the 1s → π^* peak in the N_K edge in monolayer pyridine, relative to the gas or solid state position, is also attributed to interaction between the N $2p\pi$ orbital of pyridine with adjacent metal d orbitals.

Table 4.4

Molecule	Edge	Feature	State	$\pi^{*(a)}$ FWHM(eV)
C_6H_6	C_K	1	gas	1.2
		1	solid	1.1
		1	monolayer(20°)	5.8
		1	monolayer(90°)	-
C_5H_5N	C_K	1	gas	1.1
		1	solid	1.5
		1	monolayer(20°)	-
		1	monolayer(90°)	2.0
	N_K	1	gas	1.4
		1	solid	1.9
		1	monolayer(90°)	2.8
	C_K	1	gas$^{(b)}$	1.3
	N_K	1	gas$^{(b)}$	1.6

a. 1s → π^* transition has e_{2u} symmetry in benzene, b_1 and a_2 symmetry in C_K of pyridine and b_1 symmetry in N_K of pyridine.

b. FWHM of features in spectra of pyridine using old spectrometer (see Chapter 2).

4.5 Conclusions

With the help of K shell spectra for gas phase, solid state and chemisorbed benzene and pyridine and a multiple scattering X_α calculation of the benzene K shell cross section, all the principle features have been assigned in the spectra. The carbon and nitrogen K shell spectra of gas phase pyridine are reported for the first time. The combination of the benzene spectra and the MSX_α calculation has lead to a reassignment of the benzene spectrum which had been previously recorded[HB77]. The assignment of two σ shape resonances for aromatic molecules has allowed the empirical relationship between bond length and σ resonance position to be applied to aromatic molecules as well as simple hydrocarbons. The spectra also indicated that there is little distortion in these molecules when going from the gas phase to the solid or chemisorbed state.

CHAPTER 5

CARBON K-SHELL SPECTRA OF SOME NON-AROMATIC, CYCLIC HYDROCARBONS

5.1 Introduction

In the previous chapter, the gas, solid and monolayer spectra of benzene and pyridine were found to be dominated by a common set of intramolecular resonances. The similarity of the various spectra indicated that the aromatic molecules had similar electronic excitations which resulted in bound π^* states and delocalized continuum σ^* states. The correlation with bond length produced reasonable agreement with theory only after the intensities of both of the continuum states had been taken into account. In order to determine whether this was a function of the aromatic nature of benzene and pyridine or due, in part, to their cyclic nature, an investigation of some saturated and unsaturated cyclic hydrocarbons has been carried out. Solid and chemisorbed NEXAFS spectra were provided for C_5H_8, C_6H_{12} and C_8H_8 from Stöhr and coworkers[S85], while gas phase ISEELS spectra of C_5H_8, C_5H_{10}, C_6H_{10} , C_6H_{12} and C_8H_8 were recorded. In this chapter, the results are presented and interpreted. In addition, the ability of the empirical bond length versus σ shape resonance position relationship [SSH84] to predict the experimental results in these molecules will be tested.

5.2 Results and Discussion

5.2.1 Saturated Cyclic Hydrocarbons

The carbon K-shell gas phase spectra of C_5H_{10} (cyclopentane) and C_6H_{12} (cyclohexane) are shown in Figure 5.1. The energies and tentative assignments are listed in Table 5.1. To our knowledge, the carbon 1s ionization potential(I.P.) of gaseous C_5H_{10} has not been reported. However, it is unlikely to vary significantly from that of cylcohexane (290.3 eV [BCJ80]) since hydrocarbon C 1s I.P.s are all within 0.8 eV of 290.3 eV, independent of chain length or even hybridization[SSH84,PSB76]. An indication of this are the carbon 1s I.P.s of the linear chains C_5H_{12} and C_6H_{14} which are 290.42 eV and 290.36[PSB76] respectively. The uncertainty in the estimate of the C 1s I.P. of C_5H_{10} is likely to be less than 0.5 eV.

The two spectra in Figure 5.1 have roughly the same appearance each consisting of three main resonances. The C_6H_{12} spectrum has a small shoulder, feature 2, on the major resonance, feature 3. Feature 3 is located further above the K-shell I.P. in C_6H_{12} than the corresponding resonance in C_5H_{10}. The resonances are expected to resemble those found in ethane and to some extent this is true[HB77]. The most intense feature in ethane has been assigned to a 1s → 3p Rydberg transition with a term value of 2.7 eV[HB77]. In both C_5H_{10} and C_6H_{12} feature 1 also has a term value of 2.7 eV which

Figure 5.1

5.1.1 The carbon K-shell ISEELS spectrum of gaseous cyclopentane recorded by electron energy loss of 2.8 keV electrons at 1.0 FWHM resolution.

5.1.2 The carbon K-shell ISEELS spectrum of gaseous cyclohexane recorded by electron energy loss of 2.8 keV electrons at 1.0 FWHM resolution.

A background has been subtracted from each spectrum.

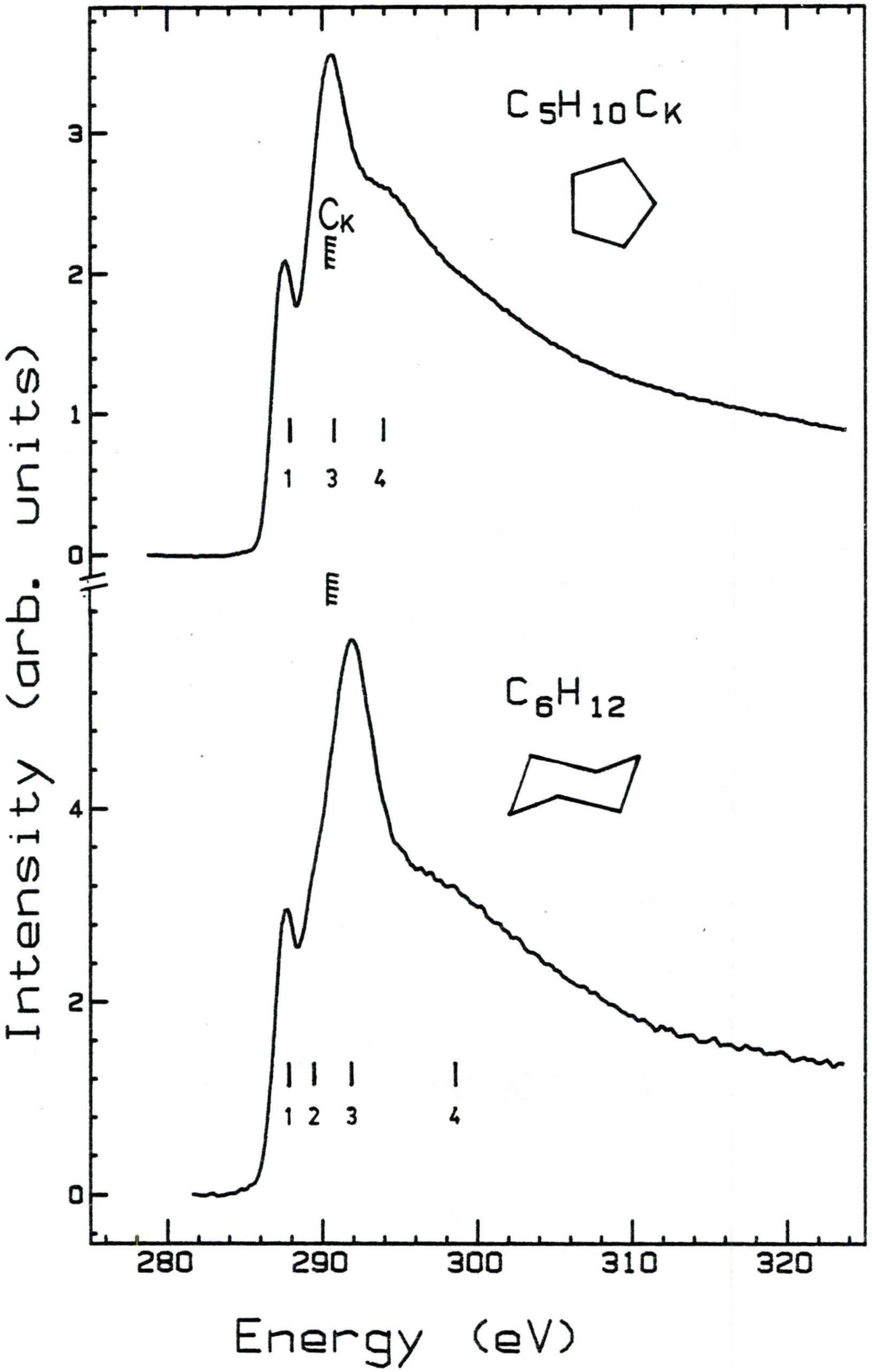
$C_5H_{10}C_K$
C_K
C_6H_{12}
1
3
4
1
2
3
4
0
1
2
3
0
2
4
280
290
300
310
320
Intensity (arb. units)
Energy (eV)

is consistent with an assignment to the 3p Rydberg state[R74]. However an alternate assignment is preferred as explained in Section 5.2.2. The shoulder(2) in the C_6H_{12} spectrum is likely a poorly resolved 4p Rydberg transition.

The most intense feature in both spectra occurs around 291 eV, just above the I.P.. It is assigned to a 1s → σ^*(C-C) transition whose position can be related to the C-C single bond length in these molecules[SSH84,HBS84]. The C-C single bond length of C_5H_{10} (1.5460Å) is approximately 0.01Å longer than that of C_6H_{12} (1.5351Å)[LB76]. The correlation relationship reported previously[SSH84] predicts that the σ(C-C) resonance of C_6H_{12} should occur 0.5 eV higher in energy above the I.P. than in C_5H_{10}. Experimentally, the feature we assign to the σ(C-C) resonance is 1.3 eV higher in C_6H_{12} than in C_5H_{10}. Thus the observed shift is in good agreement with the correlation relationship[SSH84] in both direction and magnitude.

A very broad, low intensity shoulder is observed in the spectra of both C_5H_{10} and C_6H_{12} on the high energy side of feature 3. This shoulder is much more intense in C_5H_{10}. than in C_6H_{12}. This feature is thought to be a second σ^* shape resonance. The rationale for this assignment is presented in the condensed phase section(5.2.2) and further in Chapter 7.

Table 5.1

Absolute Energies(eV) and Tentative Assignments of Features Observed in the Carbon K-Shell Spectra of Gaseous Cyclopentane and Cyclohexane

Feature	Energy (± 0.1 eV)		Assignment[b]
	C_5H_{10}	C_6H_{12}	
1	287.6[a]	287.7[a]	$\pi^*(CH_2)$
2	-	289.2	4p
3	290.5	291.9	σ^*(C-C)
4	294.5	299.6	σ^*(in-ring)
I.P.	290.3[c]	290.3[d]	

a. The first feature in C_5H_{10} is 2.8(1) eV above the 1s → π^* transition in C_2H_4(284.7 eV).
The first feature in C_6H_{12} is 1.8(1) eV above the 1s → π^* transition in C_2H_2(285.9 eV)[HB77].

b. Only the final orbital is listed.

c. Estimated from the I.P.s of similar hydrocarbons[BCJ80].

d. From X-ray PES[BCJ80].

5.2.2 Comparison to Condensed Phase NEXAFS Spectra

The NEXAFS spectra of solid phase(multilayer) and monolayer C_6D_{12} on Pt(III) recorded at both grazing(20°) and normal(90°) X-ray incidence are shown in Figure 5.2 along with the gas phase spectrum for comparison. As previously observed in benzene and pyridine(Chapter 4), the gas phase, multilayer and monolayer of cyclohexane show similar major spectral features, indicating that transitions to a common set of intramolecular states dominate the spectra in all phases. Aside from intensity variations associated with polarization dependence, two features are particularly noteworthy in comparing the condensed phase to the gas phase ISEELS spectra. These are peak 1 and the peak (a), a feature at 284 eV which is not observed in the gas phase spectra. The energies of the observed features and their assignments are listed in Table 5.2.

The fact that peak (a) is observed in the monolayer and multilayer spectra but not in the gas phase spectrum strongly suggests that it arises from intermolecular or molecule-surface interactions. In the monolayer, peak (a) probably arises from promotion of carbon 1s electrons into the unoccupied valence band of the metal substrate. This interpretation is supported by the observation that the onset of (a) is coincident with the measured C 1s I.P.[K85], corresponding to the Fermi level of C_6D_{12} covered metal.

Figure 5.2

5.2.1 The carbon K-shell ISEELS spectrum of gaseous cyclohexane.

5.2.2 The carbon K-shell NEXAFS spectrum of solid cyclohexane recorded with normal X-ray incidence by partial electron yield from a multilayer condensed on Pt(III) at 100K.

5.2.3 The carbon K-shell NEXAFS spectrum of solid cyclohexane at glancing incidence.

5.2.4 The carbon K-shell NEXAFS spectrum of a monolayer of deuterated cyclohexane on Pt(III) at room temperature as recorded at normal incidence.

5.2.5 The carbon K-shell NEXAFS spectrum of a monolayer of deuterated cyclohexane on Pt(III) at room temperature as recorded at grazing incidence.

A background has been subtracted from each spectrum.

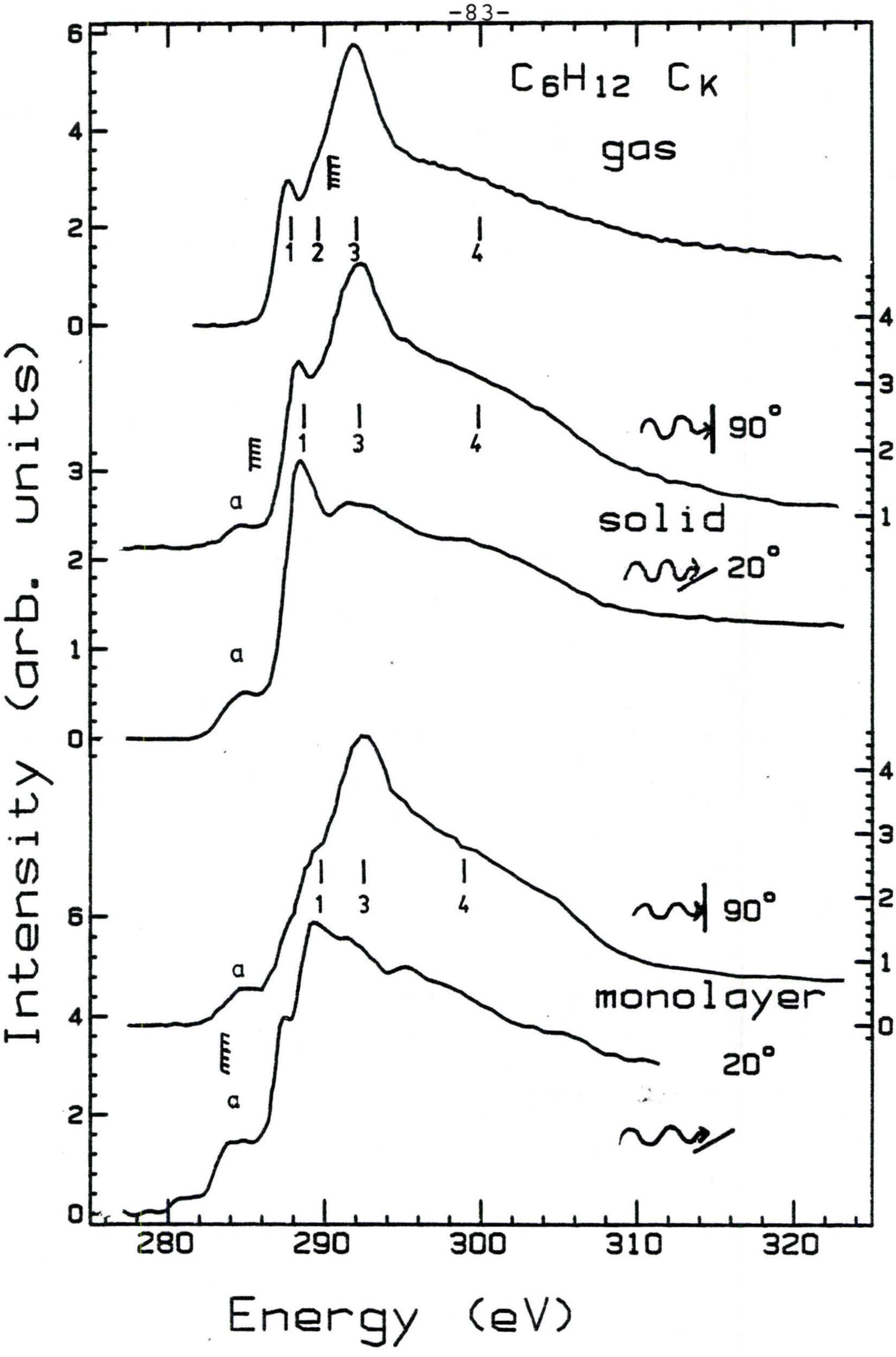
C_6H_{12} C_K
gas
solid
monolayer
90°
20°
90°
20°
a
a
a
a
1
2
3
4
1
3
4
1
3
4
Intensity (arb. units)
Energy (eV)
280
290
300
310
320
0
2
4
6
0
1
2
3
0
2
4
6
0
1
2
3
4
0
1
2
3
4

In the multilayer, which may be a thin one(<10 layers), feature (a) is weaker relative to the higher energy features than in the monolayer. In the multilayer spectrum feature (a) may arise from transitions from the C_6D_{12} layer closest to the metal. This signal, detected in a partial electron yield mode, would in a sense be "shining" through the overlying C_6D_{12} layers.

Peak 1 is also of interest. In our discussion of the gas phase spectrum, this feature was suggested to be a transition to the 3p Rydberg state. However, a Rydberg assignment is inconsistent with the prominent intensity of this feature in the multi and monolayer spectra(Figure 5.2) since transitions to Rydberg orbitals generally disappear in condensed spectra. Indeed, this behaviour is used frequently to distinguish molecular from Rydberg transitions[R75]. Feature 1 does not disappear in the multilayer spectrum. Furthermore, it shows polarization dependence which would not be expected for a spherically symmetric Rydberg orbital. Clearly some explanation other than a Rydberg transition is required.

The obvious alternative is to assign feature 1 to a valence state based on transitions to a molecular orbital of antibonding character. This would be more consistent with the strong intensity observed in the solid state. Cyclohexane in the chair conformation has a low lying antibonding $4a_{1u}(\sigma^*CH_2)$ orbital[JS73] and transitions to this level are dipole allowed. Furthermore, peak 1 shows a polarization dependence which is opposite of that of the σ(C-C) shape resonance[SJ82]. Thus both the polarization dependence and the absence of quenching in the solid state are consistent with a transition to a $4a_{1u}(\pi^*CH_2)$ orbital. Cyclopentane also has a low lying 14a' $\pi^*(CH_2)$ orbital[JS76] suggesting this assignment for peak 1 in the C_5H_{10} C_K spectrum.

A reassignment of other hydrocarbon spectra may be in order in light of the assignment of feature 1 in the C_5H_{10} and C_6H_{12} spectra to a $1s \rightarrow \pi^*$ (CH_2) level. For example, molecular orbital diagrams for ethane show that an analogous $\pi^*(CH_3)$ orbital exists in both the staggered($2e_u$ symmetry) and eclipsed(2e' symmetry) conformations of ethane[JS76]. This suggests that the first feature in ethane(287.9 eV[HB77]) corresponds to a $1s \rightarrow \pi^*$ (CH_3) transition rather than the 3p Rydberg level to which it was previously assigned.

Surprisingly, the solid state spectrum of C_6H_{12} shows considerable polarization dependence. This suggests that the molecules in the multilayer solid are at least partially oriented. The degree of orientation in a sample can be expressed by an orientation factor defined as the ratio of the intensity of a feature in spectra recorded with different angles of X-ray incidence of the sample. Since we have not measured absolute intensities, the intensity ratios were normalized by taking the ratio of the ratio of peak 3 to peak 1 in the C_6D_{12} spectra in each of the two different

Table 5.2

Absolute Energies(eV) and Tentative Assignments of Features Observed in the Carbon K-Shell Spectra of Gas Phase, Multilayer and Monolayer C_6H_{12} on Pt(III)

Feature	Gas	Multilayer		Monolayer		Assignment[a]
		90°	20°	90°	20°	
	±0.1 eV	±0.5 eV	±0.5 eV	±0.5 eV	±0.5 eV	
1	287.7	288.2	288.5	289.4	289.4	$4a_{1u}(\pi^*CH_2)$
3	291.9	292.2	291.5	292.6	-	σ^*(C-C)
4	299.6	301.6	300.5	-	-	σ^*(in-ring)
I.P.	290.3	285.4[b]	285.4[b]			

a. Only the final orbital is listed.

b. From solid state XPS, relative to Fermi level[CRC74].

X-ray incident spectra. The ratio of the normal incidence to the glancing incidence spectral intensity ratios should be 1 if the multilayer was randomly oriented. The measured orientation factor of 0.16 indicates considerable orientation. It is possible that this is the effect of a thin multilayer allowing the highly oriented monolayer signal to shine through a less oriented overlayer. This is consistent with the greater polarization dependence of the monolayer than of the multilayer spectra of C_6D_{12} . The orientation factor as defined above is 0.08 for the monolayer. However it is inconsistent with the sharpness of feature 1 since this is greatly broadened in the monolayer state. Thus the multilayer must be oriented as a result of the higher mobility of the saturated molecules or the Pt(III) surface. This may result in epitaxial growth of the C_6D_{12} multilayer into a crystalline solid that is ordered at the surface[J85].

The enhancement of peak 3 in the normal incidence spectra is characteristic of a σ^* resonance in a molecule whose bond axis lies parallel to the Pt(III) surface. The reduction of peak 1 in the normal incidence spectra and enhancement of this feature in the glancing incidence spectra is characteristic of a π^* resonance in a molecule lying parallel to the surface. This is further support for assignment of this feature to the $\pi^*(CH_2)$ level. The $\pi^*(CH_2)$ feature (1) is considerably broader in the monolayer spectrum than in the gas phase or multilayer spectra. This indicates broadening of the π^* level in the monolayer by hybridization into metal levels as previously observed and discussed for benzene.

5.2.3 Unsaturated Hydrocarbons

The gas phase ISEELS spectra of cyclopentene, cylcohexene and cyclo-octatetraene are shown in figure 5.3. Absolute energies and assignments are listed in Table 5.3. The carbon 1s I.P.s of these molecules are estimated to be 290.3 eV in the gas phase as described previously for C_5H_{10} . In all three spectra, an intense peak corresponding to the 1s → π^* transition is observed around 285 eV. The intensity of this peak relative to the C 1s continuum varies considerably. It is most intense in C_8H_8 and weakest in C_6H_{10} . This is not unexpected as C_8H_8 contains the greatest number of carbon carbon double bonds. Feature 2 in the gas phase spectra of C_5H_8 and C_6H_{10} is similar to feature 1 in the gas phase spectra of the saturated cyclic hydrocarbons. Thus these are assigned to a $\pi^*(CH_2)$ level associated with the saturated regions of these molecules. We assign feature 3 in C_5H_8 and C_6H_{10} and feature 4 in C_8H_8 to the σ^*(C-C) resonance. The intensity of the σ^*(C-C) shape resonance(3 or 4) relative to the π^* feature(1) or the non-resonant continuum is highest in C_6H_{10} , consistent with this molecule containing the greatest number of carbon-carbon single bonds. Feature 4 in C_5H_8 and C_6H_{10}, and feature 5 in the C_8H_8 spectrum is assigned to a σ shape resonance associated with the shorter carbon-carbon double bonds.

Figure 5.3

5.3.1 The carbon K-shell ISEELS spectrum of gaseous cyclopentene recorded by electron energy loss of 2.8 keV electrons at 1.0 eV FWHM resolution.

5.3.2 The carbon K-shell ISEELS spectrum of gaseous cyclohexene recorded by electron energy loss of 2.8 keV electrons at 1.0 eV FWHM resolution.

5.3.3 The carbon K-shell ISEELS spectrum of gaseous cyclooctatetraene recorded by electrom energy loss of 2.8 keV electrons at 1.0 eV FWHM resolution.

A background has been subtracted from each spectrum.

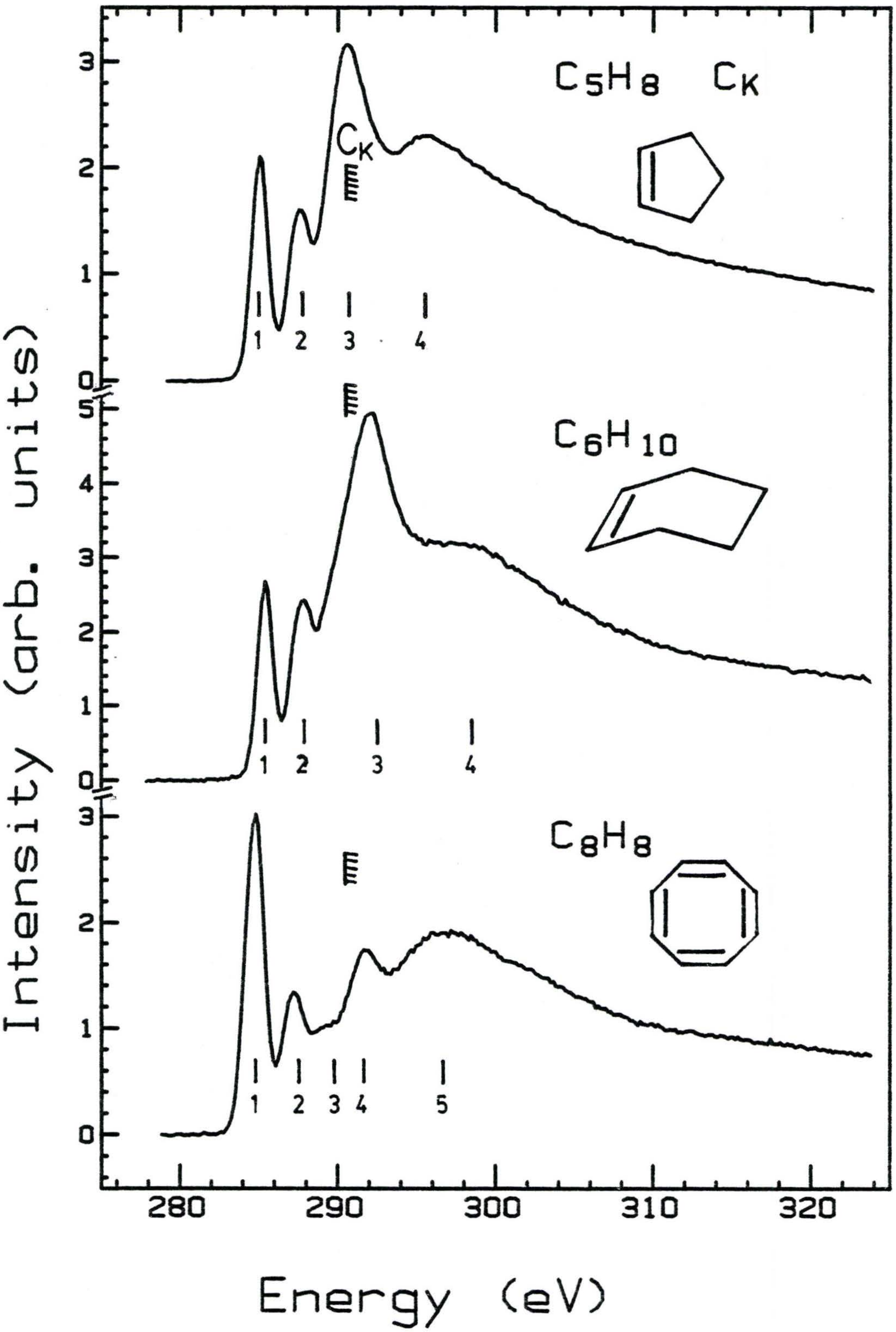
C_5H_8 C_K
C_K
1 2 3 4
C_6H_{10}
1 2 3 4
C_8H_8
1 2 3 4 5
Intensity (arb. units)
0
1
2
3
4
5
280
290
300
310
320
Energy (eV)

Table 5.3

Absolute Energies(eV) and Tentative Assignments of Features Observed in the Carbon K-Shell Spectra of Gaseous Cyclopentene and Cyclohexene

Feature	Energy (± 0.1 eV) C_5H_8	C_6H_{10}	Assignment[a]
1	285.0[b]	285.3[b]	$\pi^*(C=C)$
2	287.6	287.7	$\pi^*(CH_2)$
3	290.6	292.0	$\sigma^*(C-C)$
4	295.6	298.5	$\sigma^*(C=C)$
I.P.	290.3[c]	290.3[c]	

a. Only the final orbital is listed.

b. The first feature in C_5H_8 is 2.4(1) eV below the 1s → π^* transition in CO. The first feature in C_6H_{10} is 2.1(1) eV below the 1s → π^* transition in CO(287.40 eV)[SB84].

Again, as with the π^*(C-C) feature(1) it is most intense in C_8H_8, the molecule with the greatest number of C=C bonds. The weak continuum features observed in the spectra of the saturated hydrocarbons((4) in Figure 5.1) which were attributed to a second σ^* resonances are not observed in the spectra of the unsaturated species possibly because they are masked by the more intense σ^*(C=C) resonances.

The gas phase spectrum of C_8H_8 differs in some respects from those of C_5H_8 and C_6H_{10}. Cyclo-octatetraene(COT) is a non-aromatic, conjugated cyclic system whose most stable conformation is a tub structure with D_{2d} symmetry[FK78]. It has three π^* antibonding orbitals($3a_2$, 8e and $4b_1$) to which promotion of C 1s electrons may occur. The orbital ordering is thought to be $3a_2$, 8e and $4b_1$ [FK78] with a 1 to 2 eV separation between the $3a_2$ and 8e levels and again between the 8e and $4b_1$ levels. Thus features 1, 2 and 3 are tentativley assigned to transitions to the $3a_2$, 8e and $4b_1$ orbitals respectively. Peaks 4 and 5 correspond to the σ(C-C) and σ(C=C) shape resonances.

5.2.4 Comparison to Condensed Phase NEXAFS Spectra

The NEXAFS spectra of solid and monolayer C_5H_8 and C_8H_8, recorded by Stŏhr, Sette and Johnson[SSJ85], are shown in Figures 5.4 and 5.5. The energies and peak assignments are listed in Tables 5.4

Figure 5.4

5.4.1 The carbon K-shell ISEELS spectrum of gaseous cyclopentene.

5.4.2 The carbon K-shell spectrum of solid(multilayer) cyclopentene recorded at normal incidence.

5.4.3 The carbon K-shell spectrum of solid(multilayer) cyclopentene recorded at glancing incidence.

5.4.4 The carbon K-shell spectrum of a monolayer of cyclopentene on Pt(III) at 170K recorded at normal incidence.

5.4.5 The carbon K-shell spectrum of a monolayer of cyclopentene on Pt(III) at 170K recorded at glancing incidence.

A background has been subtracted from each spectrum.

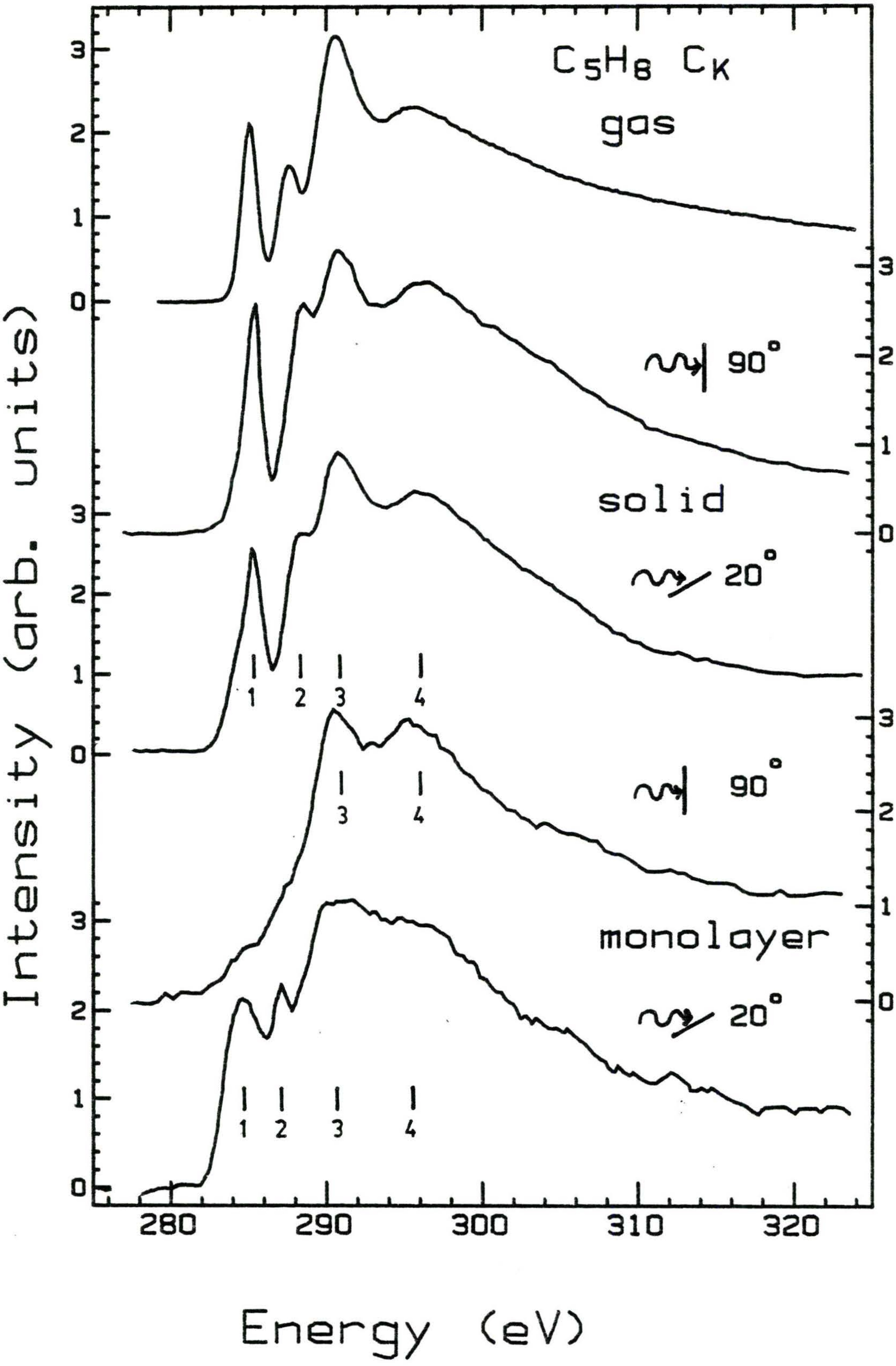
C_5H_8 C_K
gas
solid
monolayer
90°
20°
90°
20°
1
2
3
4
3
4
1
2
3
4
Intensity (arb. units)
Energy (eV)
280
290
300
310
320
0
1
2
3

Table 5.4

Absolute Energies(eV) and Tentative Assignments of Features Observed in the Carbon K-Shell Spectra of Gas Phase, Multilayer and Monolayer Cyclopentene on Pt(III)

Feature	Gas	Multilayer		Monolayer		Assignment[a]
		90°	20°	90°	20°	
	±0.1 eV	±0.5 eV	±0.5 eV	±0.5 eV	±0.5 eV	
1	285.0	285.2	285.2	-	284.6	π^*(C=C)
2	287.6	288.4	288.3	-	287.0	π^*(CH_2)
3	290.6	290.8	290.8	290.6	290.8	σ^*(C-C)
4	295.6	296.0	295.8	295.0	296.3	σ^*(C=C)
I.P.	290.3[b]					

a. Only the final orbital is listed.

b. Estimated from the I.P.s of similar hydrocarbons[BCJ80].

and 5.5. As with C_6H_{12} and benzene and pyridine, the condensed phase spectra are generally similar to the gas phase ones indicating that the features are predominantly intramolecular.

The multilayer spectra of cyclopentene show a lesser degree of polarization dependence than those of cyclohexane. A similar analysis of the relative peak intensities yields an orientation factor of 1.2 incidating that the multilayer is essentially randomly oriented. By contrast, the normal incidence spectrum of monolayer C_5H_8 shows only the σ^*(C-C) and σ^*(C=C features(3 and 4). This, along wih the absence of the π^* resonances, is consistent with an oriented chemisorbed geometry with the double bond parallel to the metal surface. The glancing incidence monolayer spectrum shows enhancement of the π^* resonances(features 1 and 2) and weak σ^* intensity, consistent with the spectral assignments and the proposed surface geometry. The residual σ^* intensity indicates that the molecule does not lie completely flat on the surface. This suggests that cyclopentene retains its open envelope structure on the surface so that the portion of the σ(C-C) shape resonance from the carbon atom located above the molecular plane gives rise to the σ^* intensity in the glancing incidence spectrum. A possible metal-hydrogen steric effect may play a role in giving residue σ^* intensity. This would result in a tilting of the molecule towards the surface normal.

The NEXAFS multilayer spectrum of C_8H_8 taken at normal

Figure 5.5

5.5.1 The carbon K-shell spectrum of gaseous cyclo-octatetraene.

5.5.2 The carbon K-shell spectrum of solid(multilayer) cyclo-octatetraene recorded at normal incidence.

5.5.3 The carbon K-shell spectrum of solid(multilayer) cyclo-octatetraene recorded at glancing incidence.

5.5.4 The carbon K-shell spectrum of a monolayer of cyclo-octatetraene on Pt(III) at 210K recorded at normal incidence.

5.5.5 The carbon K-shell spectrum of a monolayer of cyclo-octatetraene on Pt(III) at 210K recorded at glancing incidence.

A background has been subtracted from each spectrum.

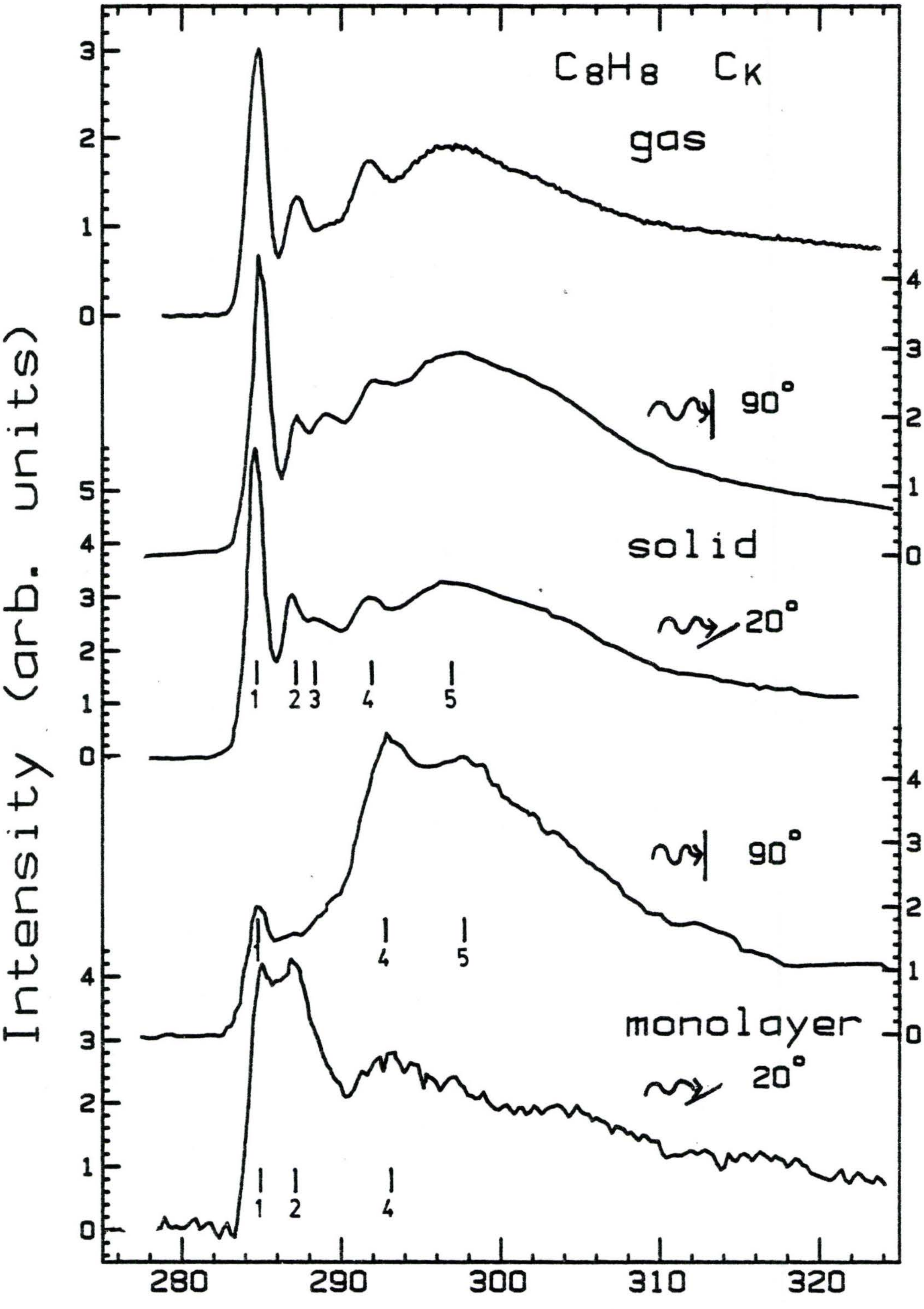
C8H8 CK
gas
solid
monolayer
90°
20°
90°
20°
1 2 3 4 5
4 5
1 2 4
Intensity (arb. units)
Energy (eV)
280
290
300
310
320
0
1
2
3
4
5

Table 5.5

Absolute Energies(eV) and Tentative Assignments of Features Observed in the Carbon K-Shell Spectra of Gas Phase, Multilayer and Monolayer Cyclooctatetraene on Pt(III)

Feature	Gas	Multilayer		Monolayer		Assignment[a]
		90°	20°	90°	20°	
	±0.1 eV	±0.5 eV	±0.5 eV	±0.5 eV	±0.5 eV	
1	284.8[b]	284.9	284.6	284.7	285.0	$\pi^*(3a_2)$
2	287.3	287.2	287.0	-	286.9	$\pi^*(8e)$
3	289.3	288.9	288.4	-	-	$\pi^*(4b_1)$
4	291.8	291.9	291.8	292.8	292.8	σ^*(C-C)
5	296.9	297.0	296.5	297.5	-	σ^*(C=C)
I.P.	290.3[c]					

a. Only the final orbital is listed.

b. This feature is found 2.6(1) eV below the 1s → π^* transition in CO(287.40 eV)[SB84].

incidence shows one distinct difference from the gas phase spectrum. Whereas feature 3 in the gas phase spectrum is barely noticeable, it is present as a definite peak in the normal incidence multilayer spectrum. Feature 3 is less well defined in the glancing incidence spectrum. The presence of features 2 and 3 in the condensed phase spectra of COT indicates that they are not Rydberg orbitals and supports their assignment to the π^* orbitals. It is interesting to note that, relative to feature 1, peaks 2 and 3 are somewhat weaker in the gas phase spectrum of COT than in the condensed phase. This may reflect an increased intensity in the condensed phase spectra due to intermolecular and molecule-surface interactions.

Features 4 and 5 dominate the normal incidence monolayer spectrum indicating that the majority of the C-C bonds in COT are parallel to the metal surface. The presence of feature 1 shows that not all of the π^* orbitals are oriented similarly. This seems reasonable in view of the most stable tub conformation of cyclo-octatetraene. In the glancing incidence spectrum, the π^* orbitals show intensity enhancement. The third π^* transition is masked by the other two π^* transitions which are significantly broadened by hybridization with the metal unoccupied states.

5.3 Continuum Resonances in Cyclic Hydrocarbons

The linear correlation between bond length and shape resonance position has been able to predict bond lengths fairly accurately in small "diatomic-like" molecules[SSH84]. The positions of the shape resonances in the cyclic hydrocarbons have been compared to the shape resonance positions predicted from the actual bond lengths. The measured shape resonance positions are plotted against the bond lengths in Figure 7.5 along with the Z=12 correlation line which was used to obtain the predicted resonance position. The data is tabulated in Table 7.1.

In general, the predicted values are in reasonable agreement with the experimental values. The agreement was closest on the shape resonance position of carbon-carbon single bonds, but somewhat worse for the carbon carbon double bonds.

The rather large deviation in C_5H_8 for the σ_{C-C} shape resonance position may be due, at least in part, to the extra strain in the ring. The deviations in both shape resonance position in C_8H_8 may be a result of the partial conjugation of this molecule. This is explained in detail in Chapter 7.

5.4 Conclusions

The carbon K-shell excitation spectra of gas phase C_5H_8, C_5H_{10}, C_6H_{10}, C_6H_{12} and C_8H_8 have been recorded at moderate resolution and all features assigned. The assignments of the features are based, in part, on available condensed phase NEXAFS spectra of C_5H_8, C_6H_{12} and C_8H_8 This assignments include a $\pi^*(CH_2)$ level which was not considered previously in the interpretation of the core excitation spectra of other saturated hydrocarbons[HB77]. A continuum feature which is thought to be a second σ^*_{C-C} level has been assigned in the spectra of the unsaturated molecules. The positions of the predicted σ shape resonances were in reasonable agreement with the experimental positions.

CHAPTER 6

INNER SHELL ELECTRON ENERGY LOSS SPECTROSCOPY OF SOME HETEROCYCLIC MOLECULES

6.1 Introduction

In this chapter, ISEELS spectra of gaseous furan(C_4H_4O), pyrrole(C_4H_4N), tetrahydrofuran(C_4H_8O or THF), pyrrolidine(C_4H_9N) and piperdine($C_5H_{11}N$) are discussed. Heterocyclic molecules such as these are important in many organic and biochemical reactions. Furan and pyrrole in particular, have been the topics of extensive study[FMK76]. The ISEELS spectra of these molecules will be compared to their cyclic hydrocarbon analogs and thus the effect of the heteroatom on the electronic structure of the ring may be observed. The predicted results from the σ shape resonance position correlation[SSH84] will be compared to the information gathered from the presented spectra. Any differences between the predicted and experimental results will be documented and discussed.

6.2 Estimation of Ionization Potentials

Wherever possible, gas phase XPS ionization potentials have been used for the 1s electron's I.P. in both carbon and heteroatoms. In certain cases XPS data was not available. To allow calculation of term values and shape resonances positions some estimate of the 1s I.P. was necessary. Such estimates were made for the C 1s and O 1s I.P.s of THF and the C 1s I.P.s of C_4H_9N and $C_5H_{11}N$.

The C 1s I.P. of THF was estimated by examining available gas phase XPS data for similar compounds. The closest to THF were dimethyl ether and ethanol. The 1s I.P. of the carbon in these molecules nearest the oxygen is 292.3 and 292.5 eV respectively. The 1s I.P. of the second carbon in ethanol is 291.1 eV. The values in THF should be similar to these. The C 1s I.P.s for THF are estimated to be 292.4 eV and 291.1 eV for the first and second carbons respectively (see Figure 6.3.1). The O 1s I.P. in the forementioned molecules is 538.6 eV and the O 1s I.P. of THF is estimated to be equal to this value.

The gas phase C 1s I.P.s were also unavailable for both pyrrolidine and piperdine. The C 1s I.P.s in CH_3NH_2 and $(CH_3)_3N$ are 291.6 eV and 291.3 eV. The C 1s I.P. of the carbon nearest the nitrogen in C_4H_9N and $C_5H_{11}N$ is expected to be similar to this and is given a value of 291.5 eV. The effect of the nitrogen is not expected to disturb the ring as much as the oxygen in THF and thus the second carbon is given an I.P. of 290.5 eV, closer to that of the hydrocarbon ring. In all cases the expected deviation is thought to be less than ±0.5 eV.

6.3 Furan

6.3.1 Furan Carbon K-Shell ISEELS Spectrum

Furan is an aromatic five membered ring with C_{2v} symmetry. The molecule is isoelectronic with the cyclopentadienyl anion. Unfortunately, no ISEELS data exist as yet for the cyclopentadienyl anion, so a comparison between furan and its closest analog is not possible. Since furan is aromatic, it should be possible to make comparisons to benzene or pyridine, a six membered heterocyclic aromatic. The carbon K shell electron energy loss spectrun of furan is shown in Figure 6.1. The energies and assignments of the features in the spectra are listed in Table 6.1.

Analysis of the furan molecule indicates that there are two antibonding π orbitals which are of $3b_1$ and $2a_2$ symmetry[JS73]. Optical and valence EELS spectroscopy[P40, FMK76] and theoretical calculations[SC65, AFL79, JS73] all indicate that the $3b_1$ orbital is lower in energy than the $2a_2$. This energy difference appears to be on the order of 2eV, in the previously mentioned studies. In addition, furan has two different carbon 1s environments which are separated by 1.2eV[BEJ83]. Thus four $1s \rightarrow \sigma^*$ excitation features are expected in the carbon K shell spectrum of furan with the resolution available. The first two features are assigned to transitions to the $3b_1$ orbital from the two carbon 1s states. The separation observed is 0.9eV which is consistant with the expected separation of 1.2eV. The third and fourth features are assigned to transitions to the $2a_2$ orbital from the different carbon 1s levels. These two features show a separation of 0.8eV. The separation between the $3b_1$ and $2a_2$ orbitals is measured to be 2.8-2.9eV. This is larger than the difference observed in the previous valence studies. The explanation of this lies in the different levels from which excitation is occurring. The different intensities observed in the transitions to the $3b_1$ orbitals can be accounted for by examining the spatial distribution of the molecular orbital[JS73]. The $3b_1$ orbital has greater density on the carbons closer to the oxygen. On the other hand, the $2a_2$ orbital has equal density on the two different carbons and as a result appear, in the carbon K shell spectrum, as peaks with equal intensity.

The two remaining features(5 and 6) present an interesting dilemma. They are assigned to 1s $\rightarrow \sigma^*$ transitions or σ shape resonances. This type of resonance is known to exist for many molecules and dominates the continuum of the larger molecules examined in this thesis. The treatment of σ shape resonances by Sette et al[SSH84] has indicated that such resonances show characteristic energies, with respect to the I.P., for different bond

Figure 6.1

6.1.1 The carbon K-shell spectrum of gaseous furan recorded by electron energy loss of 2.8 keV electrons at 0.6 eV FWHM resolution.

6.1.2 The oxygen K-shell spectrum of gaseous furan recorded by electron energy loss of 3.0 keV electrons at 0.6 eV FWHM resolution.

A background has been subtracted from both spectra.

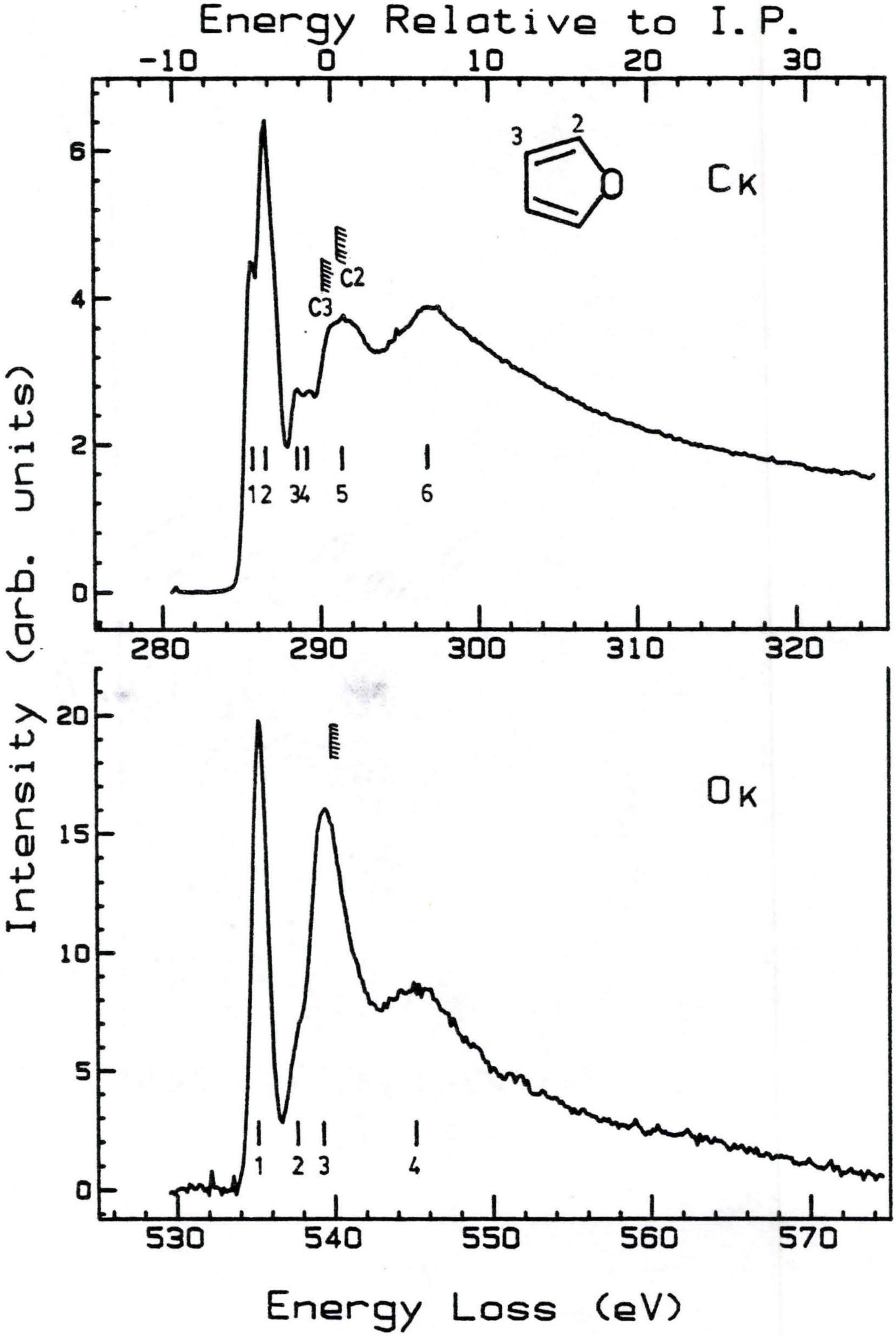
Energy Relative to I.P.
-10
0
10
20
30
3
2
O
CK
C2
C3
1 2 3 4 5 6
6
4
2
0
280
290
300
310
320
Intensity (arb. units)
OK
1 2 3 4
20
15
10
5
0
530
540
550
560
570
Energy Loss (eV)

Table 6.1

Absolute Energies(eV), Term Values and Tentative Assignments for Observed Features in the K-Shell Energy Loss Spectra of Gaseous Furan

Edge	Feature	Energy(±0.1 eV)	Term Value(eV)		Assignment[a]	
			C_2	C_3	C_2	C_3
C_K	1	285.6	-	4.7	-	$\pi^*(3b_1)$
	2	286.5[b]	5.0	-	$\pi^*(3b_1)$	-
	3	288.5	-	1.8	-	$\pi^*(2a_2)$
	4	289.3	2.2	-	$\pi^*(2a_2)$	-
	5	291.4	-0.7[c]		σ^*	
	6	297.0	-6.3[c]		σ^*	
	C_2IP	291.5[d]	-		-	
	C_3IP	290.3[d]	-		-	
O_K	1	535.3[e]	4.7		$\pi^*(3b_1)$	
	2	537.6	2.4		3p	
	3	539.4	0.6		σ^*	
	4	545.3	-5.3		σ^*	
	IP	540.0[d]	-		-	

a. Only the final orbital is listed.

b. This feature is located 4.3(1) eV below the C_K 1s → π^* transition in CO_2(290.7(1) eV)[W74].

c. Determined from the average of the C 1s environments.

d. From XPS[BEJ84].

e. This feature is located 1.1(1) eV above the O_K 1s → π^* peak of CO(534.21(9) eV)[SB84].

lengths of a particular Z value. Furan[LB76] contains two distinct carbon carbon bonds and one carbon oxygen bond. The simple shape resonance/bond length correlation indicates that there should be three resonances in the carbon K shell spectrum of furan corresponding to the three different bond lengths. However, only two resonances in the continuum are observed, and they are not in the positions expected from the simple correlation. My interpretation is that since furan is aromatic, its resonances should be treated in a similar manner to those in benzene and pyridine as outlined in Chapter 4. Further dicussion of this is given in Chapter 7.

6.3.2 Furan Oxygen K-Shell ISEELS Spectrum

The oxygen K shell electron energy loss spectrum of furan is shown below that of the carbon in Figure 6.1.2. The energies and assignments of the observed features are listed in Table 6.1.

There are only four distinct features in the oxygen K shell spectrum of furan. The first feature is assigned to a 1s → σ^* transition. This feature is noticably narrower than that in the carbon spectrum and has only one peak. In an oxygen 1s excitation the symmetry remains C_{2v} and by dipole selection rules only the 1s → $\sigma^*(3b_1)$ is allowed.

Feature 3 has on its low energy side a small shoulder, labelled as feature 2. This is assigned to a 3p Rydberg level based on its term value of 2.4 eV[R74]. Peaks 3 and 4 are analogous to features 5 and 6 in the carbon K shell spectrum. It is expected that the transitions from the oxygen 1s state will be to a similar set of valence antibonding orbitals within any symmetry restriction. Thus these features are also assigned to σ shape resonances. The presence of two features in the oxygen K shell spectrum is further indication that furan should be treated in a similar manner to pyridine since only one σ(C-O) resonance is predicted by simple theory[SSH84]. This is discussed further in Chapter 7.

6.4 Pyrrole

6.4.1 Pyrrole Carbon K-Shell ISEELS Spectrum

Pyrrole is another aromatic five membered ring which is isoelectronic with furan. In pyrrole the oxygen is replaced by a NH group. The spectra of pyrrole might then be expected to resemble that of furan and pyridine. The carbon K shell electron energy loss spectrum of pyrrole and the energies of the observed features are presented in Figure 6.2 and Table 6.2 respectively.

As with furan, pyrrole should also exhibit four π^* features.

The two carbon 1s environments in pyrrole are separated by 1.0eV[BEJ83]. This makes separation of two different carbon 1s levels more difficult since it is much nearer the limit of available resolution. Valence shell studies indicate that the two π^* orbitals, $3b_1$ and $2a_2$, are separated by 0.9eV[PCW53]. This has been confirmed by ab-initio SCF-CI calculations[TNN77]. In light of the furan study, the first feature in the carbon K shell spectrum of pyrrole is assigned to a transition to the $3b_1$ orbital and the second feature is assigned to the $2a_2$ orbital. Improvement in resolution would allow the transitions from the different carbon environments to be observed. The $3b_1$ and $2a_2$ orbitals show a separation of 1.6eV which, as in furan, is greater than that observed in the previous valence studies[PCW53, TNN77]. This is again attributed to the different levels from which excitation is occurring.

As with furan, pyrrole is also aromatic and thus it may be expected to show continuum resonances similar to benzene and pyridine. Indeed, pyrrole is considered to be more aromatic than furan and examination of its bond lengths of 1.42, 1.38 and 1.37Å for the C-C, C=C and C-N bonds, respectivily[LB76], tend to indicate that the molecule is more aromatic than furan. It is expected that pyrrole will be less likely to exhibit continuum resonances that are similar to those seem in non-aromatic molecules than was furan. However, features 3,4 and 5 are in good agreement with the predictions of the simple relationship. While it is tempting to

Figure 6.2

6.2.1 The carbon K-shell spectrum of gaseous pyrrole recorded by electron energy loss of 2.8 keV electrons at 0.6 eV FWHM resolution.

6.2.2 The nitrogen K-shell spectrum of gaseous pyrrole recorded by electron energy loss of 2.9 keV electrons at 0.6 eV FWHM resolution.

A background has been subtracted from both spectra.

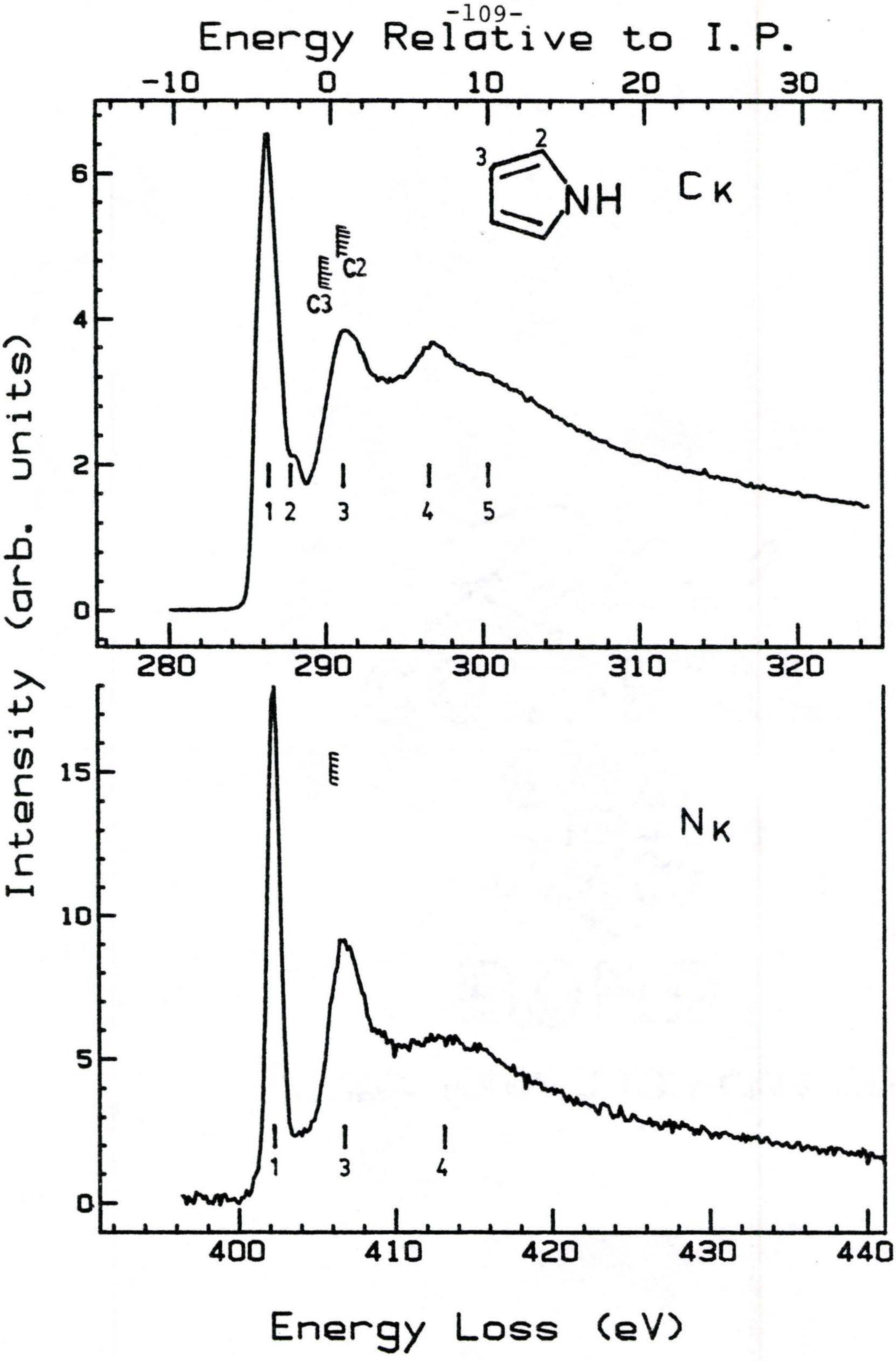
Energy Relative to I.P.
-10
0
10
20
30
6
4
2
0
3
2
NH
C K
C3
C2
1 2 3 4 5
280
290
300
310
320
15
10
5
0
N K
1 3 4
400
410
420
430
440
Intensity (arb. units)
Energy Loss (eV)

assign these features to resonances from the three different bond lengths it is my opinion that this is not correct. Feature 5 has no counterpart in the furan carbon K shell spectrum, where it would be more likely to occur. This feature is very broad and weak making accurate determinations of its energy difficult. I believe that this feature is much more likely to be a multielectron excitation which is unique to pyrrole. The nitrogen K shell spectrum of pyrrole(Sec. 6.4.2) indicates that the aromatic treatment put forth in Chapter 4 is correct in the interpretation of continuum features in that spectrum. This makes it difficult to accept the one bond, one resonance picture for pyrrole and not for any other aromatic molecule.

6.4.2 Pyrrole Nitrogen K-Shell ISEELS Spectrum

The nitrogen K shell electron energy loss spectrum of pyrrole is presented below the carbon K shell spectrum in Figure 6.2. The energies of the features and tentative assignments are listed in Table 6.2. To an even greater extent than the carbon K-shell spectra, the heteroatom core spectra of pyrrole and furan are similar. The first feature is thus assigned as a $1s \rightarrow \pi^*$ transition. As with furan dipole selection rules limit this to a $1s \rightarrow 3b_1$ transition.

Table 6.2

Absolute Energies(eV), Term Values and Tentative Assignments for Observed Features in the K-Shell Energy Loss Spectra of Gaseous Pyrrole

Edge	Feature	Energy(±0.1 eV)	Term Value(eV)		Assignment[a]	
			C_2	C_3	C_2	C_3
C_K	1	286.3[b]	4.5	3.5	$\pi^*(3b_1)$	$\pi^*(3b_1)$[c]
	2	287.9	2.9	1.9	$\pi^*(2a_2)$	$\pi^*(2a_2)$
	3	291.3	-0.9[d]		σ^*	
	4	296.8	-6.4[d]		σ^*	
	5	301.5	-11.1[d]		?	
	C_2IP	290.8[e]	-		-	
	C_3IP	289.8[e]	-		-	
N_K	1	402.3[f]	3.8		$\pi^*(3b_1)$	
	2	405.9	0.2		4p	
	3	406.7	-0.6		σ^*	
	4	413.4	-7.3		σ^*	
	IP	406.1[e]	-		-	

a. Only the final orbital is listed.

b. This feature is located 4.4(1) eV below the C_K 1s → π^* transition in CO_2(290.7(1) eV)[W74].

c. Not resolved as separate features.

d. Average of the two C 1s environments.

e. From XPS[BEJ84].

f. This feature is located 1.2(1) eV above the N_K 1s → π^* transition in N_2(401.1(1) eV)[SB84].

The two remaining major resonances(2 and 3) are also similar in appearance to those found in the oxygen K shell spectrum of furan and are assigned correspondingly to σ shape resonances. The presense of two resonances where only one might be expected is indicative of delocalized σ states as discussed in Chapter 7.

6.5 Tetrahydrofuran

6.5.1 Tetrahydrofuran Carbon K-Shell ISEELS Spectrum

The carbon K shell electron energy loss spectrum of THF, a saturated, five membered, heterocyclic, is shown in Figure 6.3. The energies of the observed features are listed in Table 6.3. Tetrahydrofuran is the oxygen heterocyclic analog of cyclopentane and thus the carbon K shell spectrum of THF is expected to be similar to that of cyclopentane. While the spectra are not precisely the same, some similarites can be noted.

In cyclopentane a low lying π^* state associated with a CH_2 bond has been identified(Chapter 5). This feature would be expected to be seen in THF. Feature 2 is similar to the $1s \rightarrow \pi^*(CH_2)$ feature in cyclopentane and is thus given the same assignment. This feature is slightly more intense that in cyclopentane and at higher energy. There is also a small shoulder, feature 1, on the larger feature 2.

Figure 6.3

6.3.1 The carbon K-shell spectrum of gaseous tetrahydrofuran by electron energy loss of 2.8 keV electrons at 0.6 eV FWHM resolution.

6.3.2 The oxygen K-shell spectrum of gaseous tetrahydrofuran by electron energy loss of 3.0 keV electrons at 0.6 eV FWHM resolution.

A background has been subtracted from both spectra.

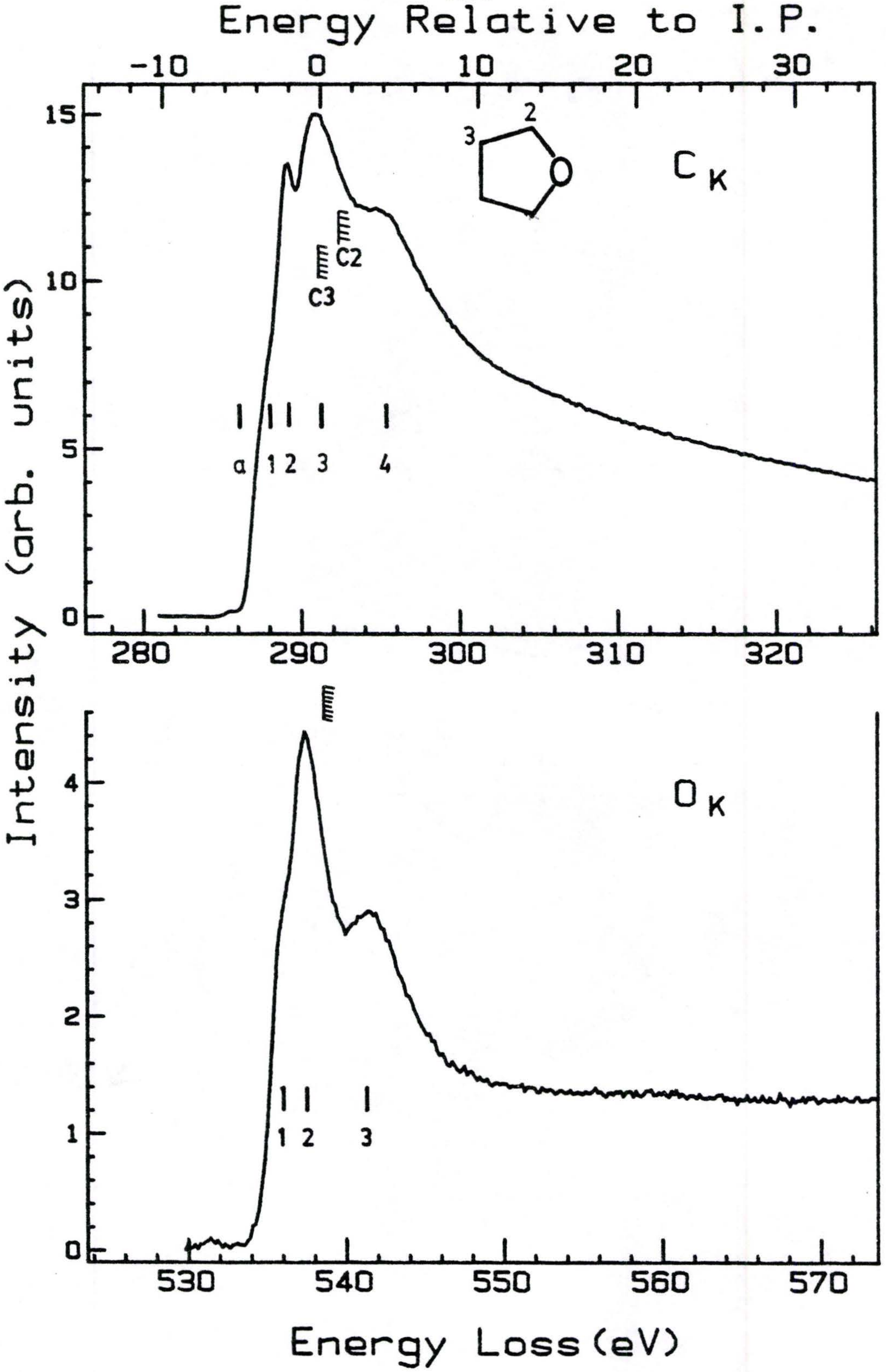
Energy Relative to I.P.
-10
0
10
20
30
15
10
5
0
Intensity (arb. units)
3
2
O
C K
C3
C2
a
1
2
3
4
280
290
300
310
320
4
3
2
1
0
O K
1
2
3
530
540
550
560
570
Energy Loss (eV)

This is believed to be a transition to the $\pi^*(CH_2)$ orbital from the carbons furthest away from the oxygen. The effect of the oxygen appears to give an enhancement of the $\pi^*(CH_2)$ orbitals which are closer to it. The position of these features in pyrrolidine will further document the possible effect of electronegativity in saturated ring systems. Electronegative ligands are known to contain potential barriers which create enhanced intensities for some features[NV68]. The small feature, a, before the first feature, is attributed to impurity peroxide which was not removed in the distillation process.

The third feature is a σ shape resonance associated with the carbon carbon bond. Electron diffraction measurements[LB76] indicate that the carbon carbon bond lengths are all similar and only one σ(C-C) resonance is expected. A σ shape resonance for the C-O bond should be observed and be roughly 40% as intense as the C-C resonance. This feature is not observed, presumably since it overlaps with the C-C resonance. The fourth feature is too far from the C_K I.P. to be assigned to the σ(C-O) resonance. This feature is similar to the last feature in cyclopentane. This was assigned to a second σ shape resonance resulting from the overlap of in-ring atomic orbitals(see Chapter 7).

Table 6.3

Absolute Energies(eV) and Tentative Assignments for Observed Features in the K-Shell Energy Loss Spectra of Gaseous Tetrahydrofuran

Edge	Feature	Energy(±0.1 eV)	Term Value(eV)		Assignment[a]	
			C_2	C_3	C_2	C_3
C_k	a	285.4			peroxide	
	1	287.3	-	3.8	-	$\pi^*(CH_2)$
	2	289.2	3.2[b]	-	$\pi^*(CH_2)$	-
	3	291.0[c]	0.8[b]		$\sigma^*(C-C)$	
	4	294.9	-3.1		σ^*(in-ring)[d]	
	C_2IP	292.4[e]	-		-	
	C_3IP	291.1[e]	-		-	
O_K	1	536.0	2.6		$\pi^*(CH_2)$	
	2	537.4[f]	1.2		$\sigma^*(C-C)$	
	3	541.4	-2.8		σ^*(in-ring)[d]	
	IP	538.6[e]	-		-	

a. Only the final orbital is listed.

b. Determined from the average of the C 1s environments.

c. This feature is located 3.6(1) eV above the C_K 1s → π^* transition of CO(287.4(1) eV)[SB84].

d. See Chapter 7.

e. Estimated(Section 6.2).

f. This feature is located 3.2(1) eV above the O_K 1s → π^* transition in CO(534.21(9) eV)[SB84].

6.5.2 Tetrahydrofuran Oxygen K-shell ISEELS Spectrum

The oxygen K-shell electron energy loss spectrum for THF is shown below the carbon K shell spectrum in Figure 6.3. The energies of the observed features are listed in Table 6.3. The oxygen K shell spectrum parallels that of the carbon K shell spectrum reasonably well, indicating that the transitions are to similar final states.

The first feature, which appears only as a shoulder, is assigned to the same level as in the carbon K shell spectrum, namely the 1s $\rightarrow \pi^*(CH_2)$. The assignment of this orbital indicates that the antibonding levels are not localized between one type of bond but can be reached from a 1s excitation of any atom provided it is dipole allowed.

The second feature is assigned to a σ shape resonance associated with the C-O bond. This resonance is not quite as broad as is the σ(C-C) resonance in the C 1s spectrum. The increased width of the σ(C-C) resonance is likely an indication of the underlying C-O resonance in the C 1s spectrum. The final feature in the oxygen K-shell spectrum is a transition to a second σ shape resonance as described for the carbon K shell spectrum and in further detail in Chapter 7.

6.6 Pyrrolidine

6.6.1 Pyrrolidine Carbon K-Shell ISEELS Spectrum

As with THF, pyrrolidine, C_4H_9N, is another heterocyclic analog of cyclopentane with one of the CH_2 groups replaced by a NH group. Since nitrogen is not as electronegative as oxygen, the perturbation of the ring electronic structure is expected to be less and the carbon K shell spectrum of pyrrolidine, shown in Figure 6.5, should resemble that of cyclopentane more closely than does THF. The energies and assignments of spectral features are listed in Table 6.4.

The carbon K shell energy loss spectrum of pyrrolidine does resemble cyclopentane(see Chapter 5). There are four features that can be identified in the spectrum. The first and second features occur at a similar energy with similar intensities as the 1s → $\pi^*(CH_2)$ feature in cyclopentane. This feature in cyclopentane was quite well resolved even with the reduced resolution of the instrument at the time of that experiment and was well resolved in THF. The effect of the second peak in C_4H_9N is to "fill in the valley" between peak 1 and 3 thus producing a less distinct peak. Both are assigned to 1s → $\pi^*(CH_2)$ transitions similar to those found in cyclic hydrocarbons and furan. In pyrrolidine the π^*CH_2 features are seen with slightly better resolution. This is an effect resulting from the decrease in electronegativity in replacing the

Figure 6.4

6.4.1 The carbon K-shell spectrum of gaseous pyrrolidine by electron energy loss of 2.8 keV electrons at 0.6 eV FWHM resolution.

6.4.2 The nitrogen K-shell spectrum of gaseous pyrrolidine by electron energy loss of 2.9 keV electrons at 0.6 eV FWHM resolution.

A background has been subtracted from both spectra.

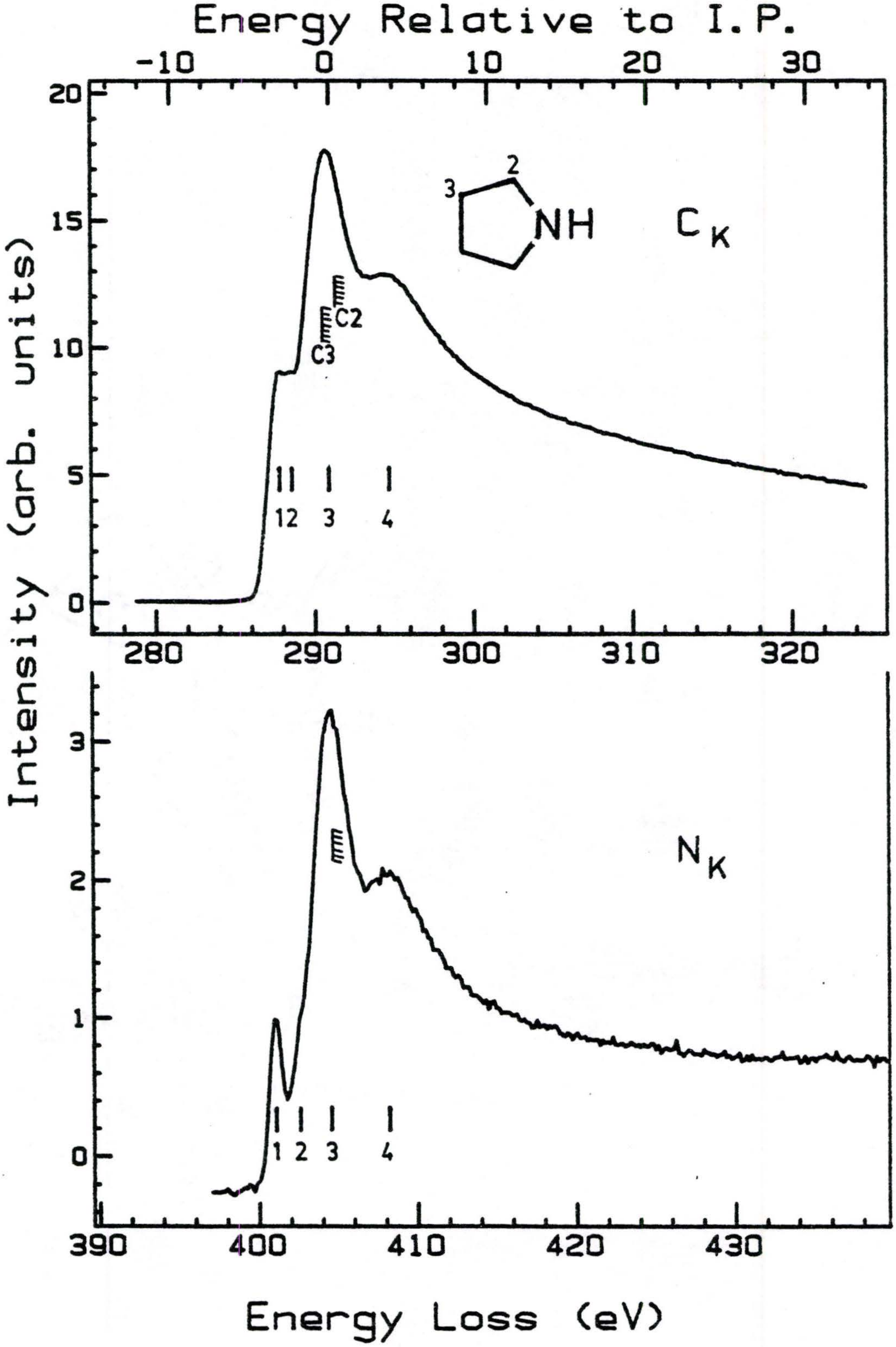
Energy Relative to I.P.
-10
0
10
20
30
20
15
10
5
0
280
290
300
310
320
3
2
NH
C K
C3
C2
11
12
3
4
Intensity (arb. units)
3
2
1
0
N K
1
2
3
4
390
400
410
420
430
Energy Loss (eV)

Table 6.4

Absolute Energies(eV) and Tentative Assignments for observed Features in the K-Shell Energy Loss Spectra of Gaseous Pyrrolidine

Edge	Feature	Energy(±0.1 eV)	Term Value(eV)		Assignment[a]	
			C_2	C_3	C_2	C_3
C_K	1	287.7	-	2.8	-	$\pi^*(CH_2)$
	2	288.4	3.1	-	$\pi^*(CH_2)$	-
	3	290.7[c]	0.3[b]		σ^*(C-C)	
	4	294.8	-3.8		σ^*(in-ring)	
	C_2IP	291.5[e]	-		-	
	C_3IP	290.5[e]	-		-	
N_K	1	401.0	3.6		3p(π^*CH_2)	
	2	402.5	2.1		3p	
	3	404.5[f]	0.1		σ^*(C-N)	
	4	408.0	-3.4		σ^*(in-ring)[d]	
	IP	404.6[g]	-		-	

a. Only the final orbital is listed.

b. Average of the two C 1s environments.

c. This feature is located 3.3(1) eV above the C_K 1s → π^* peak of CO(287.4(1) eV)[SB84].

d. See Chapter 7.

e. Estimated(see Section 6.5.3).

f. This feature is located 3.4(1) eV above the N_K 1s → π^* peak of N_2(401.1(1) eV)[SB84].

g. From XPS[BEJ83].

oxygen with the nitrogen.

The major resonance, feature 3, is assigned to the σ shape resonance from the carbon carbon bond. As with THF, there should also be a resonance associated with the carbon heteroatom bond. However, as with THF, none could be observed due to its proximity to the carbon σ shape resonance. Feature 4 is assigned to a second σ shape resonance similar to those seen in cyclopentane and THF. These features are discussed in detail in Chapter 7.

6.6.2 Pyrrolidine Nitrogen K-Shell ISEELS Spectrum

The nitrogen K shell spectrum of pyrrolidine is shown below the carbon K shell spectrum in Figure 6.4. The energies of the observed features are listed in Table 6.4. The nitrogen K shell spectrum shows four features and resembles the carbon K shell spectrum of pyrrolidine.

The first feature originally was thought to be due to impurity N_2 or an air leak. However, leak checking and measurement of an oxygen K shell spectrum showed no sign of any air leak and extensive degassing was done to eliminate any N_2 trapped in the liquid. This confirmed that this was a true spectral feature. This may also be assigned to a $\pi^*(CH_2)$ orbital. The feature is not as close to the main feature as it was in THF. This would appear to be a result of the decrease in electronegativity of the nitrogen.

The second feature, which appears as a small shoulder on the larger third resonance, is assigned to a Rydberg feature. Its term value of 2.1 eV suggests assignment to transitions to a 4s Rydberg orbital. The large resonance on which it sits is the σ shape resonance associated with the carbon nitrogen bond length. The final feature is also assigned to a second σ shape resonance as mentioned previously for THF.

6.7 Piperdine

6.7.1 Piperdine Carbon K-Shell ISEELS Spectrum

The carbon K shell electron energy loss spectrum of piperdine, $C_5H_{11}N$, is shown in figure 6.5 with the energies of the observed features listed in Table 6.5. The carbon K-shell spectrum of piperdine was expected to resemble, even more closely, that of its cyclic hydrocarbon analog, cyclohexane. This would be expected since the replacement of a CH group with a NH group should have even less effect in a six membered ring than a five membered ring.

The first two features in the carbon K shell spectrum of

Figure 6.5

6.5.1 The carbon K-shell spectrum of gaseous piperdine by electron energy loss of 2.8 keV electrons at 0.6 eV FWHM resolution.

6.5.2 The nitrogen K-shell spectrum of gaseous piperdine by electron energy loss of 2.0 keV electrons at 0.6 eV FWHM resolution.

A background has been subtracted from both spectra.

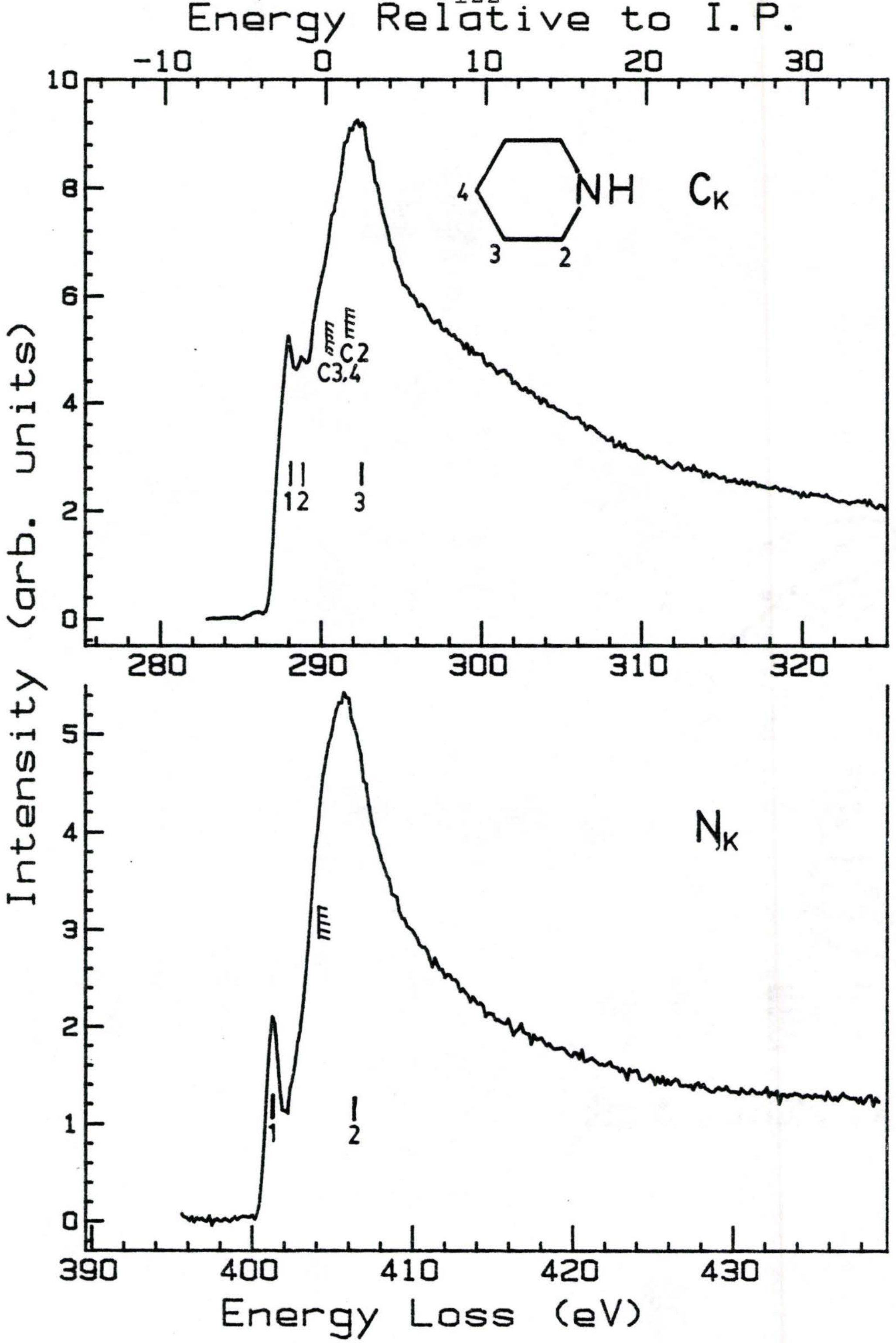
Energy Relative to I.P.
-10
0
10
20
30
10
8
6
4
2
0
4
NH
3
2
C_K
C2
C3,4
1 2
3
280
290
300
310
320
Intensity (arb. units)
5
4
3
2
1
0
N_K
1
2
390
400
410
420
430
Energy Loss (eV)

piperdine are again assigned to the 1s $\rightarrow \pi^*$ CH_2 transitions. As before the two features are a result of two different carbon 1s environments. The first feature is more intense that the second, presumably since there are three carbons contributing to the transition. The third feature is assigned to the σ shape resonance associated with the carbon carbon bond. Again a σ shape resonance which might correspond to the carbon nitrogen bond is not observed. There is also no peak analogous to peak 4 in the carbon K shell spectrum of pyrrolidine. This feature was also less intense in cyclohexane than in cyclopentane(Chapter 5). This indicates that the pattern of excitation observed depends on ring geometry as well as on heteroatom and bond lengths present(see Chapter 7).

6.7.2 Piperdine Nitrogen K-Shell ISEELS Spectrum

The nitrogen K shell electron energy loss spectrum of piperdine is shown below the carbon K shell spectrum in Figure 6.5. The energies of the observed features are listed in Table 6.5.

The N_K spectrum of piperdine again is quite similar to that of the C_K spectrum, indicating that similar transitions are occurring. The first feature is quite intense and is likely due to a transition to a $\pi^*(CH_2)$ type orbital as indicated in pyrrolidine. The unchanging intensity with successive degassing rules out any

Table 6.5

Absolute Energies(eV) and Tentative Assignments for Observed Features in the K-Shell Energy Loss Spectra of Gaseous Piperdine

Edge	Feature	Energy(±0.1 eV)	Term Value(eV)		Assignment[a]	
			C_2	$C_{3,4}$	C_2	$C_{3,4}$
C_K	1	287.9	2.8	-	$\pi^*(CH_2)$	-
	2	288.7	-	1.8	-	$\pi^*(CH_2)$
	3	292.2[c]	-1.2		$\sigma^*(C-C)$	
	C_2IP	291.5[d]	-		-	
	$C_{3,4}$IP	290.5[d]	-		-	
N_K	1	401.2	3.4		$\pi^*(CH_2)$	
	2	405.6[e]	-1.0		$\sigma^*(C-N)$	
	IP	404.6[f]	-		-	

a. Only the final orbital is listed.

b. Average of the three C 1s environments.

c. This feature is located 4.8(1) eV above the C_K 1s → π^* peak of CO(287.4(1) eV)[SB84].

d. Estimated(see Section 6.5.3).

e. This feature is located 1.3(1) eV above the N_K 1s → π^* peak of N_2(401.1(1) eV)[SB84].

f. From XPS[BEJ83].

possibility that this is impurity N_2 in the sample as originally believed. The presence of this transition in the heteroatom core edge spectra of heterocyclic molecules is an indication that this orbital is not highly localized on the carbon atoms.

The second feature is the σ shape resonance from the carbon-nitrogen bond. There are no features beyond this peak suggesting that the second σ shape resonance feature which was present in pyrrolidine is strongly geometry dependent. This was seen in the saturated hydrocarbons (Chapter 5). Since the feature is present at a low intensity in cyclohexane but absent in piperdine, some dependence on the heteroatom must exist(Chapter 7).

6.8 Continuum Resonances in Heterocyclics

The correlation between shape resonance position, δ, and the intramolecular bond distance, R, has given reasonable results on most of the data analyzed so far(Chapters 4, 5 and [SSH84]). In the analysis of the results from the heterocyclic molecules those with simple bonding showed good agreement between predicted and experimental results. In the two aromatic molecules, the results require further interpretation (Chapter 7). The use of intensity weighted averages of the experimental values give much better agreement than does the simple, one bond, one resonance picture. The data is listed in Table 7.1 and shown in Figures 7.1, 7.2 and 7.3.

The heteroatom spectra of the heterocyclic molecules resembled those of the carbon edge quite closely. This is interpreted as transitions to a similar set of antibonding orbitals. In the heteroatom spectra of furan and pyrrole, the first σ shape resonance is more intense, relative to the higher energy resonance, than it is in the carbon spectra. This resonance is approximately where the σ_{C-X} shape resonance would be expected if there was no delocalization of the orbitals (see Chapter 7). The increased intensity of this feature, relative to its counterpart in the carbon spectrum, appears to be a reflection of the decrease in aromaticity of furan and pyrrole relative to pyridine and benzene, where the two resonances are more similar in intensity(see Section 7.3.2).

6.9 Conclusions

The spectra of C_4H_4O, C_4H_5N, C_4H_8O, C_4H_9N and $C_5H_{11}N$ have been recorded by gas phase ISEELS spectroscopy and all observed features given tentative assignments. To my knowledge none of these spectra have been recorded previously.

The saturated heterocyclic molecules showed spectra similar to those seen in their hydrocarbon analogs. The carbon K shell spectra and the heteroatom K shell spectra were quite similar indicating that the transitions observed are to a similar set of molecular orbitals in both cases.

CHAPTER 7

INTERPRETATION OF CONTINUUM FEATURES

7.1 Introduction

As the amount of available data increased, the explanation of certain features in the continuum of more complex molecules became increasingly difficult. There are a number of possible explanations for the various continuum features observed. It is possible to attribute features to σ shape resonances, localized at a particular bond, delocalized σ^* states or multielectron excitations and give reasonable arguments as to why a feature could be any of these. The purpose of this chapter is to discuss each of these possibilities in some detail and subsequently explain the continuum features in the spectrum of the cyclic and heterocyclic molecules studied and reported in Chapters 5 and 6.

7.1.1 The Shape Resonance Picture

The main aim of this section is to discuss the continuum features in terms of a simple one bond, one shape resonance picture. It is this type of reasoning which allowed Sette and co-workers to develop their empirical relationship between σ shape resonance position and bond length. The origins of the shape resonance position model are discussed in detail in Section 1.6. The rationale used by Sette was to treat the outgoing electron as one which is resonantly scattered back and forth between the excited atom and its nearest neighbour. In this treatment, there will be one σ shape resonance for each different bond length. Where the nearest neighbour was hydrogen, this resonance was expected to be very weak due to the poor scattering ability of hydrogen[SSH84]. This treatment worked best where the molecules consisted only of atoms from the first and second rows of the periodic table, and did not exhibit extensive delocalization. Where there is extensive delocalization the empirical relationship developed in [SSH84] appears to break down in its ability to accurately correlate bond lengths and observed continuum features.

7.1.2 Delocalized Sigma States

In Chapter 4, the simple relationship between σ shape resonances and bond length did not initially accurately predict the features observed in the spectra of benzene and pyridine. Nor does it for molecules such as COS, CO_2 or N_2O. In these molecules there is delocalization of the molecular σ^* states and the simple picture of an electron being scattered back and forth between two atoms is lost. In the simpler linear molecules it is also suggested that multiple scattering interference effects may also be important[T81], since these are enhanced in colinear geometries such as CO_2, COS and N_2O.

In benzene the condensed phase polarization NEXAFS spectra showed that the two continuum resonances were both of σ symmetry. A $X\alpha$ multiple scattering calculation[H85] also showed that these two features were due to transitions to σ^* states. The explanation for the observation of two features was that interaction among localized σ^* orbitals produced a set of delocalized molecular σ^* states that were separated in energy as observed experimentally. By taking the intensity weighted average of the observed peak position, a much better fit between the predicted and experimental values of the σ shape resonance position was obtained. This suggests that the simple picture is essentially correct, except that the delocalization seems to split the resonances about the position that the simple picture predicts.

7.1.3 Multielectron Excitation

In cases where a continuum feature cannot be immediately identified as a σ shape resonance it may be assigned to a multielectron process[W74,H78,S84]. In these cases the feature is generally either a double excitation or an XPS shake up like feature. Double excitations, (the simultaneous excitation of a 1s and valence electron) have been detected in ISEELS and are generally fairly sharp features[HB80]. Where XPS satellite structure is available, correlation to shake up features, a 1s ionization accompanied by a valence excitation[SNJ69], have been documented[W74,S84]. These features are broader in the ISEELS continuum and are generally weak. The scarcity of XPS satellite structure data for the larger cyclic species in this thesis makes it difficult to unambiguously assign features in the continuum to shake-up. No XPS shake off features have ever been confirmed in ISEELS spectra.

7.2 Cyclic Hydrocarbons

In Chapter 5 the various features in the continua were assigned but little discussion was given as to the reasoning behind the assignment. Here the spectra will be discussed in greater detail, examining the geometry and bonding of the molecules to arrive at satisfactory explanations of the assignments.

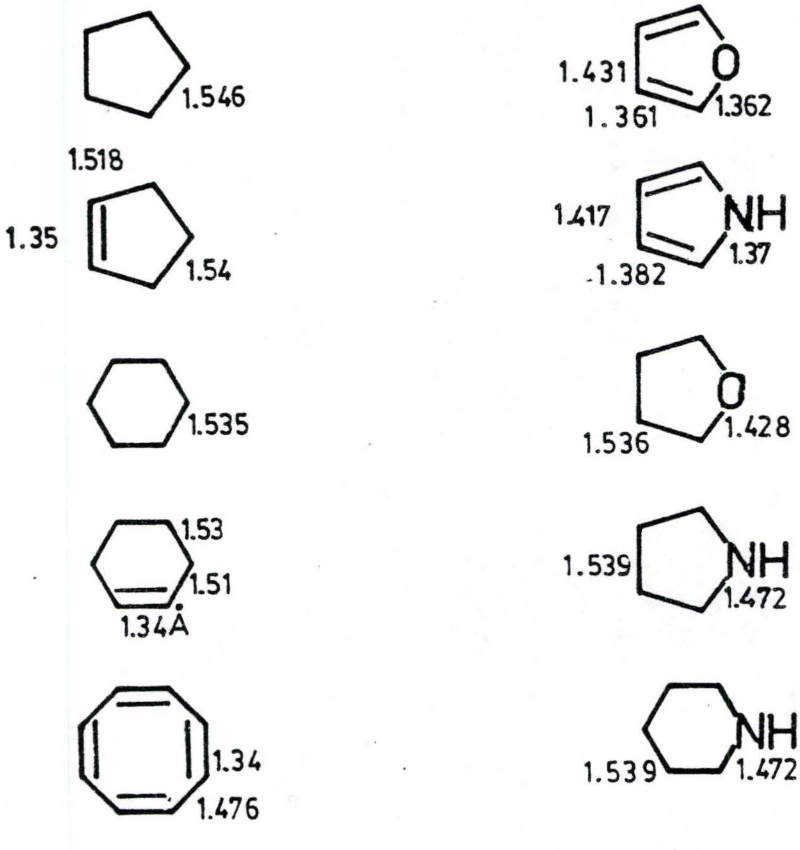

Figure 7.1 The shapes and bond lengths of the cyclic hydrocarbons(Chapter 5) and heterocyclic molecules(Chapter 6).

7.2.1 Geometry of Molecules

The shapes and bond lengths of all of the molecules discussed in Chapters 5 and 6 are shown in Figure 7.1. The prediction of the simple empirical relationship[SSH84] for each molecule is listed in Tables 7.1 to 7.3, along with the data for molecules previously studied. In the unsaturated molecules the simple relationship predicts two σ shape resonances for the C-C and C=C bonds, while for the saturated compounds only one such resonance is predicted.

As previously mentioned, the simple empirical relationship seems to be most applicable when the molecule has little delocalization. In these cases the description of one resonance for each different bond length is accurate. In the saturated molecules this is the case and the first continuum feature is assigned to a σ shape resonance associated with the C-C single bond. The simple relationship can also be used to describe accurately the C-C shape resonances in C_6H_{10} and C_5H_8 as well as the $\sigma_{C=C}$ shape resonance in C_8H_{18}. The theory is less accurate in describing the positions of the σ shape resonances in C_8H_8 and the $\sigma_{C=C}$ shape resonance in C_5H_8. The simple theory of shape resonances also does not predict the second continuum feature in the spectra of the saturated molecules.

7.2.2 Explanation of Continuum Features in Cyclic Hydrocarbons

In the previous section the first continuum features in C_5H_8, C_6H_{10}, C_5H_{10} and C_6H_{12} could all be adequately explained in terms of a shape resonance correlated with one type of carbon carbon bond. In the spectra of the saturated molecules however, there is a second peak not explained by this method. This peak is much more intense in C_5H_{10} than it is in C_6H_{12}. If the simple empirical relationship was followed, the only possible explanation of this feature is an assignment to a σ_{CH} shape resonance. Initially this was considered, but closer investigation showed that such as assignment is inconsistent with the experimental results.

Previously, molecules which have shown evidence of possible σ_{CH} shape resonances are NH_3, CH_4 and H_2O. In all of these, the proposed shape resonance feature was quite weak in comparison to the other spectral features. Such a σ_{C-H} feature would be relatively more intense and easy to detect in molecules where no other continuum resonances might be expected. The poor backscattering ability of the hydrogen atom results in very low intensities even in these molecules. This makes it difficult to justify why the σ_{CH} shape resonance would be as intense as the second continuum feature in C_5H_{10}. Nor can it explain why the relative intensity would drop so dramatically in C_6H_{12}. The addition of one more CH_2 group should, if anything, increase the intensity of a σ_{CH} shape resonance. Thus the

σ_{CH} shape resonance proposal is considered unacceptable. The low intensity of such a feature would be lost in the much greater intensity resulting from the C-C bond resonance.

One alternate explanation for these features is to assign them to a multielectron excitation process. The lack of extensive XPS satellite spectra makes it difficult to confirm or eliminate a shake-up interpretation and thus the possibility that these features are shake-up continua cannot be completely ruled out. Double excitation features, such as those seen in CO[HB80], tend to be sharper than the features observed in the spectra of the saturated hydrocarbons. Thus although an assignment of these features to double excitation is possible, it seems unlikely due to the breadth of the features.

This leaves delocalization and splitting of the σ^* states as the preferred explanation. In cyclobutane it can be shown that the overlap of the localized carbon carbon σ orbitals will produce two sets of $\sigma*$ orbitals[HD71]. A recent X_α multiple scattering calculation[H85] also shows the existence of two distinct σ^* states. These σ^* states can be thought of as occurring due to the overlap of in-ring and out of ring atomic s and p orbitals. If this approach is used then the results are consistent for cyclopentane and cyclohexane. As the ring size increases, the amount of in-ring overlap decreases and the intensity of this σ^* state decreases and broadens. This is what is observed in cyclohexane. In the six membered ring the molecule is in an unstrained geometry and little in-ring overlap should occur. This interpretation could be substantiated by recording the ISEELS spectra of saturated non-cyclic hydrocarbons. If the second σ^* state is a result of the overlap of the in-ring atomic orbitals, then this feature should not be observed.

Similar reasoning explains why the simple relationship gives less accurate results for the $\sigma_{C=C}$ shape resonance position of C_5H_8. If the antibonding σ^* states are affected by ring size in saturated molecules, it is logical to assume that such in-ring overlap would affect the σ^* resonance associated with the C=C bond. This is supported by the fact that the simple theory gives a more accurate prediction in C_6H_{10} where the amount of in-ring overlap is less. It appears that this overlap shifts the $\sigma_{C=C}$ shape resonance to lower energy than predicted.

In C_8H_8 a different situation is thought to exist. This molecule does not have as much in-ring interaction as C_5H_8. However, there is conjugation of the bonds in C_8H_8. The effect of this conjugation is to produce more delocalization of the σ^* levels than in the other non-aromatic molecules. This produces a situation which is akin to the effect in benzene. There are resonances that appear to be associated with a shorter and longer C-C bond but the simple picture cannot accurately describe their positions due to this increase in the delocalization of the electron in the σ^* state. As well, the tub shape of the molecule may result in cross ring orbital overlaps not experienced in the other species.

7.3 Heterocyclic Molecules

7.3.1 Geometry of Molecules

As with the cyclic hydrocarbons, there were some inconsistencies in the predictions of the simple relationship. The greatest deviations from the predictions occurred in furan and pyrrole, both aromatic molecules. The saturated heterocyclic molecules had spectra with continuum resonances close to the predicted positions. The geometries of the heterocyclic molecules are shown in Figure 7.1. The predictions of the simple theory and the actual positions are listed in Tables 7.1, 7.2 and 7.3.

7.3.2 Explanation of Continuum Features in Furan and Pyrrole

As mentioned previously, the predictions of the simple relationship[SSH84] for furan and pyrrole did not agree with the observed spectra. There are essentially two methods to analyze the observed resonances. One can follow the simple relationship in [SSH84] and predict that three resonances should be observed in the carbon K shell spectra, corresponding to a C-X, C-C and C=C bond length. There is only one resonance predicted in the heteroatom spectra. There are two resonances observed in both spectra. If one stays within the framework of the simple empirical relationship the assumption that there is overlap of the different resonances can be used to explain only two features. The second feature in the heteroatom can be assigned to in-ring σ^* states.

The alternative is to treat these molecules similar to benzene and pyridine. In these molecules the buildup of delocalized σ^* states was used to explain why more than one feature was observed. The intensity weighted average(IWA) σ^* position was found to give a better fit of the experimental data to the known C-C bond length. Such averaging also produces a better fit in furan and pyrrole, particularly in the heteroatom spectra.

The IWA is performed by subtracting an estimation of the non-resonant continuum and measuring the area under the peak. The energy of the peak is then multiplied by this area, added to the energy of the second feature, multiplied by its area. This is all divided by the sum of the total area. This is shown in equation 7.1.

$$(A_1E_1+A_2E_2)/A_1+A_2=IWA \qquad 7.1$$

What is believed to be occuring is that in the delocalized electronic structure of aromatic molecules the picture of a photoelectron being scattered back and forth between two well defined centers to be lost. Furan and pyrrole are not as aromatic as benzene and pyridine, a fact born out by the increased intensity of the first continuum feature relative to the second in the heteroatom spectrum of furan and pyrrole as compared to benzene and pyridine. This is a reflection of the excited electron having an enhanced intensity on the heteroatom and its nearest neighbour rather than over the whole molecule. This reduction in delocalization, as illustrated by the heteroatom spectra, may also explain why the carbon K-shell continuum resonances are not accurately described either through the simple one bond one resonance picture or through the IWA process. If delocalization was complete and equal as in benzene, the bond length predicted from the IWA of the continuum resonances and the average bond length should be quite close. This is not the case and probably indicates appreciable localization in the σ^* state although not enough to allow three resonances to be observed. It appears that in molecules such as these the simple correlation will always have some trouble accurately correlating resonance positions with bonds lengths.

It is of interest to note that the boron and nitrogen K-shell spectra of borazine have recently been recorded[GDM85]. The core spectra of this aromatic analog of benzene are very similar to those of benzene and pyridine and the IWA of the continuum resonances in both the B 1s and N 1s spectra provide bond lengths in good agreement with the known geometry. This confirms that aromatic molecules cannot be treated simply by a one bond, one resonance picture. However, as the amount of delocalization decreases the intensity weighted average of the shape resonance position begins to break down.

7.3.3 Explanation of Continuum Features in Saturated Heterocyclics

The oxygen and carbon K shell spectra of THF both show two continuum resonances which are similarly assigned. The remarkable similarity of the spectra, which has been interpreted as transitions to the same set of antibonding levels may be a function of cyclic molecules only. Comparison to the spectra of non-cyclic ethers of similar size would indicate this more clearly. The second resonance feature in the C 1s and O 1s spectra of THF is more intense than the corresponding feature in cyclopentane(see Figure 7.3). This may be due to a potential barrier effect[NF68,D72], or to an increased overlap of the in-ring σ^* states due to the shorter C-O bond.

The σ shape resonances associated with C-C or C-X bonds show excellent agreement with the simple theory. The agreement can be improved with an intensity weighted average of the two resonances but the shift is small compared to that in the aromatic molecules.

The C_{1s} and N_{1s} spectra of pyrrolidine are also quite similar and both of these are similar to cyclopentane and THF. Again, a second continuum feature is observed and assigned to in-ring σ^* states. In pyrrolidine this feature is also more intense than it is in cyclopentane. This suggests that the nitrogen causes more overlap than in the hydrocarbon. The first continuum feature is assigned to the σ_{C-C} shape resonance in both spectra. In both cases the predicted values are in good agreement with the experimental.

The final molecule, piperdine, shows only one resonance in the continuum. The higher energy feature observed in C_4H_9N, C_5H_{10} and C_6H_{12} is not present in either the C_K or N_K shell spectra. Presumably the amount of splitting then is affected by both ring size and the heteratom in the ring. This subject will be discussed further in Section 7.4. It is of interest to note that a feature which could be uniquely identified to the σ_{C-X} resonance was not observed in any of the carbon K spectra. The σ_{C-X} resonance will lie very close to the C_K edge and thus is lost in the larger σ_{CC} shape resonance. The clear increase in the width of the first carbon K shell continuum resonance relative to the corresponding feature in the heteroatom spectra is evidence for this.

7.4 Influence of Ring Size and Heteroatom

In Figure 7.2, the carbon K shell spectra of the three saturated five membered ring systems are plotted. The spectra of the two six membered ring saturated molecules are shown in Figure 7.3. It has already been pointed out that there appears to be a connection between the intensity of the second σ^* shape resonance and geometry. This can be seen very clearly by comparing the five and six membered ring spectra shown in Figures 7.2 and 7.3. The second continuum feature is interpreted in terms of overlap of $\sigma_{(CC)}$ orbitals. As the ring size increases the amount of interaction decreases and the second transition becomes broader and less intense. When going from pyrrolidine to piperdine, the second resonance disappears altogether. This result is somewhat unexpected since the shorter C-N bond length might be expected to increase the overlap of the in-ring σ^* states. There may in fact be as much or more of the second resonance but it may be masked by the broader σ_{C-X} resonances. This then indicates that the heteroatom must affect this overlap in some way. There is not yet enough data to discuss in detail how the heteroatom affects the second σ^* level.

7.5 State of Shape Resonance Position Relationship

Over the course of this thesis and in work done by

Figure 7.2

Comparison of the effect of the heteroatom in the carbon K-shell spectra of C_5H_{10}, C_4H_9N and C_4H_8O.

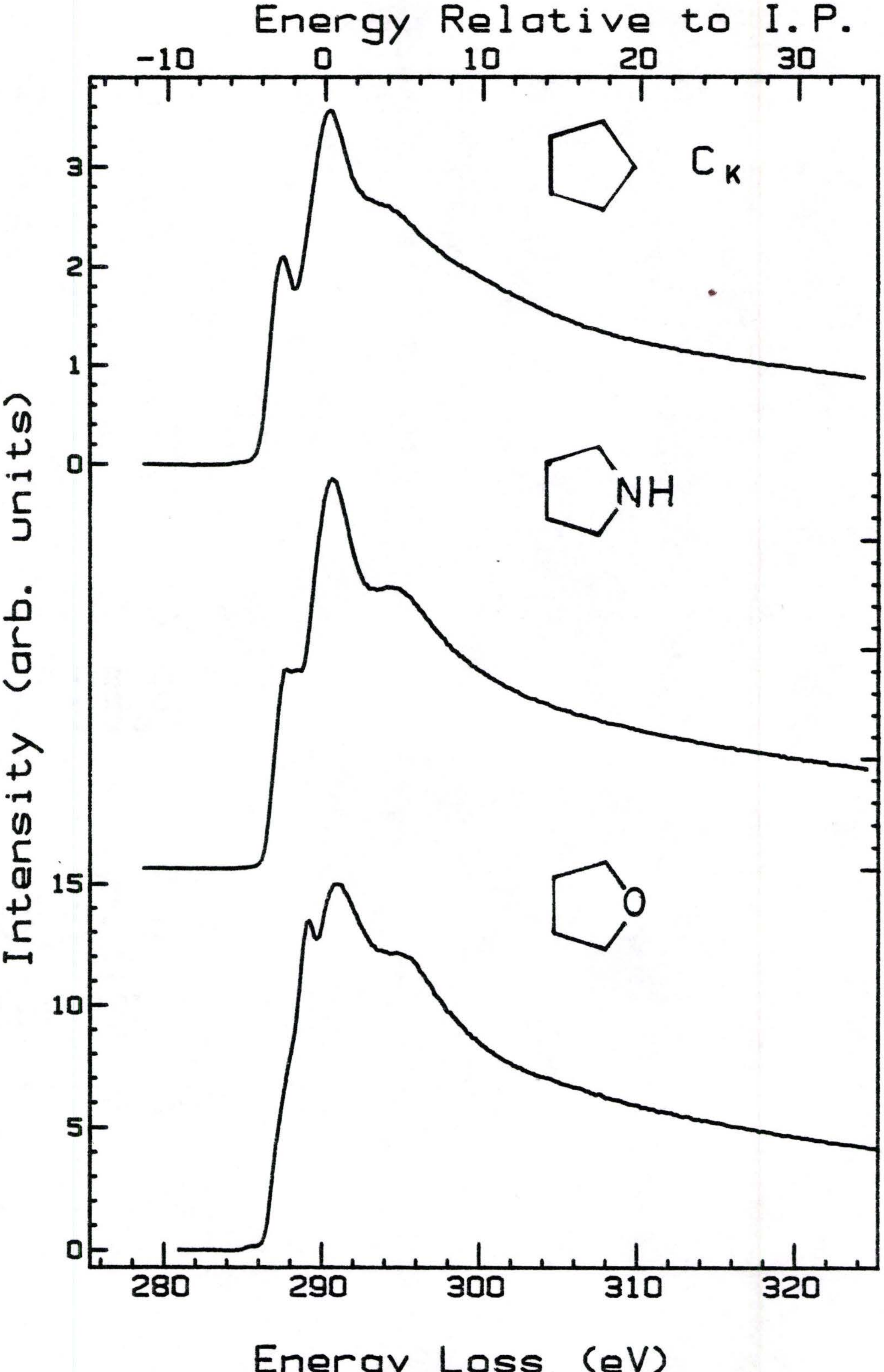
Energy Relative to I.P.
-10
0
10
20
30
C K
NH
O
Intensity (arb. units)
0
1
2
3
0
5
10
15
0
5
10
15
280
290
300
310
320
Energy Loss (eV)

Figure 7.3

Comparison of the effect of the heteroatom in the carbon K-shell spectra of C_6H_{12} and $C_5H_{11}N$.

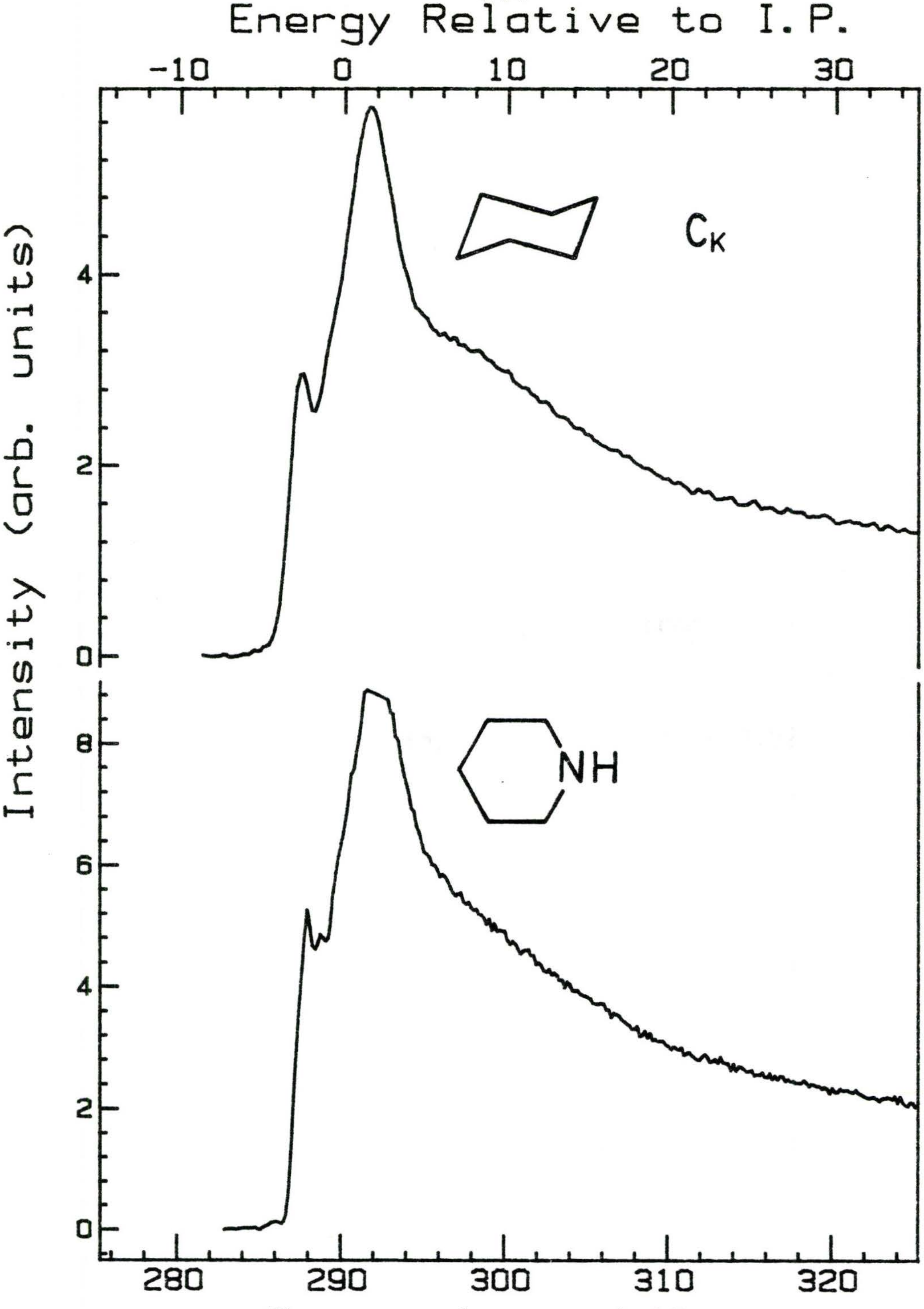
Energy Relative to I.P.
-10
0
10
20
30
C_K
NH
Intensity (arb. units)
0
2
4
0
2
4
6
8
280
290
300
310
320
Energy Loss (eV)

others[H82] the amount of data available for investigating the relationship between bond length and σ shape resonance position has greatly increased. This section will briefly summarize the work done to date. Trends in the data will be pointed out and all data available for Z=12, Z=13 and Z=14 will be summarized.

Overall the empirical relationship appears to hold up reasonably well. The types of molecules that have been subject to treatment by the relationship has varied from simple diatomics to relatively large cyclic systems and aromatics. In most cases the theory predicts bond lengths which are within 0.02Å of the known distance. If the uncertainty in the resonance position measurement is considered to be to ±2 eV, because of the difficulty in accurately determining the position of the broad σ shape resonances then, within this uncertainty, almost all of the data points are found to lie on the correlation line. The theory has the most difficulty in accurately predicting molecules where there is extensive delocalization and the least trouble where there are only simple localized single bonds. An interesting point can be seen on the Z=12 curve, Figure 7.4. The uppermost point is the resonance from acetylene. In earlier versions of this plot this point lay on the correlation line but as the amount of data increased, the slope decreased and now this point is well off the correlation line. Since little data for molecules containing carbon carbon triple bonds is available the point cannot yet be deemed anomalous. In the Z=13

Figure 7.4

Plot of shape resonance position(δ) versus the bond length(R) for Z=12.

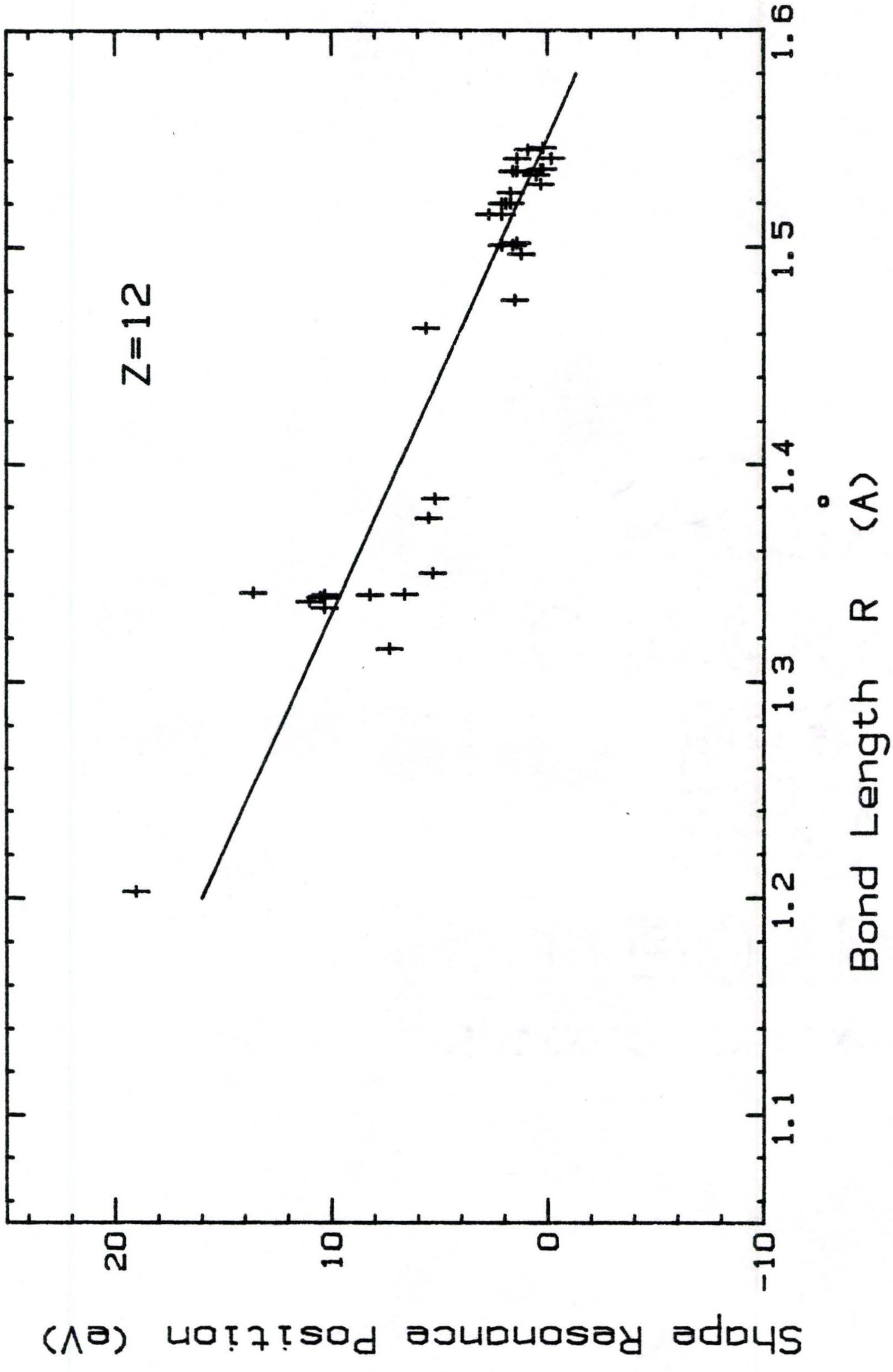
Z=12
Shape Resonance Position (eV)
20
10
0
-10
Bond Length R (Å)
1.1
1.2
1.3
1.4
1.5
1.6

Table 7.1

Shape Resonance Position and Bond Lengths for Z=12

Molecule	Bond Type	I.P.(eV)	Ref.	Eσ(eV)	Ref.	R(Å)	Ref.	δpred.[a] (± 0.5 eV)	δact.[a] (± 0.5 eV)	
C_2H_2	C≡C	291.1	BEJ83	310.0	HB77	1.203	LB76	19.1	19.0	
$^*CH_2CF_2$	C=C	291.3	BEJ83	299.5	SSH84	1.315	LB76	13.0	8.2	}7.3
$CH_2{}^*CF_2$	C=C	296.1	BEJ83	302.5	SSH84	1.315	LB76	10.7	6.4	
cis-2-C_4H_8	C=C	290.7	est.[b]	301.0	HBS84	1.334	LB76	12.0	10.3	
C_2H_4	C=C	290.8	BEJ83	302.0	HB77	1.337	LB76	11.8	11.0	
trans-2-C_4H_8	C=C	290.7	est.[b]	301.0	HBS84	1.339	LB76	11.7	10.3	
1-C_4H_8	C=C	290.7	est.[b]	301.0	HBS84	1.34	LB76	11.7	10.3	
C_6H_{10}	C=C	290.3	est.[b]	298.5	NHS85	1.34	LB76	11.7	8.2	
C_8H_8	C=C	290.3	est.[b]	295.6	NHS85	1.3403	LB76	11.7	6.6	
C_4H_6	C=C	290.4	est.[b]	304.0	HBS84	1.341	LB76	11.6	13.6	
C_5H_8	C=C	290.3	est.[b]	295.6	NHS85	1.35	LB76	11.1	5.3	
C_4H_4O	C=C	290.9	BEJ83	297.0	NH85	1.361	LB76	10.5	5.5[c]	
C_4H_5N	C=C	290.7	BEJ83	296.8	NH85	1.38	LB76	9.5	5.2[c]	
C_5H_5N	C=C	290.6	HSH85	294.2 300.1	HSH85	1.39	LB76	8.9	8.7[c]	
C_6H_6	C=C	290.3	BEJ83	293.5 300.2	HSH85	1.40	LB76	8.4	8.7[c]	

Table 7.1 continued

Molecule	Bond Type	I.P.(eV)	Ref.	Eσ(eV)	Ref.	R(Å)	Ref.	δpred.[a] (± 0.5 eV)	δact.[a] (± 0.5 eV)
C_4H_5N	C-C	290.4	BEJ83	291.3	NH85	1.42	LB76	7.3	5.2[c]
C_4H_4O	C-C	290.7	BEJ83	291.5	NH85	1.431	LB76	6.7	5.5[c]
C_4H_6	C-C	290.4	est.[b]	296.0	HBS84	1.463	LB76	5.0	5.6
C_8H_8	C-C	290.3	est.[b]	291.8	NHS84	1.475	LB76	4.3	1.5
cis-2-C_4H_8	C-C	290.7	est.[b]	291.9	HBS84	1.497	LB76	3.1	1.2
$^*CH_3CHO$	C-C	291.3	BEJ83	293.4	SSH84	1.501	LB76	2.9	2.1
$CH_3{}^*CHO$	C-C	293.8	BEJ83	295.4	SSH84	1.501	LB76	2.9	1.6
1-C_4H_8	C-C	290.7	est.[b]	292.1	HBS84	1.502	LB76	2.8	1.4
$(^*CH_3)_2CO$	C-C	291.2	BEJ83	293.3	SSH84	1.515	LB76	2.1	2.1
$(CH_3)_2CO$	C-C	293.7	BEJ83	296.4	SSH84	1.515	LB76	2.1	2.7
C_6H_{10}	C-C	290.3	est.[b]	292.0	NHS85	1.520	LB76	1.9	1.7
trans-2-C_4H_8	C-C	290.7	est.[b]	292.6	HBS84	1.520	LB76	1.9	1.9
C_5H_8	C-C	290.3	est.[b]	290.6	NHS85	1.529	LB76	1.4	0.3
C_2H_6	C-C	290.7	BEJ83	291.2	HB77	1.534	LB76	1.1	0.5
C_6H_{12}	C-C	290.3	BEJ83	291.9	NHS85	1.535	LB76	1.0	1.6
1-C_4H_8	C-C	290.7	est.[b]	292.1	HBS84	1.535	LB76	1.0	1.4
C_4H_8O	C-C	291.8	est.[b]	291.0	NH85	1.536	LB76	1.0	-0.8

Table 7.1 continued

Molecule	Bond Type	I.P.(eV)	Ref.	Eσ(eV)	Ref.	R(Å)	Ref.	δpred.[a] (± 0.5 eV)	δact.[a] (± 0.5 eV)
C_4H_9N	C-C	291.0	est.[b]	290.7	NH85	1.539	est.[d]	0 8	-0.3
$C_5H_{11}N$	C-C	291.0	est.[b]	292.2	NH85	1.539	est.[d]	0.8	1.2
CF_3CF_3	C-C	299.7		300.6		1.545	LB76	0.5	0.9
C_5H_{10}	C-C	290.3	est.[b]	290.5	NH85	1.546	LB76	0.4	0.2

a. From the relationship δ=Eσ-IP[SSH84].

b. Estimated from the IPs of similar molecules.

c. Intensity Weighted Average(see Chapter 4).

d. Estimated from [S62].

Figure 7.5

Plot of shape resonance position(δ) versus the bond length(R) for Z=13.

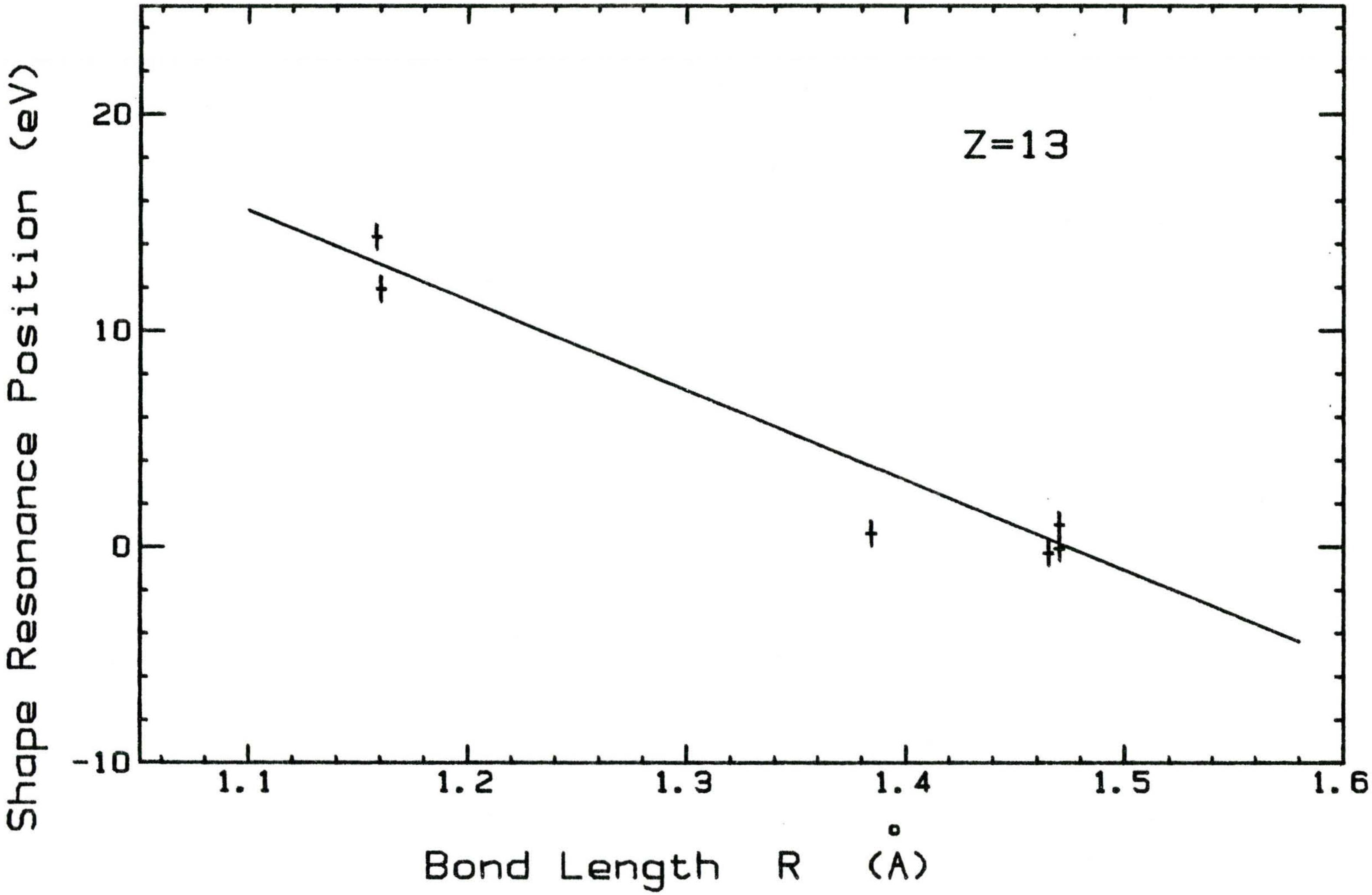
Z=13
Shape Resonance Position (eV)
20
10
0
-10
1.1
1.2
1.3
1.4
1.5
1.6
Bond Length R (Å)

Table 7.2

Shape Resonance Position and Bond Lengths for Z=13

Molecule	Bond Type	I.P. (eV)	Ref.	Eσ(eV)	Ref.	R(Å)	Ref.	δpred.[a] (± 0.5 eV)	δact.[a] (± 0.5 eV)
HCN	C-N	293.4	BEJ83	307.9	HB77	1.158	LB76	13.2	14.3
	C-N	406.8	BEJ83	420.8	HB79	1.158	LB76		
C_2N_2	C-N	294.5	HB79	306.3	HB79	1.16	LB76	13.1	11.8
	C-N	407.4	HB79	419.3	HB79				11.9
C_5H_5N	C-N	404.2	BEJ83	406.7	HSH85	1.338	LB76	5.2	6.0[b]
				413.4					
C_4H_4N	C-N	406.1	BEJ83	409.7	NH85	1.37	LB76	3.4	3.6[b]
C_4H_8N	C-N	404.6	BEJ83	404.5	NH85	1.472	est.[c]	-0.6	-0.1
$C_5H_{11}N$	C-N	404.6	BEJ83	404.6	NH85	1.472	est.[c]	-0.6	1.0

a. From the relationship δ=Eσ-IP[SSH84].

b. Intensity Weighted Average(see Chapter 4).

c. Estimated from [CRC84].

Figure 7.6

Plot of shape resonance position(δ) versus the bond length(R) for Z=14.

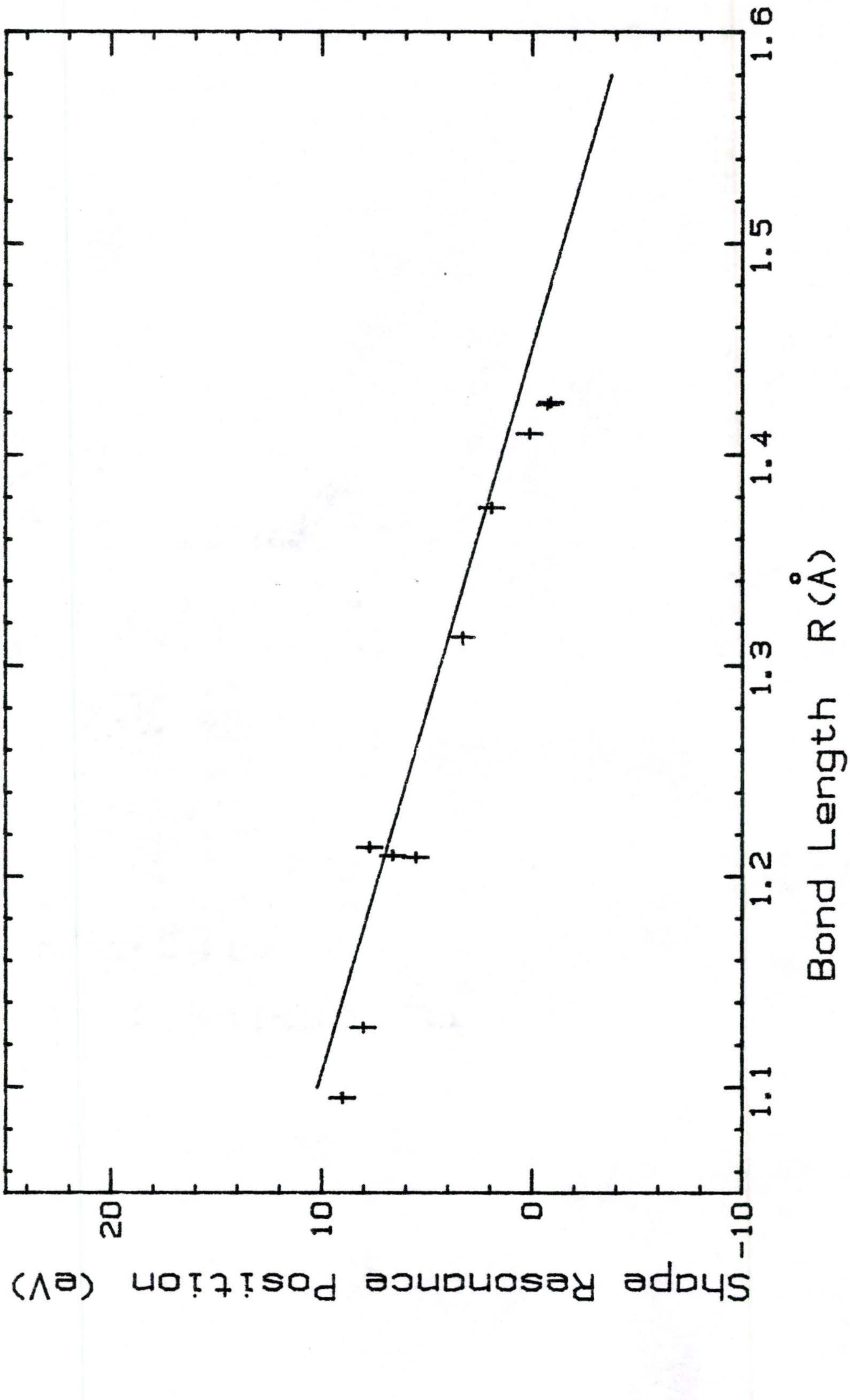
Shape Resonance Position (eV)
20
10
0
-10
Bond Length R(Å)
1.1
1.2
1.3
1.4
1.5
1.6

Table 7.3

Shape Resonance Position and Bond Lengths for Z=14

Molecule	Bond Type	I.P.(eV)	Ref.	Eσ(eV)	Ref.	R(Å)	Ref.	δpred.^{a} (± 0.5 eV)	δact.^{a} (± 0.5 eV)	
N_2	N-N	409.9	BEJ83	418.9	HB80	1.095	LB76	10.3	9.0	
CO	C-O	296.2	BEJ83	303.9	HB80	1.128	LB76	9.4	7.7	}8.0
	C-C	542.6	BEJ83	550.9	HB80				8.3	
H_2CO	C-O	294.5	BEJ83	300.9	SSH84	1.209	LB76	7.0	6.4	}5.5
	C-O	539.4	BEJ83	544.0	SSH84				4.6	
CH_3CHO	C-O	294.0	BEJ83	301.0	KVV77	1.21	LB76	7.0	7.0	}6.6
	C-O	538.4	BEJ83	544.5	KVV77				6.1	
$(CH_3)_2CO$	C-O	293.7	BEJ83	301.7	KVV77	1.214	LB76	6.9	8.0	}7.7
	C-O	537.9	BEJ83	545.3	KVV77				7.4	
BF_3	B-F	202.8	BEJ83	205.1	SSH84	1.313	LB76	4.0	2.3	}3.3
	B-F	694.8	BEJ83	699.0	SSH84				4.2	
C_4H_4O	C-O	540.0	BEJ83	541.9	NH85	1.362	LB76	2.6	1.9^b	
CH_3OCH_3	C-O	292.3	BEJ83	292.6	SSH84	1.41	LB76	1.2	0.3	}0.1
	C-O	538.6	BEJ83	538.6	SSH84				0.0	
CH_3OH	C-O	292.3	BEJ83	292.0	SSH84	1.425	LB76	0.7	-0.3	}-0.9
	C-O	538.9	BEJ83	537.4	SSH84				-1.5	
C_4H_8O	C-O	538.6	est.^{c}	537.4	NH85	1.428	LB76	0.6	-1.2	

Table 7.3 continued

a. From the relationship $\delta = E\sigma - IP$[SSH84].

b. Intensity Weighted Average(see Chapter 4).

c. Estimated from the IPs of similar molecules.

plot(Figure 7.5) there are still too few points to make accurate estimations of any trends. In the Z=14 plot(Figure 7.6) the data appears to be scattered around the line. The new data of this thesis lowers the correlation coefficient but the trend to a straight line seems to remain. Only in the Z=12 line is there some hint that the line may not be linear but more C≡C bonds need to be analyzed before this can be make clear.

As noted by Sette[SSH84], the best correlation occurrs when there is a well defined localized bond between the excited atom and its nearest neighbour. However, if the σ^* levels are subject to delocalization, as in an aromatic molecule, an intensity weighted average appears to be the most accurate way to describe the relation between spectral features and bond lengths. With this approach, there is good agreement between experiment and theory. The data for the Z=12, Z=13 and Z=14 plots are presented in Tables 7.2, 7.3 and 7.4.

7.6 Conclusions

The analysis of the continuum resonances of several cyclic species has been performed. The occurence of splitting of the σ_{C-C} resonances in the saturated cyclic hydrocarbons and the existence of a second σ_{CC} shape resonance is indicated from this analysis. This interpretation is supported by theoretical MS-Xα calculations done on cyclobutane[HD71,H85]. The intensity of the second resonance is affected by geometry and by the nature of the heteroatom. The geometric effect is one of decreasing intensity and increasing width as the ring size is increased. The effect of the heteroatom is as yet unclear due to insufficient data.

The updated results of the linear shape resonance position bond length empirical relationship have been presented. This simple relationship appears to hold remarkably well for most of the molecules analyzed. Most of the discrepancies occurred in molecules where there was the possibility of delocalization of the σ^* levels.

CHAPTER 8

CONCLUDING REMARKS

The inner shell energy loss spectra of some cyclic species have been recorded and their spectral features discussed. In all cases except for benzene, the spectra have not been recorded previously by either ISEELS or photoabsorption. In some cases the unpublished condensed phase NEXAFS spectra were available to aid in the spectral assignments. The combination of gas phase, solid and monolayer spectra has been shown to be particularly useful in unambiguously identifying Rydberg, π^* and σ^* orbitals. This approach has been used to reassign the spectral features of benzene(Chapter 4). The apparent domination of unoccupied valence states in a majority of the spectra analyzed may be an indication that sharp intense features, which were attributed to transitions to Rydberg states in previous ISEELS work, may indeed be transitions to molecular states of antibonding character. The ring systems of saturated hydrocarbons showed a second σ^*state which is believed to be a result of in-ring overlap of atomic orbitals. This is supported by the decrease in the intensity of this feature as the ring size increases. The replacement of a carbon atom with an oxygen or nitrogen did not greatly alter the appearance of the spectra from that of the parent hydrocarbon. The heteroatom did, however, affect the position and intensity of certain features. The ISEELS spectrum of the heteroatom showed, in most cases, transitions similar to those observed in the carbon K shell spectrum. This indicates that the antibonding levels are appreciably delocalized over the entire molecule.

The σ shape resonance position relative to the ionization potential, has been shown to be related to bond length in simple molecules[SSH84]. The results of my work seems to indicate that cyclic molecules follow the same relationship. However, care must be taken in certain cases. In cyclic molecules there appears to be more delocalization of the σ^* states. In saturated molecules, this produced a weak second σ shape resonance but did not significantly affect the comparison between the predicted and actual resonance position. Aromatics and other molecules with substantial delocalization are more difficult to deal with in simple terms. These molecules do not follow the picture of one bond, one resonance as well and care must be taken in treating the bond length/resonance correlations in these molecules.

The future for a developing technique such as ISEELS is excellent. There is a large amount of data yet to be recorded and analyzed. As this is done, the processes involved in inner shell excitation will become better understood. In the near future, analysis of some long chain hydrocarbons will clarify the assignment of the second continuum feature in cyclic hydrocarbons. Studies of more heterocyclic molecules such as six membered oxygen containing rings and unsaturated nitrogen containing rings will further document the effect which the heteroatom has on the electronic levels of the ring. In all cases the empirical relationship between bond length and shape resonance position should be tested and expanded. This relationship has held up surprisingly well through a variety of molecules. It is now hoped that theoreticians will begin to try to explain this simple relationship in more basic terms.

REFERENCES

A71 E.E. Anderson, "Modern Physics and Quantum Mechanics," Saunders Toronto(1971).

A62 F.A.L. Anet, J. Am. Chem. Soc. 84(1962), 671.

AFL79 L. Asbrink, C. Fridh, E. Lindholm, J. Electr. Spec. Relat. Phenom., 16(1979), 65.

B30 H.A. Bethe, Ann. Physik., 5(1930), 325.

BB81 C.R. Brundle and A.D. Baker "Electron Spectroscopy: Theory, Techniques and Applications," V1-4 Academic Press, London(1981).

BCJ80 A.A. Bakke, H.W. Chen and W.J. Jolly, J. Elect. Spec. Relat. Phemon., 20(1980), 333.

BDG83 A. Bianconi, M. Dell'Ariccia, A. Gargono and C.R. Natoli in "EXAFS and Near Edge Structures," Springer-Verlag, Berlin(1983) p. 57.

BEJ83 K.D. Bomben, C.J. Eyermann and W.J. Jolly, Private Communication (1983) update of BCJ80.

BR79 J.C. Bertolini and J. Rousseau, Surf. Sci., 89(1979), 467.

BST81 W.Butscher, W.H.E. Schwarz and K.H. Thumemann in "Inner Shell and X-Ray Physics of Atoms and Solids," ed. D.J. Fabian, Kleinpoppen and L. Watson, Plenum Press, New York(1981).

C58 E.G. Cox, Rev. Mod. Phys., 30(1958), 159.

C67 E. Clementi, J. Chem. Phys., 46(1967), 4731.

C71 L.G. Christophorou, "Atomic and Molecular Radiation Physics," Wiley Interscience, London(1971).

CCK72 D.J. Clark, R.D. Chamber, D. Kilcast and W.K.R. Musgrave, J. Chem. Soc. Faraday II, 68(1972), 309.

CK71 D.J. Clark and D. Kilcast, J. Chem. Soc. B(1971), 2243.

CRC74 "CRC Handbook of Spectroscopy Vol. 1," ed. J.W. Robinson, CRC Press, Cleveland(1974).

CRC84 "CRC Handbook of Chemistry and Physics 64th Edition," ed. R.C. Weast, CRC Press, Florida(1984).

CS65 C.A. Coulson and A. Streitwiser Jr., "Dictionary of Pi Electron

Calculations," W.H. Freeman and Co. San Francisco(1965).

D72 J.L. Dehmer, J.Chem. Phys., 56(1972), 4496.

DD76 J.L. Dehmer and D. Dill, J. Chem. Phys. 65(1976), 5327.

DS74 D.W. Davis and D.A. Shirley, J. Electr. Spec. Relat. Phenom., 3(1974), 157.

FH14 J. Franck and G. Hertz, Verdandl. Deut. Phys. Ges., 16(1914), 457.

FK78 R.P. Frueholz and A. Kuppermann, J. Chem. Phys. 69(1978), 3614.

FMK76 W.M. Flicker, O.A. Mosher and A. Kupperman, J. Chem. Phys., 64(1976), 1315.

GDM85 A. Gedanken, J. Doering, J. Moore, J.K. Olthoff, J. Tossell, A.P. Hitchcock, P. Fisher and M.B. Robin, submitted to J. Am. Chem. Soc.(1985).

GL81 T. Gustafsson and H.J. Levinson, Chem. Phys. Lett., 78(1981), 28.

GMT85 J.C. Giordan, J.H. Moore and J.A. Tossel, J. Am. Chem. Soc., in press(1985)

H73 J.B. Hasted, Cont. Phys., 14(1973), 357.

H78 A.P. Hitchcock, PhD Thesis, University of British Columbia(1978).

H82 A.P. Hitchcock, J. Electr. Spec. Relat. Phenom., 25(1982), 245.

H85 J.A. Horsley, Private Communication(1985).

HB77 A.P. Hitchcock and C.E. Brion, J. Electr. Spec. Relat. Phenom., 10(1977), 317.

HB79 A.P. Hitchcock and C.E. Brion, Chem. Phys., 37(1979), 319.

HB80 A.P. Hitchcock and C.E. Brion, J. Electr. Spec. Relat. Phenom., 18(1980), 1.

HBS84 A.P. Hitchcock, S. Beaulieu, T. Steel, J. Stöhr and F. Sette, J. Chem. Phys., 80(1984), 3927.

HD71 R. Hoffmann and R.D. Davidson, J. Am. Chem. Soc., 93(1971), 5699.

HSH85 J.A. Horsley, J. Stöhr, A.P. Hitchcock, D.C. Newbury, A.L.

Johnson and F. Sette, J. Chem. Phys., in press(1985).

I71 M. Inokuti, Rev. Mod. Phys. 43(1971), 297.

J85 A.L. Johnson, Private Communication(1985).

JHA84 Y. Jugnet, F.J. Himpsel, P.L. Avouris and E.E. Koch, Phys. Rev. Lett., 53(1984), 198.

JMS83 A.L. Johnson, E.L. Muetterties and J. Stöhr, J. Am. Chem. Soc., 105(1983), 7183.

JMS85 A.L. Johnson, E.L.Muetterties, J. Stöhr and F. Sette, submitted to J. Chem. Phys.(1985).

JS73 L. Jorgensen and L. Salem, "The Organic Chemists Book of Orbitals," Academic Press, New York(1973).

K85 R.J. Koestner, Private Communication(1985).

KJ66 E. Keulen and F. Jellinek, J. Organomet. Chem., 5(1966), 50.

KRT77 G.C. King, F.H. Read and M. Tronc, Chem. Phys. Lett. 52(1977), 490.

KSG84 R.J. Koestner, J. Stöhr, J.L. Gland and J.A. Horsley, Chem. Phys. Lett., 105(1984), 332.

KTR77 G.C. King, M. Tronc, F.H. Read and R.C. Bradford, J. Phys. B, 10(1977), 2479.

KVV77 R.B. Kay, Ph.E. Van der Leeuw and M.J. Van der Wiel, J. Phys B, 10(1977), 2513.

L78 I.N. Levine, "Physical Chemistry," McGraw-Hill, New York(1978).

L85 E. Linholm, J. Chem. Phys., in press(1985).

LB76 "Structural Data of Free Polyatomic Molecules" ed. Landolt and Bornstein, New Series II, Vol. 7, Springer, Berlin(1976).

LID78 S. Lehwald, H. Ibach and J.E. Demuth, Surf. Sci., 78(1978), 577.

N83 C.R. Natoli in " EXAFS and Near Edge Structures," Springer-Verlag, Berlin(1983).

NF68 V.I. Nefedov and V.A. Fomichev, J. Struct. Chem., 9(1968), 217.

NH85 D.C. Newbury and A.P. Hitchcock, in press Can J. Chem.(1985).

NHS85 D.C. Newbury, A.P. Hitchcock, J. Stöhr and A.L. Johnson, to be submitted to J. Chem. Phys.(1985).

NM79 F.P. Netzer and J.A.D. Matthew, Solid State Comm., 29(1979), 209.

NS75 I. Nenner and G. J. Schulz, J. Chem. Phys., 62(1975), 1747.

P40 L.W. Pickett, J. Chem. Phys., 8(1940), 293.

PCW53 L.W. Pickett, M.E. Corning, G.H. Wieder, D.A. Semenow and J.M. Buckley, J. Am. Chem. Soc., 75(1953), 1618.

PSB76 J.J. Pireaux, S. Svensson, B. Basilier, P.A. Malnquist, U. Gelius, R. Coudano and K. Siegbahn, Phys. Rev. A., 14(1976), 2133.

R75 M.B. Robin, "Higher Excited States of Polyatomic Molecules," Vol.I,II, Academic Press, New York(1975).

RC73 B. Rees and P. Coppens, Acta Crystallogr. Sect. B., 29(1973), 2516.

RL77 T.N. Rescigno and P.W. Langhoff, Chem. Phys. Lett., 51(1977), 65.

RRG83 R.A. Rosenburg, V. Rehn, A.K. Green and P.R. LaRoe in "Desorption Induced By Electronic Transitions," ed. N.H. Tolk, M.M. Traury, J.C. Tully and T.E. Modey, Springer, Berlin(1983).

S62 B.P. Stoicheff, Tetrahedron, 17(1962), 135.

S67 J.A. Simpson in "Methods of Experimental Physics," ed. V.W. Hughes and H.L. Schultz, 4A(1967), 127.

S77 E.A. Stern, J. Vac. Sci. Tech. 14(1977), 461.

S82 T. Steel, B.Sc. Thesis, McMaster University(1982).

S83 J. Stöhr, Internal Report, EXXON Reseach Co., New Jersey(1983).

S84 R.N. Sodhi, PhD Thesis, UBC(1984).

Sa84 J. Stöhr in " Chemistry and Physics of Solid Surfaces V," ed. R. Vanselow and R. Howe, Springer, Berlin(1984), 231.

S85 J. Stöhr, Private Communication(1985).

SB84 R.N. Sodhi and C.E. Brion, J. Electr. Spec. Relat. Phenom.,34 (1984), 363.

SBJ81 J. Stöhr, K. Baberschke, R. Jaeger, R. Trechler and S. Brennan, Phys. Rev. Lett., 47(1981), 381.

SGE83 J. Stöhr, J.L. Gland, W. Eberhandt, D. Outka, R.J. Madix, F. Sette, R.J. Koestner and U. Doebler, Phys. Rev. Lett., 51 (1983), 2414.

SJ71 J.C. Slater and K.H. Johnson, Phys. Rev. B., 5(1971), 844.

SJ82 J. Stöhr and R. Jaeger, Phys. Rev. B., 26(1982), 4111.

SNJ69 K. Siegbahn, C. Nordling, G. Johansson, J. Hedman, P.F. Heden, K. Harin, U. Gelius, T. Bergmark, L.O. Werne, R. Manne and Y. Baer, "ESCA Applied to Free Molecules," North Holland, Amsterdam(1969).

SSJ84 J. Stöhr, F. Sette and A.L. Johnson, Phys. Rev. Lett. 53(1984), 1684.

SSJ85 J. Stöhr, F. Sette and A.L. Johnson, unpublished work(1985).

SSH84 F. Sette, J.Stöhr and A.P. Hitchcock, J. Chem. Phys., 81(1984), 4906.

T81 B.K. Teo, J. Am. Chem. Soc., 103(1981), 3990.

TKB76 M. Tronc, G.C. King, R.C. Gradford and F.H. Read, J. Phys. B, 9 (1976), L555.

TNN77 K. Tanaka, T. Nomura, T. Noro, H. Tatewaki, T. Takada, H. Kashiwagi, F. Sasaki and K. Ohno, J. Chem. Phys., 67(1977), 5738.

W74 G. Wight, PhD Thesis, UBC(1974).

WB74 G. Wight and C.E. Brion, J. Elect. Spec. Relat. Phenom., 4(1974), 25.

WBV74 G. Wight, C.E. Brion and M.J. Van der Wiel, J. Electr. Spec. Relat. Phenom., 1(1974), 457.

WGS74 B. Wannberg, U. Gelius and K. Siegbahn, J. Phys. E., Sci. Instr., 7(1974), 149.